FINAL REPORT

WAVE--ICE INTERACTION & SITE-SPECIFIC WAVE PREDICTION DURING LIMEX/LEWEX '87 PILOT PROJECT

Contract No. FP802-6-2704/01-SS
Our file No. 58047

Prepared For:

MARINE ENVIRONMENTAL DATA SERVICE (MEDS)
Dept. of Fisheries & Oceans
Stn. 1202 – 200 Kent Street
Ottawa, Ontario
K1A 0E6

Prepared By:

MacLaren Plansearch Limited
Purdy's Wharf Tower
1959 Upper Water Street
Suite 701
Halifax, Nova Scotia
B3J 3N2

March 1988

MacLaren Plansearch

MacLaren PLANSEARCH LIMITED
SUITE 701, PURDY'S WHARF TOWER, 1959 UPPER WATER STREET, HALIFAX
NOVA SCOTIA, CANADA B3J 3N2
TELEPHONE: (902) 421–3200. TELEX: 019–22718. CABLE: LAVALIN HFX

58047

May 31, 1988

Dr. Ron Wilson
Marine Environment Data Service
Department of Fisheries & Oceans
200 Kent Street
Ottawa, Ontario
K1A 0E6

Dear Dr. Wilson:

RE: WAVE–ICE INTERACTION & SITE–SPECIFIC WAVE PREDICTION DURING LIMEX/LEWEX '87 PLOT PROJECT (UP–M6–027) SSC CONTRACT # FP802–6–2704/01–SS

Pursuant to your review of the daft report, we are pleased to submit two copies of the final report for the above referenced study. The report presents the results of the work done under this contract. This work was carried out jointly by MacLaren Plansearch Limited, C–CORE, and Oceanweather Inc.

A magnetic tape of the data obtained during this work (i.e, meteorological data, ice motion package measurements, and wind/wave hindcast results) was provided previously. The aerial photographs original negatives were also provided.

We trust this is satisfactory, but should you have any questions or further requirements, please contact the undersigned.

On the behalf of the project team, I would like to thank you for your assistance. We look forward to working with you again in these endeavors.

Yours very truly,

MacLAREN PLANSEARCH LIMITED

Bassem M. Eid, P.Eng., Ph.D.
Project Manager

Lavalin

WAVE–ICE INTERACTION & SITE SPECIFIC WAVE PREDICTION DURING LIMEX/LEWEX '87 PILOT PROJECT

TABLE OF CONTENTS

ACKNOWLEDGEMENT

This study was carried out jointly by MacLaren Plansearch Limited, Halifax, N. S., Centre for Cold Ocean Resources Engineering (C–CORE) of the Memorial University of Newfoundland. St. John's, Newfoundland, and Oceanweather Inc., Cos Cob, Connecticut. The Principal Investigators for this study were Dr. B. Eid, and Mrs. Co Morton from MacLaren Plansearch, Mr. W. Windsor, Mr. Do Mitchell and Dr. J. Lever of C–CORE, and Drys. V. Cartoned and A. Greenwood of Oceanweather Inc.

The study was a result of an unsolicited proposal (UP) funded by Supply and Services Canada (DSS UP funds) and contributions from DFO, Marine Environmental Data Service (MEDS) and Bedford Institute of Oceanography (BIO), EMR (RADARSAT office, CCRS), and the Federal Panel on Energy R & D (PERD). The contribution from these sources is acknowledged with gratitude.

We are grateful to several LIMEX/LEWEX participants who made this study a successful and most interesting one. Our special thanks to the Scientific Authority Dr. Ron Wilson of MEDS for his contribution and encouragements throughout the course of the study, We also would like to acknowledge with gratitude the initiation and encouragements of Drs. Clive Mason of BIO and Nelson Freeman of DFO, without their support this study would have not been possible. Special thanks to Dr. Charles Tang of BIO, the Baffin Chief Scientist, and Sue Argus and Keith Rainey of CCRS for their suggestions and stimulating discussions, Dr. Nethercote of DND. So Bales and L. Thomas of DTNSRD for providing met/ocean data. We also acknowledge Husky Bow Valley for providing meteorological and wave data at their drilling location on the Grand Banks.

1.0 INTRODUCTION

The Labrador Extreme Waves Experiment (LEWEX) and The Labrador Ice Margin Experiment (LIMEX) Pilot Project was an international effort to understand wind–generated ocean waves and ocean–ice interaction off the east coast of Labrador and Newfoundland. The LEWEX/LIMEX field experiment took place from March 9 to 26, 1987. The LIMEX was divided into two distinct activities: (1) remote sensing and (2) ice and oceanography. The remote sensing component involved several aircraft employing a number of different sensors to collect information about ice and sea conditions at the marginal ice zone (MIZ). The ice/ocean component was conducted as part of the oceanographic cruise of the Physical and Chemical Sciences Branch of the Department of Fisheries and Ocean, Bedford Institute of Oceanography (BIO). Both the ocean program and the investigation of ice conditions at the ice edge were carried out during the LIMEX cruise. The ice program was conducted by a team of researchers from a number of agencies and institutions. RADARSAT Ice applications Group, Jet Propulsion Laboratory (JPL), Naval Ocean Research Development Activity (NORDA) and Scott Polar Research Institute (SPRI) were involved chiefly in a ground–truthing program for the remote sensing overflights. C–CORE, Physical and Chemical Sciences Branch, MacLaren Plansearch Ltd, and the Alfred–Wegener–Institut Fur Polar–Und Meeresforschung were interested in the measurement and the study of the physical processes of the ice/ocean interaction at the ice edge. The ice studies involved the measurement of wave propagation into the ice cover, the drift and circulation of the pack ice, the strength and morphology of the ice cover in its final phase of disintegration and melting. The ice/wave interaction investigation was planned to be integrated with the wave data collection of a second separate programme; the Labrador Extreme Wave Experiment (LEWEX). It was unfortunately, most of the ice motion measurements were made after the LEWEX programme was completed.

This report describes our contribution to the LIMEX/LEWEX Project.

1.1 STUDY OBJECTIVES AND SCOPE

The major general objectives of the LEWEX/LIMEX were:

a) to test and assess the capability of various remote sensing techniques, i.e. the Canadian C–band synthetic aperture radar (SAR), the U.S. Ku–band radar ocean wave spectrometer (ROWS), and surface contour radar (SCR), for estimating directional wave properties, and to assess the in situ techniques for monitoring ocean waves outside and inside the marginal ice zone (MIZ);

b) to assess a number of spectral ocean wave models including the first, second and third generation (1G, 2G and 3G) models;

c) to conduct ice properties tests and study ice–ocean interaction, to examine penetration of waves into the MIZ and identification of ice properties from remote sensing data.

The main objective of the work presented in this report is to study the wave ice interaction and to provide a site specific wind/wave forecasting and hindcasting during the duration of LEWEX/LIMEX. The following tasks are included in this study:

1) literature review of relevant publications, e.g. waves in ice, wave–ice interaction, ice–structure interaction, etc.

2) participation in the LIMEX field experiment. Baffin Cruise, this included provision of meteorological data collection onboard the Baffin, wave–ice induced motion using C–Core ice motion package, aerial photography, and measuring ice surface characteristics;

3) provision of wave forecasting during the experiment, and wind/wave hindcasts using ODGP (Ocean Data Gathering Program) spectral ocean wave model. The hindcast wind fields will be used by other investigators to run their wave models (e.g. GSOWM, 3GWAM, BIO, NOAA, BMO). The models and sensor data intercomparisons will be carried out by Dr. Robert Beal of Applied Physics Laboratory (APL), John’s Hopkins University;

4) study of ice–wave interaction, particularly wave penetration into the MIZ, floe size distribution and ice mechanics,

1.2 STUDY ORGANIZATION

The study was carried out jointly by MacLaren Plansearch Limited (MPL), the Contractor, and C–CORE and Oceanweather Inc, (OWI) as subcontractors.

MacLaren Plansearch provided the overall project management, literature review, collection and compilation of all meteorological data and relevant wave records, provision of weather and seastate

forecasting during the duration of the field experiment, spectral analysis (1–D and 2–D spectra) of the ice motion package data, preliminary study of wave–ice interaction, and report preparation.

C–CORE provided wave–induced ice motion measurements (using their ice motion package) and data analysis, aerial photography, ice surface characteristics, floe size distribution, and discussions on ice properties and ice mechanics.

Oceanweather Inc. provided the site specific wave forecasting using their ODGP spectral wave model, wind fields and wave fields hindcasts for the entire LEWEX and LIMEX duration.

1.3 STUDY HIGHLIGHTS

The LIMEX ’87 pilot project has demonstrated that wave–ice interaction is one of the most significant environmental processes acting within the ice cover. It also demonstrated that the ice cover of the southern extent of the Labrador ice field is an extremely dynamic environment. The ice motion measurements showed that wave–ice interaction appears to be a major factor governing the make–up of the ice cover and accelerating the breakup and melting of the ice. The incident ocean waves dissipate most of their energy into the ice cover at the ice edge. This energy transfer is exhibited in mechanical action between the ice floes and grinding of ice debris which lies between the floes (i.e. brash ice). It is this continuous action which apparently explains the broken nature and small floe size characteristics of pack ice along the coast of Labrador and Newfoundland.

The ice motion measurements collected in this study showed that the ocean waves (swell) penetration into ice cover is governed by the size of the incident waves and characteristics of ice cover (i.e. ice thickness, floe size, distribution, ice concentration, and strength). It was found that long period waves and swell can penetrate a significant distance into the ice pack. Further intensive research work still required in order to understand waves in ice fully.

2.0 LITERATURE REVIEW

A literature search for published material relevant to the present LIMEX/LEWEX study (March, 1987) has identified several papers which discuss the interaction of winds, waves and ice in the marginal ice zone. A review of the literature encompasses papers describing the propagation of waves in an ice field, the modelling of waves and ice in the marginal ice zone, the climatology of ice fields and the interaction of ice and structures. A description of the research papers found in the literature search is provided in Appendix A.

The literature review has been broken up into the following categories:

1. Waves in ice;
2. Air–ice interaction in the marginal ice zone;
3. Ice–ocean interaction in the marginal ice zone;
4. Ice–air–ocean interaction in the marginal ice zone;
5. Ice climatology;
6. Ice–structure interaction; and
7. Background and related material.

A short description of each paper is provided to aid the reader in determining its contents and consists of its abstract and the source of publication. In some papers, an abstract was unavailable so a short summary is provided instead.

2.1 WAVE–ICE INTERACTION STUDY

Two main processes must be considered when studying the interaction between ice and waves. These processes are:

a) wave fields propagating into the marginal ice zone (MIZ) determined by
   - wave attenuation in the MIZ,
   - wave reflection at the ice edge,
   - dispersion of wave energy in the MIZ,
   - dissipation of wave energy, and
   - re–distribution of wave energy in the MIZ, and

b) the generation of the wave fields through the marginal ice zone, and the effect of the MIZ on open water waves; i.e. wave generation in fetch–limited cases in offshore wind situations.

Ice characteristics affecting these processes are the concentration and size of the ice floes in the MIZ. Since the MIZ is composed of varying the ice concentrations and ice floe sizes, the edge of the marginal ice zone must be identified when modelling wave propagation. A common method of determining the ice edge has been to select an ice concentration to determine the ice boundary (e.g. 3/10th, 5/10th, etc.).

2.2 WAVE PROPAGATION INTO THE MIZ

The propagation of wave fields into the MIZ has been the subject of a limited number of studies. In one of the earliest studies. Robin (1963) observed that long period waves and swell can be detected by shipborne wave recorders several kilometers into the ice. In a later study, Wadhams (1975) used a laser profiler and a infrared line scanner to simultaneously image surface waves and ice floe sizes and concentrations over an open drift ice field off the east coast of Newfoundland. More recently, Wadhams (1978) made a series of wave recordings under the ice margin between Greenland and Spitsbergen using an inverted echo sounder mounted on a patrol submarine. As a result of these experiments, the wave energy was found to have an exponential decay with penetration distance, with the rate of decay dependent on the wave frequency, i.e. ($E(x,f) = E(O,f) \exp (A(f) x)$). Squire and Moore (1980) studied the wave decay in pack ice in the Bering Sea by placing vertical accelerometers on ice floes near the ice edge, and measuring the open water waves at the ice edge. An exponential decay of the wave energy was observed with the decay rate in general agreement with those found in Wadhams (1975). These studies describe only a one dimensional wave energy decay along the axis of propagation without taking into consideration wave dispersion.

Very recently, Wadhams et al. (1986) studied the effect of the marginal ice zone on ocean directional wave spectrum during the MIZEX–84 experiment in the Greenland Sea. The aim was to study the processes of reflection and refraction of the directional spectra. One of the major limitations found during this experiment was the limited data regarding prevailing ice conditions (i.e. floe size distribution and thickness).

Recently, Cardone (1980) used a one–dimensional numerical model to investigate the decay characteristics of typical Bering sea storm seas in the MIZ. The model included all processes modelled in the two–dimensional deep water model, including propagation and generation, with the addition of the above attenuation law of Wadhams (1975) and Squire and Moore (1980), and reductions in the magnitude of the linear and exponential growth rates consistent with reductions in momentum transfer across an interface partially covered with ice. Simulations were carried out with different fractional ice covers.

2.3 WAVE GENERATION IN THE MIZ

Wave generation in the marginal ice zone is not fully understood. Off ice winds often have a limited fetch in the MIZ, and produce short period waves, Wadhams (1983) associates the offshore winds with the formation of ice bands, and proposes the mechanisms involved in open spans of water in the MIZ. These waves are reflected by the ice floes, producing a force large enough to push them seaward. This mechanism

enlarges the open span of water, which enhances the forces on the ice floes and produces ice bands.

Masson and LeBlond (1987) also investigated the effects of offshore winds on wave generation in the marginal ice zone. The study proposes a theoretical description of the formation of waves within the ice zone, and how the waves are scattered by the ice floes.

The above two studies describe some of the mechanisms involved in ice motion as a result of offshore winds. However, wave generation in the MIZ is not fully understood, and requires more research work.

2.4 APPLICATIONS

The extreme ice loads of the marginal ice zone are postulated to be associated with ice impact, or what is sometime called ice slamming, by ice floes driven by winds, ocean currents and ocean waves. The ice cover on the open ocean is highly broken hence it represents a very inhomogeneous material and consequently estimates of ice loads for ice/structure interaction are not well established. Application of some of the numerical techniques available for engineering analysis make it feasible to calculated probable distributions for ice loads which would result from various driving force histories and various fracture and ice clearing scenarios.

Before ice forces and ice movements can be effectively used, more work must be done to fully understand the processes involved in the marginal ice zone. From several studies, wave attenuation can be approximated in a one dimensional problem when wave measurements are taken. A theoretical approximation of the wave attenuation has been proposed, but required knowledge of the floe size, ice concentration and wave reflection.

Dispersion and re–distribution of wave energy in the MIZ needs further study, Wadhams et al. (1986) measured wave energy dispersion by measuring the directional wave energy inside and outside the MIZ. The results indicated an isotropic dispersion of the wave energy as it propagated into the MIZ. Theoretical formulations of this process have been proposed which required more study.

Modelling waves in the MIZ required knowledge of both wave characteristics and the ice conditions (e.g. thickness, ice floe size, ice concentration, strength, etc.). Further research work are needed to fully understand the relation between ice conditions and wave processes in the MIZ, which is one of the major objectives of this study.

3.0 FIELD EXPERIMENT AND DATA COLLECTION

3.1 METEOROLOGICAL DATA

During the LIMEX/LEWEX project, three ships were deployed in the region of interest to collect meteorological and sea state data. The CSS BAFFIN collected measurements in the marginal ice zone, while the HMNS TYDEMAN and the CFAV QUEST collected measurements offshore outside the ice edge (Figure 3.1a). One of the objectives of this study was to collect all meteorological data available during the field experiment (March 9–26, 1987). These data were further used to provide wind fields hindcast for the entire study period suitable for running a number of numerical models (see section 4.0).

Changes in the ice conditions during the field experiment were very drastic. At the start of the experiment, winds were predominantly from the west which caused the ice field to extend over to a distance between 50nm and 100 nm from the coast as shown in Figure 3.1b . On March 13, the wind shifted to northeasterly, and became easterly on March 16, pushing the ice back against the shore. Over the course of the next week, during the principal LIMEX data collection period, the easterlies to Northeasterlies continued and the ice was compacted against the shore in a narrow (approximately 10 nm) band of 10/10th ice. The properties of the ice and floe size distribution during this period are described in Section 5.0 of this report.

3.1.1 SUMMARY OF DATA COLLECTED

An automatic weather station (AWS) was installed onboard the BAFFIN. Measurements taken by the AWS include measurements of the wind (speed and direction), atmospheric pressure, air temperature, and solar radiation. In addition, marine observations were manually recorded in a MANMAR log, and a log report of the cruise was kept.

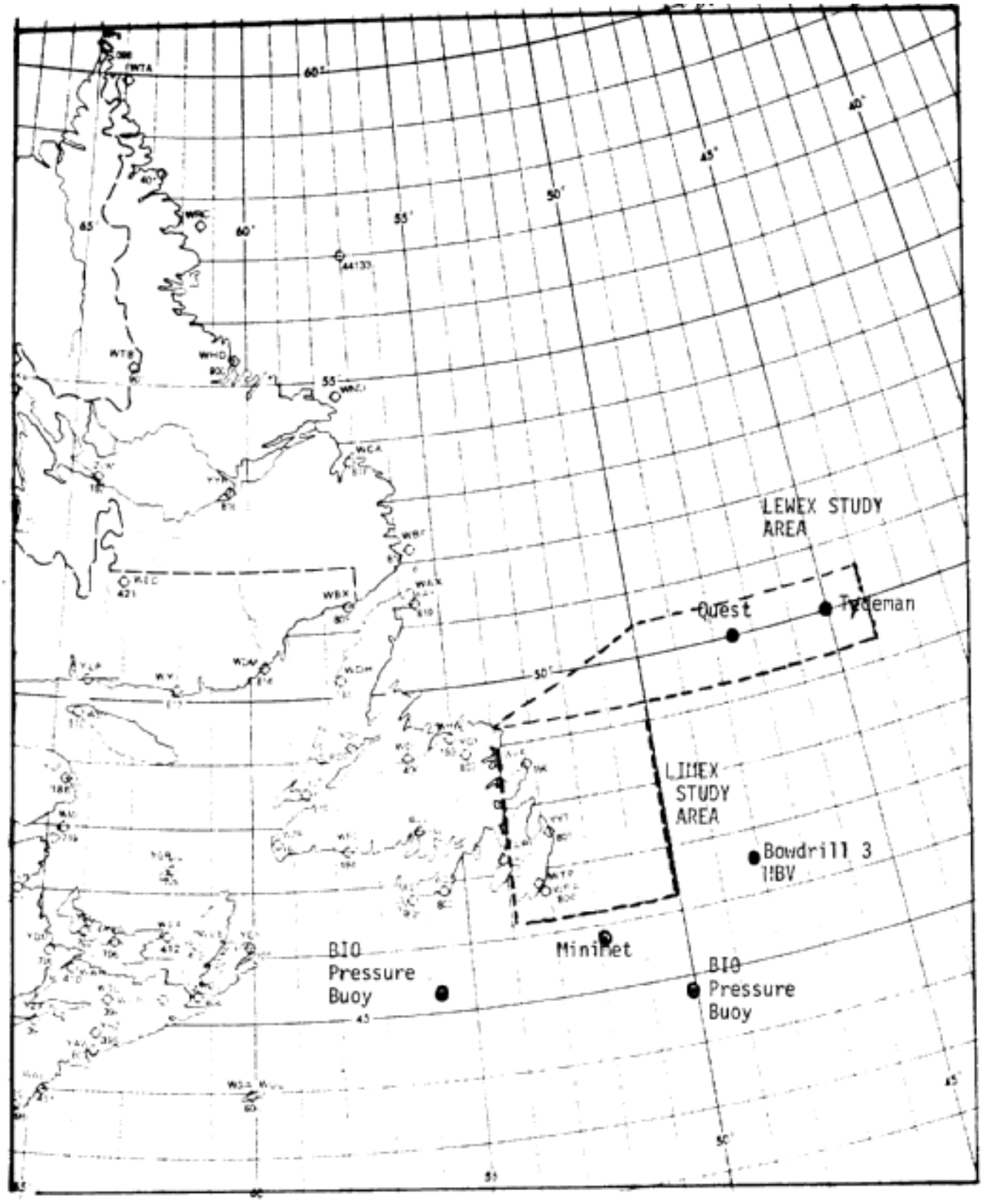

Figure 3.1a Locations Map

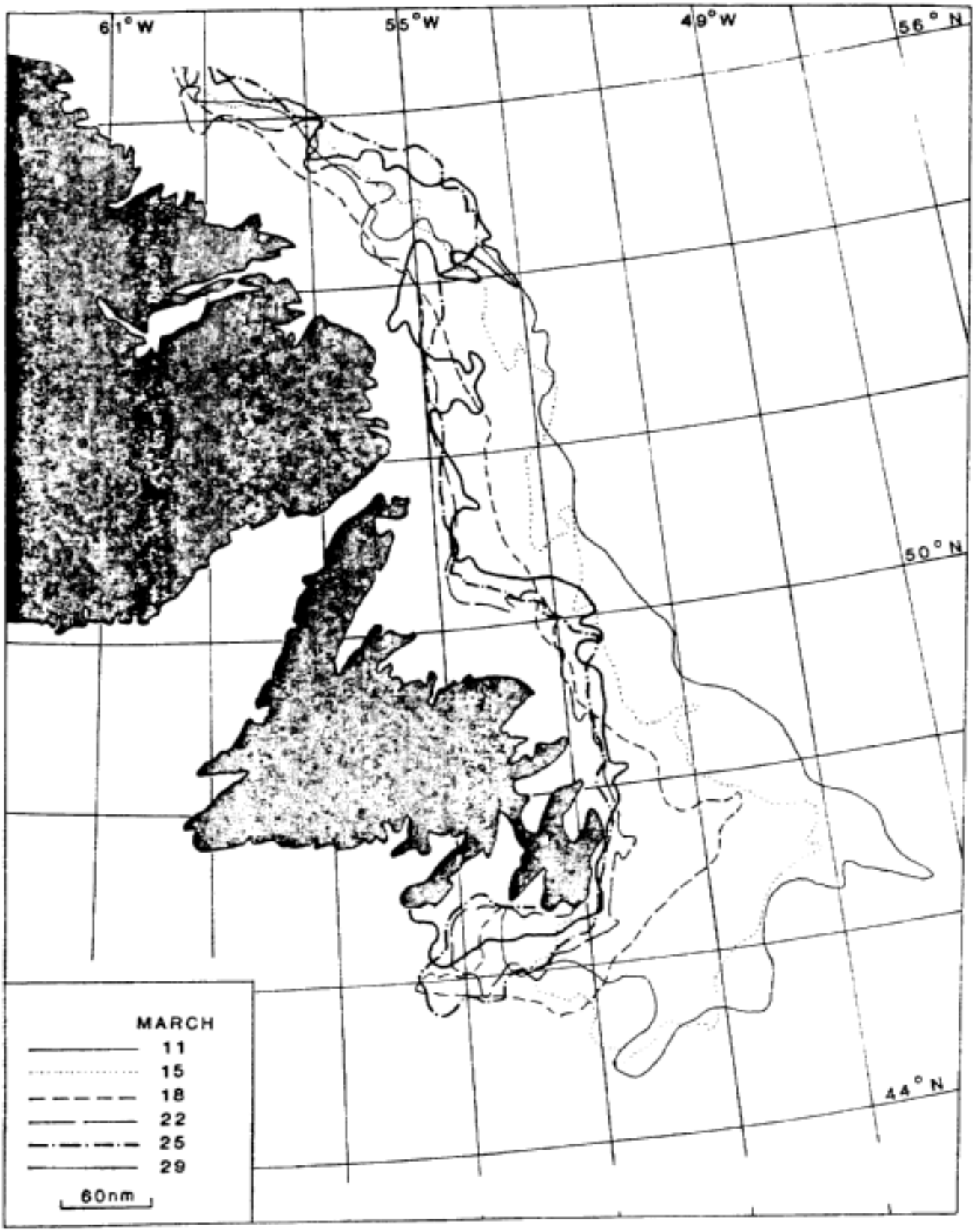

FIGURE 3.1b LIMEX/LEWEX Study Area showing ice edge from AES data (source Sue Argus,CCRS)

In addition to the data collected by AWS, meteorological data was collected on the QUEST, the TYDEMAN, and on a nearby oil rig. BOW DRILL 3, operated by Husky/Bow Valley.

During the project, synoptic weather charts for the Canadian East Coast were generated, and the ODGP (Ocean Data Gathering Program) spectral wave model was utilized in providing wave forecasts for the region.

After the project, meteorological data were obtained from the following ground stations in Newfoundland – Gander. St. John's, St. Anthony, Mary's Harbour, Bonna Vista, Cape Race and Cartwright. Synoptic weather charts obtained from MacLaren Plansearch Limited and AES Gander office were also obtained.

A record of a the LORAN–C position track of the BAFFIN, and the data collected by a MINIMET buoy deployed from the BAFFIN, were also obtained. Data records from two BIO's pressure buoys deployed in the region were also received.

A summary of the data collected is shown in Table 3.1 . Time series plots of some of the data are shown in Appendix B.

3.2 WAVE–INDUCED ICE MOTION MEASUREMENTS

There were 13 deployments and recoveries of the C–CORE Wave Induced Ice Motion Package during the LIMEX Project. All the deployments with the ice motion package were made with the articulated hydraulic crane on the foredeck of the CSS BAFFIN. The number system for the records with dates, times, positions and durations are provided in Table 3.2 . Positions of the ice package deployments are shown in Figure 3.2 .

Deployments 19–1B and 20–1B did not yield any recorded data due to a malfunction of instrument package B, 19–1B was on a small ice floe in a narrow strip of sea ice seaward from the main pack. 20–1B was on heavy ice under pressure while the ship was beset. In the latter case ice heave was not perceptible to a causal observer on the ice. Both these conditions were resampled in subsequent deployment.

TABLE 3.1
METEOROLOGICAL INFORMATION FROM LIMEX/LEWEX

Source	Information Available	Comments
MacLaren Plansearch (MPL)	AWS (Automatic Weather Station) on the CSS Baffin Raw Wind Speed + Direction Corrected Wind Speed + Direction Barometric Pressure Air temperature Solar Radiation	- Collected Mar 13 - 29/1987 - Winds, Pressure and temperature recorded is an average of the last ten minutes of every hour. - Solar radiation recorded every minute. - See attachment in Appendix B of of the corrected wind data. - Collected data has few gaps. - Note that the radiometer sustained some damage during the experiment.
	MANMAR Log From CSS BAFFIN Wind Speed & Direction (True) Air & Sea Temperatures Dew Point Barometric Pressure Wave height & Period	- Recorded from Mar 15 - 28/87 - Observations recorded every hour - Many gaps in the observations. - Wave information has only a few entries
	Synoptic Weather Charts Surface pressure maps & observations	- Maps drawn up twice/day (at 1200 & 1800Z) throughout experiment.
	ODGP Wave Forecasts Spectral wave products	- Available every 12 hours between Mar 9 - 21/87
Husky/Bow Valley	MANMAR Log from Bow Drill 3 Wind Speed & Direction (True) Air & Sea Temperature Dew Point Barometric Pressure Wave height & Period Some ice information	- Location 46°30'N, 48°6'W - Observations recorded every 3 hours. - few gaps in observations - MPL has received a copy of the Log from Mar 16-31/87
DREA (Defence Research Establishment Atlantic) Dr. Nethercote	Meteorological Observations From CFAV QUEST Ship Location Ship Speed & Direction Wind Speed & Direction (True) Barometric Pressure	- observations recorded from Mar 13-26/87 - recorded every four hours - many gaps in ship's motion, with few gaps in wind observations & barometris pressure - MPL has received a draft report

TABLE 3.1 (Cont'd)
METEOROLOGICAL INFORMATION FROM LIMEX/LEWEX

Source	Information Available	Comments
OWI (Oceanweather Inc.)	Synoptic Weather Maps 6-hourly surface pressure charts for N. Atlantic	
DTNR&D (Susan Bales)	Observations from TYDEMAN	- OWI has received it.
AES (Atmospheric Environment Service, Atlantic Region)	Synoptic Weather Charts from Gander Office Observations at Weatherstations in Gander (YQX) St. John's (YYT) St. Anthony (YAY) Mary's Harbour (WMH) Bonnavista (WVA) Cape Race (WRA) Cartwright (WCA)	- available for LIMEX/LEWEX period - MPL has received information.
B.I.O. (Bedford Institute of Oceanography)	Pressure Bouys Barometric Pressure Sea Temperatures MINIMET Buoy Wind speed & Direction Air & Sea temperature LORAN FILE - contains position of the BAFFIN every minute using LORAN	- 2 pressure bouys deployed at 44°40.14'N, 50°4.80'W and at 45°8.25'N, 55°47.70'W - available for LIMEX/LEWEX period - deployed at 45°46.44'N, 51°53.05'W. - Mar 18-27/87 - Buoy data is available on tape at B.I.O. - MPL has this date and has used it to correct the wind speed & direction on the BAFFIN - recorded from Mar 16-26/87

Table 3.2: Wave Induced Ice Motion Measurements

Test No.	Date time (NST)	Lat dec °	Long dec °	Duration (hours)	Ice thickness (metres)	Photo Ref number	Field Remarks	Data Recovery (min)
19-1B	19/03/87 1340h 1421h	 46.0745 46.0860	 51.9401 51.9465	 0.68			No data Deployed Recovered	-
20-1B	20/03/87 1001h 1039h	 47.4317 47.4270	 52.2858 52.2913	 0.63	2.10		No data Deployed Recovered	-
21-1B	21/03/87 1048h 1202h			 1.23	1.55		 Deployed Recovered	-
21-2C	21/03/87 1242h 1300h 1345h 1408h			 0.75	1.55		 Started Deployed Recovered Stored	-
22-1C	22/03/87 1004h 1331h 1120h	 47.3410 47.3298 47.3226	 52.2566 52.2660 52.2632	 0.82 1.27	1	PRX11/6	 Deployed Ship longside Recovered	40
23-1C	23/03/87 1002h 1302h	 47.784	 52.469	 3.00			 Deployed Recovered	-
25-1C	25/03/87 1152h 1748h	 46.4303 46.3907	 52.9534 53.0898	 5.93		PRX25/1,3 PRX25/6,9	 Deployed Recovered	327
25-2B	25/03/87 1331h 1442h	 46.4291 46.4182	 53.0180 53.0437	 1.18		PRX21/3,12	 Deployed Recovered	29
25-3B	25/03/87 1527h 1611h	 46.4224 46.4184	 53.0692 53.0832	 0.73	1.47	PRX22/11,16 PRX22/17,18	 Deployed Recovered	30
25-4B	25/03/87 1631h 1713h	 46.4309 46.4277	 53.1020 53.1121	 0.70	1.16	PRX24B/12,14	 Deployed Recovered	25
26-1B	26/03/87 0849h 0945h	 46.968	 52.683	 0.93			 Deployed Recovered	16
26-2C	26/03/87 0924h 1246h 1100h	 46.973	 52.793	 0.63		PRX27/8	 Started Deployed Recovered	-
26-3B	26/03/87 1246h 1408h	 46.973	 52.793	 1.37		PRX28/8	 Deployed Recovered	30

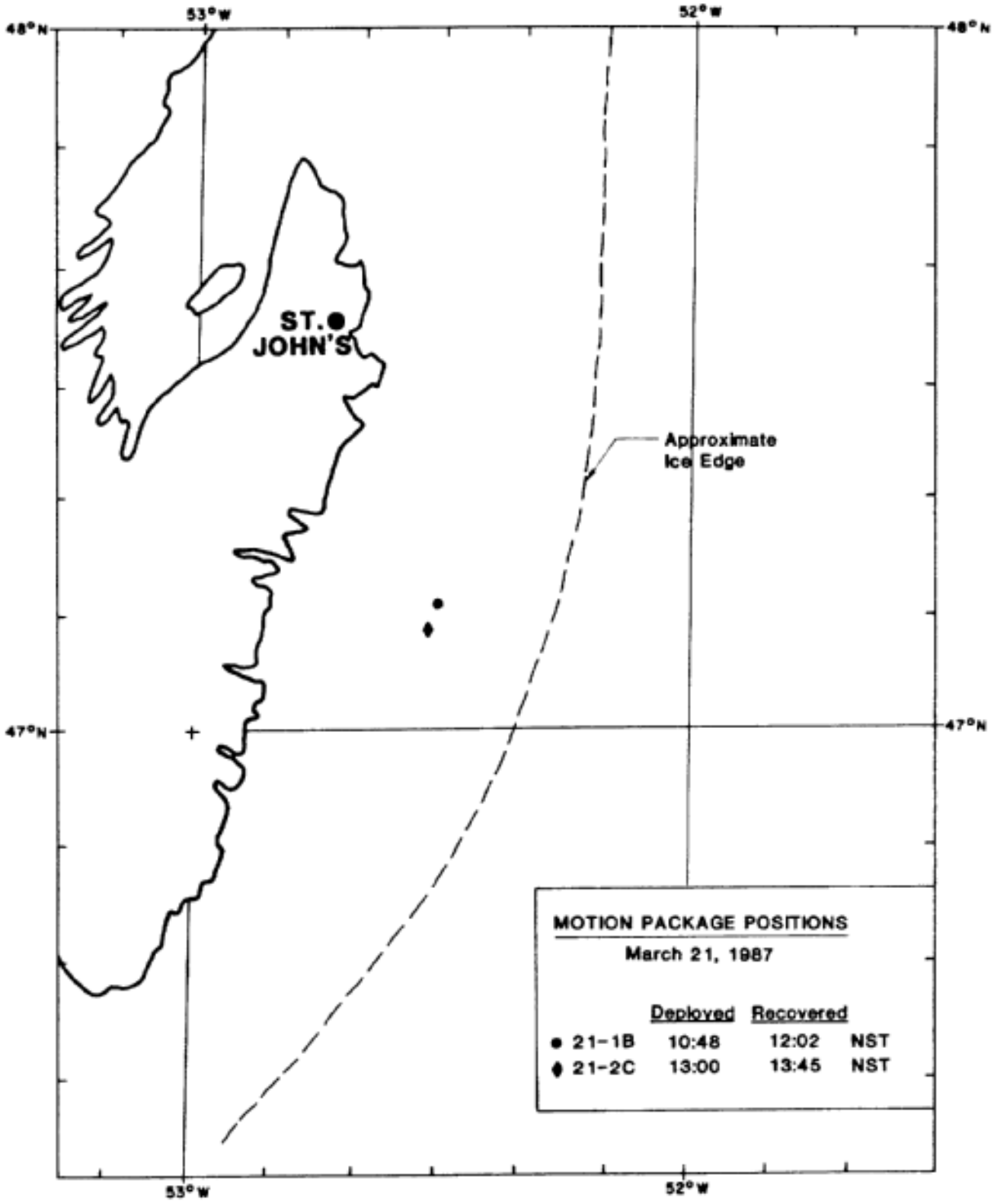
53°W
52°W
48°N
47°N
ST. JOHN'S
Approximate Ice Edge
MOTION PACKAGE POSITIONS
March 21, 1987
Deployed Recovered
21-1B 10:48 12:02 NST
21-2C 13:00 13:45 NST

Figure 3.2

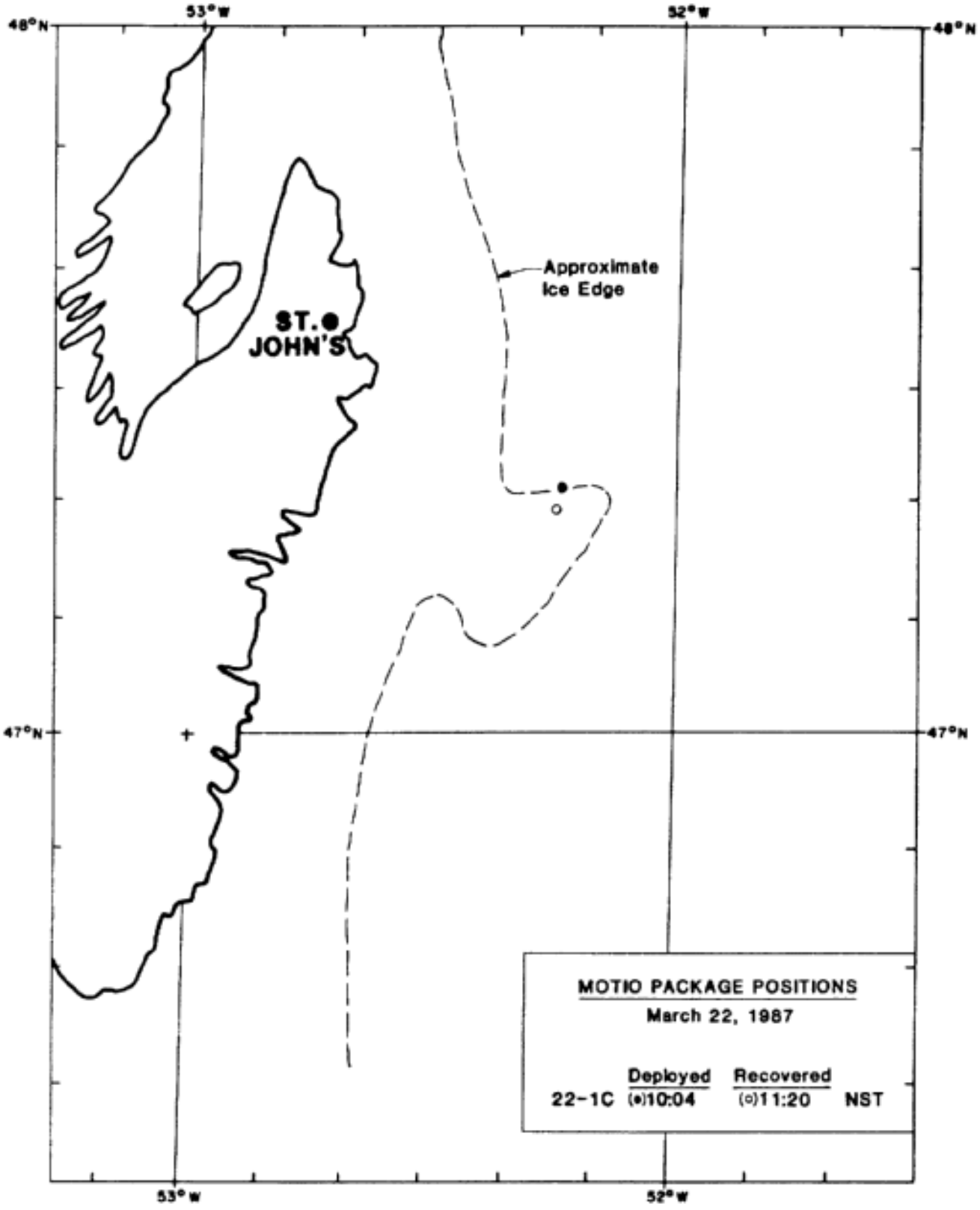

Figure 3.2 (con't)

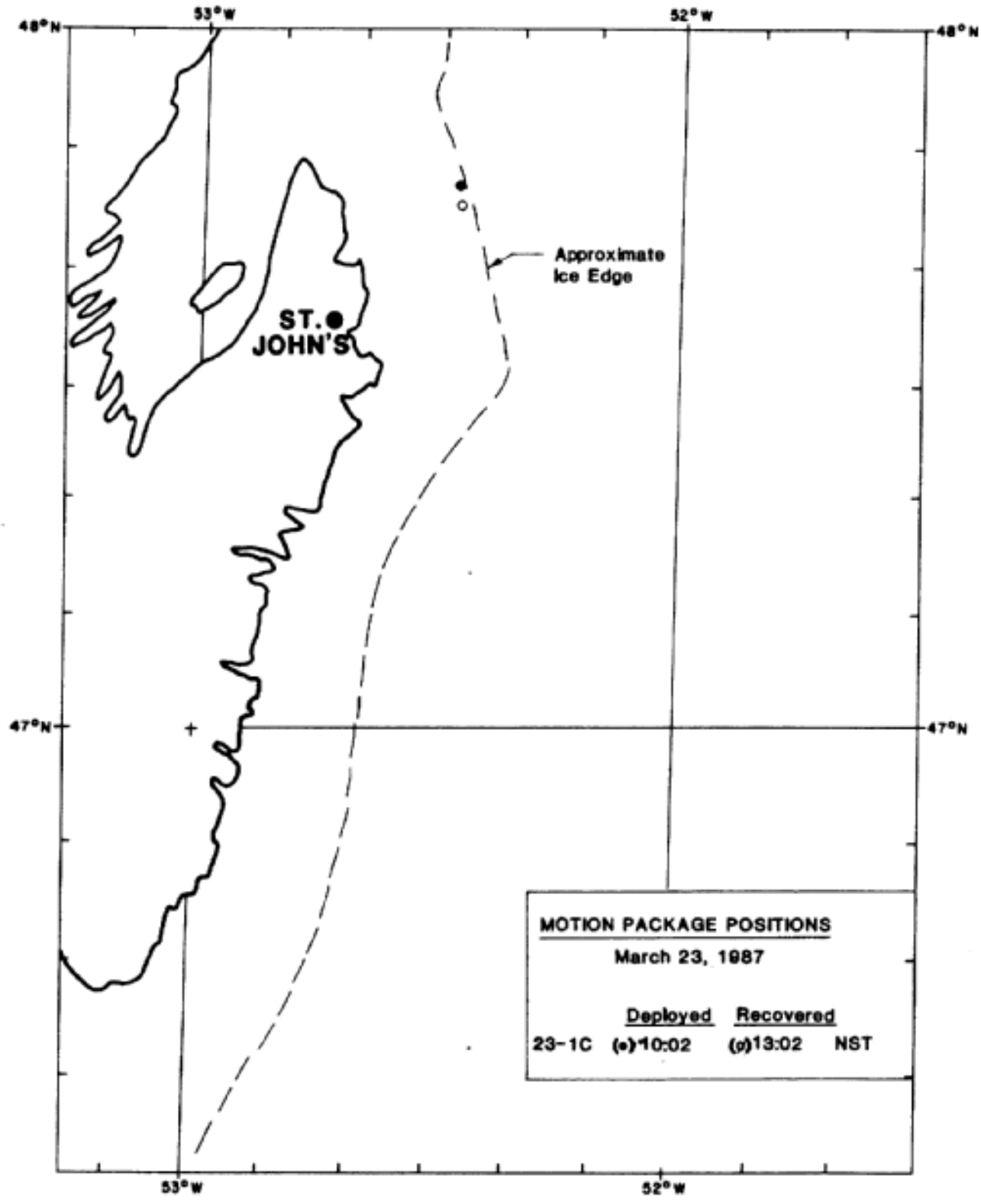

Figure 3.2 (con't)

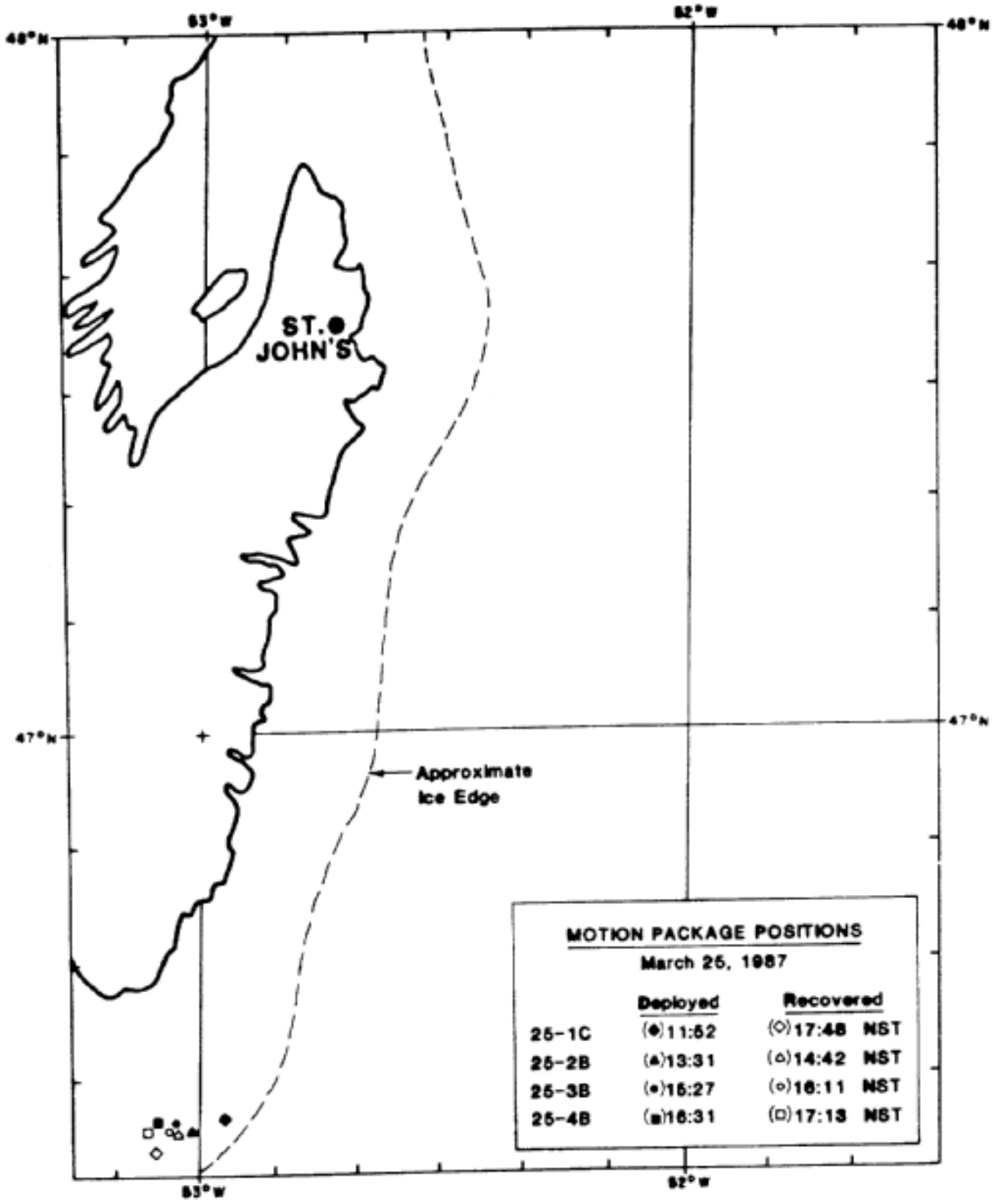

Figure 3.2 (con't)

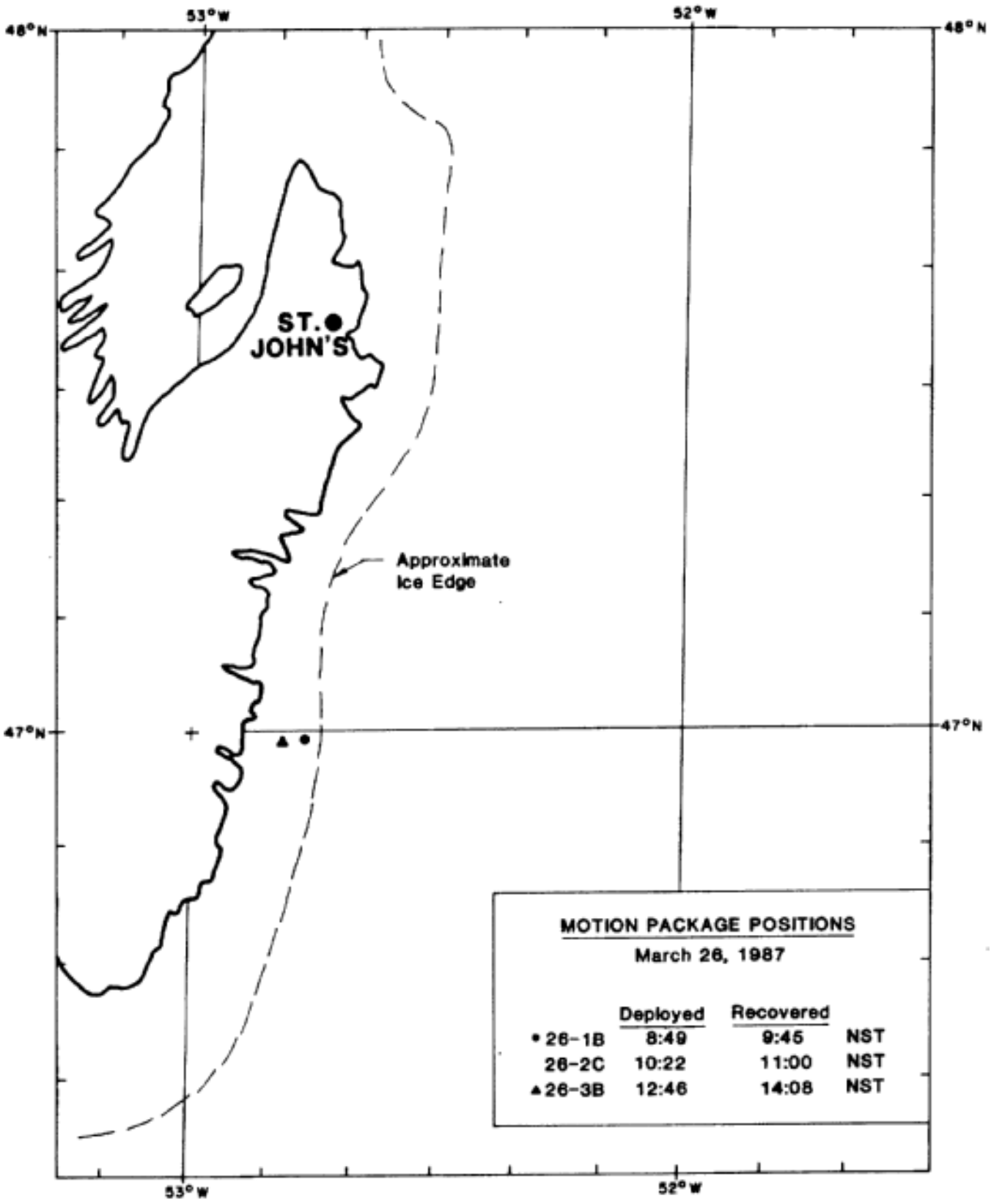

Figure 3.2 (con't)

Deployment 21–1B was placed on an ice floe within heavy pack ice. The ice was under pressure but the ship was able to break its way to open water later that day. The package was carried 30m away from the side of the ship. The relative motion within the ice was small but perceivable. The ice party could move easily between the component floes. There was a small lateral movement between the distinct floes; in the order of 50 to 100mm. At this time the ice cover was 95+ % distinct floes, Package C was substituted for Package B, test number 21–2C. when it was discovered that Package B had stopped recording. Later it was established that data had been collected during test 21–1B before the battery failed. The faulty battery of Package B was refurbished for the later test series of 25–XX and 26–XX. 21–1B and 21–1C were collected for different time periods from the same floe.

Deployment 22–1C was similar to the earlier 19–1B in a strip of sea ice of separate floes and a water boundary around all the floes. Adjacent floes were not touching or colliding. There was a two metre swell running within the ice cover. The ship moved 800 to 1,000 m away from the motion package while the data was collected. It was difficult to maneuver the ship among these small dynamic floes to recover the motion package in the moderate seas encountered. There was too much ice to employ a launch to aid with the recovery. The waverider buoy was put out in the open water adjacent to this strip of sea ice before or during the 22–1C ice motion package record.

Test 23–1C, the package was deployed in heavy ice about 700 to 900 m from the ice edge. There was a large concentration of ground or brash ice, apple sauce, providing the matrix material, filling between the distance floes to form the hundred percent ice cover. The ice floes were not packed close enough to permit safe movement of personnel from floe and floe. The ship moved back to open water and the waverider was deployed There was an helicopter aerial photography line from the ice edge to land that flew over the motion package location. This will provide a detailed description of the ice edge just after the motion package had been recovered. A second deployment had been planned for March 23 but the data recorder had stopped and the problem was not corrected until after the ship was ready to move off location. Later, it was discovered that the data from the ice package was unrecoverable.

Data collections 25–1C, 25–2B, 25–3B and 25–4B comprise an experiment to measure wave penetration into the ice cover. The experiment was conducted southeast of Cape Race. The ice cover was not constrained by any land boundary down wind. Deployment 25–1C was on a small floe close to the ice edge, 200 to 300 m from the edge. Package C which could collect data for several hours was used at 25–1C. It was left at its position near the ice edge for the duration of the day’s programme. The plan was to place Package B at positions 1, 2, and 4 km

into the ice cover from the ice edge, to measure wave penetration into the ice cover. The actual locations for the deployments are provided by ship's track log. The whole ice sheet was moving to the southwest throughout the day. The overall ice drift, will be available from the vessel track log and the sea ice drift tracks measured by the Omegasonde ice tracking programme of the Alfred–Wegener–Institut Fur Polar–Und Merresforschung.

The ice condition was heavy pack but with considerable ground or brash ice between the floes. It was possible to place a portable wooden bridge between the floes. Hence, the ice party was able to measure the ice thickness for ice stations 25–3B and 25–4B and to connect the line to recover the package. The motion package was left undisturbed on each floe during the data collection. The ship moved about 300 or 400 m away while the wave induced ice motion records were collected, Package B's data tape was changed after 25–2B. The same data tape was employed for measurements 25–3B and 25–4B. The ice condition changed to heavier floe concentrations as the ship proceeded away from the ice edge. There is a line of helicopter aerial photographs from the ice edge to Cape Race (essentially perpendicular to the ice edge), that will give a detailed description for the ice conditions for motion measurements. Low overcast limited flying altitude to 300 m and 1:3,800 scale for the film.

The waverider buoy was deployed at the ice edge after trial 25–1C had begun but before the series 25–2B, 25–3B and 25–4B. Unfortunately, wave data was not recovered from this deployment. The observed wave height attenuated with distance into the pack but was still evident at station 25–4B. The pack was not under pressure and the ship could turn and proceed at 6 knots . A summary of the waverider buoy measurements is given in Table 3.3 (after L. Thomas (1987)).

The ice motion set 26–1B, 26–2C, and 26–3B were collected adjacent to the ice edge east of Ferryland Head. There was land restraint to the west but there was no pressure evident in the ice field. The bays to the west were clear of ice. There was a high concentration of ground or brash ice between the floes. There were very light winds and a long period swell running in the ice cover. The magnitude of the swell did not appear to vary much with the ship's position from the ice edge. There is a line of helicopter aerial photography perpendicular to the ice edge from the shore side to the ice edge over the ship. This will provide detail of ice conditions for the ice motion tests. There was a Convair–5800 overflight with SAR imagery for the ice cover and for the ocean adjacent to the ice edge.

TABLE 3.3 Defft Waverider Buoy Measurements taken aboard CSS BAFFIN
(after L. Thomas of David Taylor Navel Ship Research & Development Centre, 1987)

Deployment	Location lat.(N)	long.(W)	Date 1987	Time (GMT)	Distance to Ice Edge (m)	Ice Concentration	H_s(m)		T_p(s)
1	47°03.2'	51°54.9'	19 March	1700	500*	8/10	2.4	(+.7/-0.5)**	8.0
2	47°06.2'	52°26.3'	21 March	1655	500	10/10	2.4	(+.7/-0.5)	10.7
3	47°20.4'	52°15.4'	22 March	1350	500	9/10	2.3	(+.7/-.4)	9.2
4	47°49.92'	52°22.51'	23 March	1455	3000	10/10	2.4	(+.7/-.5)	10.7
5	47°49.95'	52°22.53'	23 March	1530	600	10/10	2.5	(+.8/-.5)	9.2

* This wave measurement was taken in an open lead 500 m inside the ice pack.
All other measurements were made outside the MIZ in open water.

** 95% Confidence Band.

3.3 AERIAL PHOTOGRAPHY

A photographic record of the ice conditions encountered during the LIMEX cruise was collected. The photography referenced here is supplemented by the many photographs taken by the individual researchers. The helicopter was fitted with a camera mount and vertical looking camera to record some low level aerial photography. There was also a programme of oblique photography conducted from the ship. This was planned to supplement the aerial work supplying photography of ice conditions when visibility was unacceptable for flying. A copy of the photographs is given in a separate binder.

The flight lines for the helicopter aerial photographs were flown as single transect lines to record the change of ice conditions along each line. The aircraft altitude was established at 610 metres or what the cloud ceiling would permit up to 610 meters. The camera system employed was a 70 m Hasselblad, with 80 mm local length lens. An EL500 body with electric shutter and film advance was used to take the aerial photographs. 300 frames could be taken with a single charge of the internal NiCd batteries. The film used was the KODAK 70 mm Plus-X. Black and White Aerographic Film 2402 (ESTAR Base). The bulk film was loaded into re-loadable cassettes for the 70 shot camera back. The thin aerographic film permitted about 100 frames per film cassette. At the 1:7,600 scale, the single frame coverage is 418 x 418 metres. At the 1:3,800 scale, the single frame coverage is 209 x 209 metres.

The locations of the flight lines for the ten cassettes of helicopter aerial photography are summarized in Table 3.4 . Photography Series AR-1 was a section across the pack ice from the seaward edge to land

at Bay Bulls, AR–2 was similar to AR–1 a day later with land–fall at Flat Rock, AR–3 was a transect along the drift axis of the ice cover; the inshore section at a time when the ice was under considerable pressure, Photography Series AR–4 is a second section along the drift axis of the ice, the offshore section, AR–2 is the photography series along the flight line for the SAR imagery over the ship to the shore on March 21. The last 30 frames of AR–4 is the line perpendicular to the same SAR Flight line, AR–4 includes a series of frames along the ice edge north of the ship position.

The photography line AR–5 was flown across the pack ice from the ice edge to Cape Race. Easterly wind was pressuring the ice on the southern shore of the Avalon during this period. Line AR–6 was flown further west of AR–5 where the pack was no longer experiencing any land constraint to the west. Series AR–7 was flown along the ice edge; back toward where the ice was constrained by the Avalon shore.

Table 3.4 Aerial Photography Flight Lines

Photo Series	Date time (NST)	Lat dec°	Long dec°	Bearing *ang in deg*	Length	Scale	Frames
AR-1	22/03/87 1545h	47.263	52.773	090	40.8	1:7,600	71
AR-2	23/03/87 1230h	47.705	52.697	090	20.4	1:7,600	76
AR-3	1255h	47.705	52.697	159	41.6	1:7,600	83
AR-4	1320h	47.704	52.421	188	39.3	1:7,600	94
AR-5	25/03/87 1302h	46.663	53.063	171	24.4	1:3,800	97
AR-6	1315h	46.663	53.063	197	34.6	1:3,800	79
	1323h	46.366	53.197	057	6.0	1:3,800	16
AR-7	1329h	46.447	53.012	237	10.8	1:3,800	96
AR-8	26/03/87 0916h	46.993	52.771	193	46.3	1:7,600	90
AR-9	0934h	46.587	52.907	193	9.5	1:7,600	
	0941h	46.397	52.971	346	9.7	1:7,600	85
AR-10	0956h	46.553	53.025	346	6.7	1:7,600	21
	1013h	47.007	52.887	103	9.2	1:7,600	34
	1019h	47.038	52.771	193	16.2	1:7,600	47

AR–8 was flown along the centre line of the pack ice distributed along the Avalon shore, from Ferryland to Cape Race. AR–9 continues this line and then repeats the coverage from the ice edge to Cape Race, 20

hours later than line AR–5. The photography series AR–10 is a section across the ice strip from Ferryland head to the ice edge. This was followed by a second section over the ship parallel to the ice edge. The CONVAIR–580 collected SAR imagery over the AR–10 coverage later in the day. The aircraft overpass was scheduled for 1300 (NST). Tables A to J of aerial photography report (a separate binder) provides frame reference numbers and additional information on the ten helicopter aerial photography flight line film strips including negative numbering.

The oblique photography was taken with a C500 body with manual shutter and film advance. All the oblique photography was taken on Plus–X Professional 120 black and white film, with a square negative 12 shot camera back. There are frames of most of the floes used for Wave Induced Ice Motion package deployment. The oblique photography series includes photography of much of the on–ice activity. The coverage included deployment of the ARGOS drifting buoys, setting up the Omegasonde radio sondes, etc.

3.4 ICE SURFACE CHARACTERISTICS

The TexamTM Pressuremeter was employed to make sea ice strength measurements for the LIMEX Project. This equipment provides an index type strength measurement. Memorial University of Newfoundland's C–CORE and Engineering Faculty are investigating the application of the pressuremeter to make in situ ice strength determinations and to relate the field results with uniaxial and triaxial ice strengths. The pressuremeter employs a 75 mm diameter membrane probe with a hydraulic fluid reservoir. The membrane probe is pressurized with hydraulic fluid and exerts a circumferential load to the wall of a hole drilled in the material to be tested. For in situ tests, a 75 mm hole is drilled into the ice and the membrane until the probe

was seated in the hole and would stay in–place without any support. The pressuremeter test procedure used during the LIMEX Project was to pump a preselected volume of fluid into the probe and monitor the hydraulic pressure over a relaxation period. A series of fluid additions are made for a single test hole. The test is terminated when further fluid additions no–longer cause any change in the ice response to further load.

Table 3.5 provides a summary of the pressuremeter tests conducted for the LIMEX project (see also Figure 3.3 for locations). The sampling method was to measure ice strengths of as many different sea ice types as could be tested and/or identified. When time as an ice station permitted, two tests were conducted: one with the probe set vertically; and a second with the probe set at an angle. The angle of inclination was measured for each inclined test. A sea ice core was

taken from each pressuremeter tests site and returned to the University for further testing. One core removed from test Site 23–xG was sectioned for salinity analysis for that core is given in Table 3.6 . On March 21 and 22, the pressure meter tests were conducted on both distinct floes and on refrozen brash or ground ice. The ship was docked in pack ice under pressure during this period and the ice party could easily move between the ice floes forming the ice cover. After March 21, the ice strength test–work was conducted on single distinct floes and it was no longer practical to move around to sample the ice type of different floes. The brash between the floes made up a large portion of the ice cover and was fluid in nature. The set of 12 pressuremeter tests sampled all the distinct ice types encountered on the LIMEX Cruise. The strength records are not prepared for inclusion in this data report. The results will be part of a Masters Thesis (A. Steel, 1988).

From several aerial photographs, the distribution of ice floe size were determined as described in Section 5.0 .

Table 3.5 Summary of Pressuremeter Measurements

Test No.	Date time (NST)	Lat dec°	Long dec°	Angle	Ice thickness (metres)	Remarks
16-1A	16/03/87 0920h	47.0101	52.8076		1.00	Started
	1045h	47.0100	52.8101	Vertical		Completed
20-1B	20/03/87 0824h	47.4349	52.2693	Vertical	1.45	Started
20-2C	20/03/87			Inclined	1.45	
20-3C	20/03/87 1317h	47.4325	52.2852	Vertical	1.40	Completed
20-4D	20/03/87 1540h	47.4218	52.2964	Vertical	0.70	Probe through
21-1E	21/03/87 0937h	47.0004	52.2947	Vertical		Soft Ice
21-2F	21/03/87			Vertical		Surface Failure
21-3F	21/03/87 1400h			Inclined		Completed
23-1G	23/03/87 1005h			Vertical		Started
23-2G	23/03/87 1310h			Inclined		Completed
26-1H	26/03/87 1235h	46.973	52.793	Vertical		Started
26-2H	26/03/87 1420h			Inclined		Completed

Table 3.6 Salinity Profile Ice Station 23-xG: (*Salinity analysis conducted by Water Analysis Laboratory of CSS Baffin*)

Sample No.	Section mm	Salinity ppt
025401	50	0.226
025402	110	0.287
025403	170	0.806
025404	230	2.154
025405	340	2.520
025406	450	2.044
025407	560	3.213
025408	670	3.617
025409	780	3.915

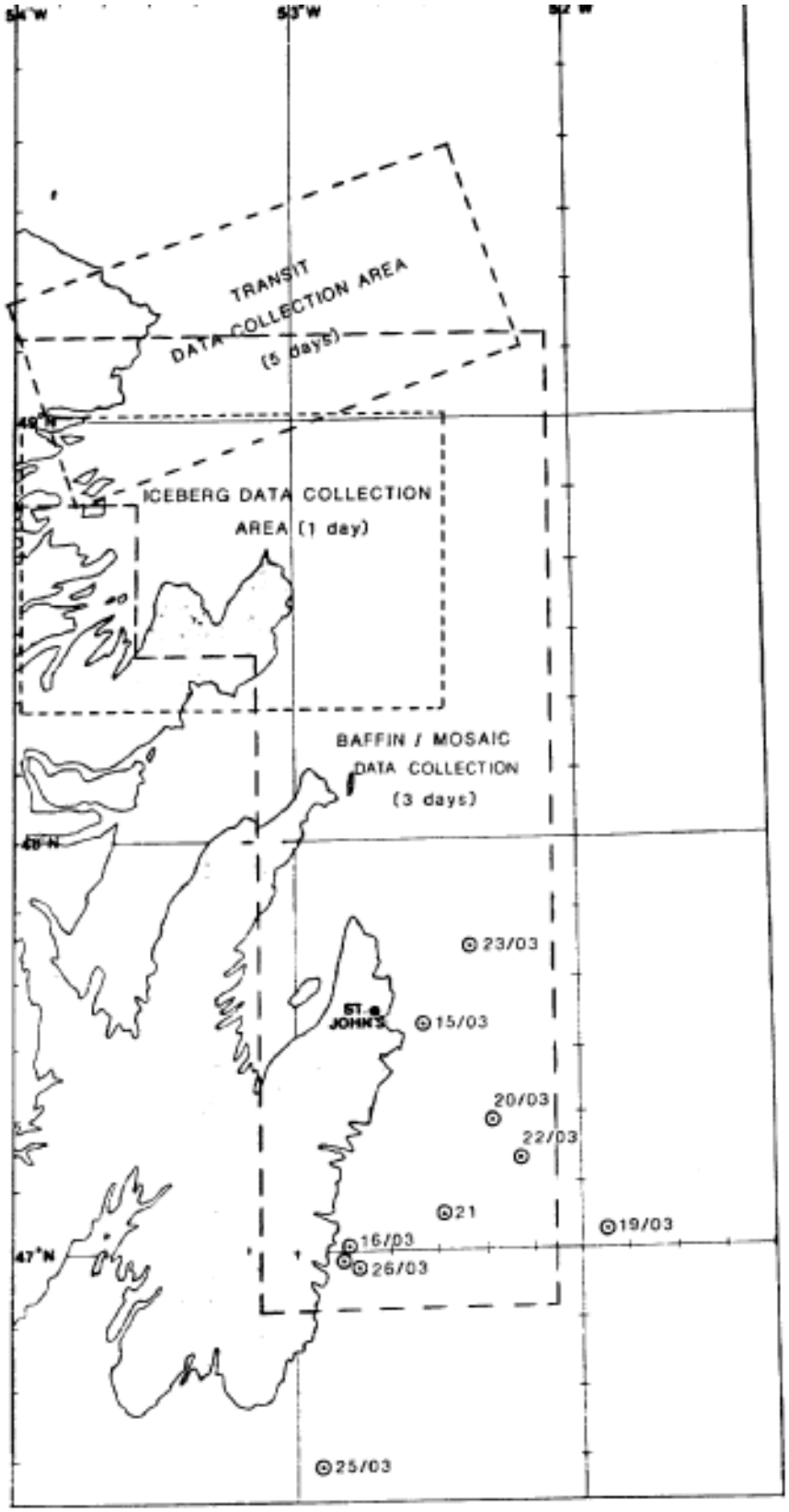

Figure 3.3 **Areas of SAR data collection and surface observations (● are BAFFIN sites for surface data collection)**
(Source: Sue Argus, CCRS)

3.5 SITE SPECIFIC WAVE FORECASTING

3.5.1 Background Introduction

The model used for the wave–forecasting is the Ocean Data Gathering Program (ODGP) which has been operational at Oceanweather Inc./MacLaren Plansearch since, mid–September 1983. The model is a fully directional, spectral, deep–water wave model.

The ODGP wave model has been adopted for use in an operational wave analysis and forecast system, on the grid system shown in Figure 3.4 . A nested grid (fine grid), in which the grid spacing is half that of the course, extends over the Scotian Shelf and the Grand Banks of Newfoundland.

The ODGP wave hindcast model evolved from the Spectral Ocean Wave Model of the U.S. Navy (SOWM) about a decade ago. Details of both the ODGP and SOWM models are given in MacLaren Plansearch Limited (1985). The ODGP model has since been tested against a broader range of wave regimes than any other existing model. This model incorporates a relatively simple representation of the source terms in the spectral energy balance equation compared to more recent formulations. The calibration of these parameterizations has remained stable over this period, unlike most contemporary models, which appear to undergo continuous tuning.

Before 1983, the ODGP model has been exercised mainly in hindcast studies of extreme wave regimes, albeit of many different types (e.g, winter cyclones, typhoons, hurricanes, and monsoon surges). Reece and Cardone (1982) summarized this extensive model experience and reported a record of hindcast skill unequalled by alternate models. The model, when driven by wind fields of accuracy about ±2 m/s in speed, ±20° in direction, provided unbiased specifications of significant wave height and peak frequency with a scatter of about 10%. which, incidentally, is comparable to the scatter in estimates of these quantities from measured 20–min wave records. Wherever possible, hindcast frequency and directional spectra have also compared and agreed. The model exhibits conspicuous skill in the specification of the complicated directional mix of local sea, and propagation swell excited by the moving, quasi–circular wind fields of migratory extratropical and tropical storms.

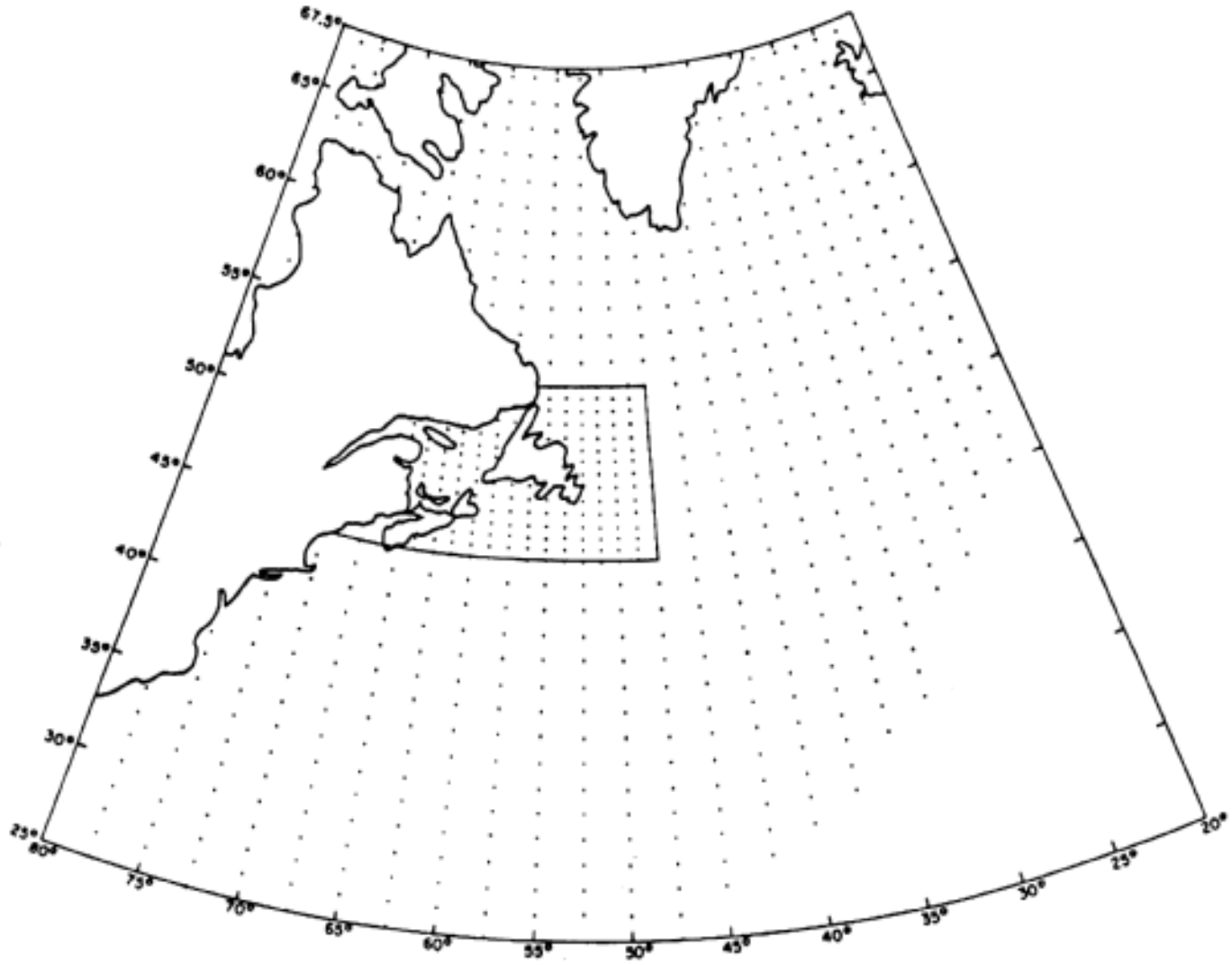

Figure 3.4 Operational ODGP wave forecast model grid.

We regard the general problem of wave climate specification in Canadian east coast waters as basically a two–scale problem. The largest scale requires a grid of about 100–km spacing covering most of the North Atlantic Ocean (e.g., the ODGP coarse grid). The second scale requires a grid of no more than about 50–km spacing (e.g., the ODGP fine grid) to resolve large islands and capes and irregular shoreline geometry, large–scale ice cover effects, and smaller scale features in the wind field. Given that the typical shelf width offshore (to depths of 50 m) in Canadian east coast waters of interest is in the order of 50 km, or one grid spacing on the fine grid, it is appropriate that the coarse and fine grid scales be treated as deep water.

3.5.2 ODGP DEEP–WATER MODEL ALGORITHM

Only a very brief summary is presented here,For detailed description of the model, the reader is referred to Cardone et al (1976) and MacLaren Plansearch (1985). The general energy–balance equation for wave evolution is given by:

$$\frac{\partial}{\partial t} S(f,\theta;x,t) + Cg.\ \nabla S = F(f,\theta;x,t) \qquad (1)$$

Where:

$S=S(f,\Theta;x,t)$ is the two–dimensional wave spectrum as a function of frequency (f) and direction (Θ) at a given location (x) and time (t);

$C_g=C_g\ (f,\Theta)$ is the deep–water group velocity;

$F(f,\Theta;x,t)$ is the source function which represents all physical processes that transfer energy from or to the spectrum.

The source function may be expressed as a sun of three terms:

$$F = F_{in} + F_{nl} + F_{ds}$$

Where: F_{in} = energy input function by wind,
F_{nl} = non–linear transfer by wave–wave interaction,
F_{ds} = energy dissipation term.

The input source function (F_{in}) is represented in ODGP as a function of wind speed and frequency according to the linear equation:

$$Fin = A + B.S$$

The A term in the above equation $=A(f_i,u)$ is a function of frequency f and wind speed u. This term represents Phillips' external turbulent pressure forcing. The B.S term corresponds to Miles' linear feedback

mechanism. The term $B(f_i,u^*)$ is expressed in ODGP as a function of frequency and the friction velocity u*.

The energy transfer associated with the non–linear wave–wave interaction is not explicitly included in ODGP.

In general, hindcast models work by applying alternate steps to model the effects of propagation and growth. In the propagation step, the frequency bands of the model are totally uncoupled, and the directional bands are weakly coupled by convergence of meridians on aspherical earth. In the growth step, the grid points are totally uncoupled; the frequency and direction bins at one grid point are coupled because of the treatment of the source and sink terms in the spectral energy balance equation.

The propagation scheme used in the ODGP operational model was constructed for use with a spherical earth, and combines elements of jump and interpolatory propagation. When an ocean basin is mapped on a plane by an arbitrary projection, and a rectangular or triangular grid overlaid, the distance from each point to its neighbours, and thus the coefficients in the propagation formula, are functions of both latitude and longitude. Coefficients dependent on latitude alone arise when one set of grid lines is meridians equally spaced, and the other set parallels at any convenient spacing.

The present grid is that used in the North Atlantic wave hindcast/ forecast model referred to above (MacLaren Plansearch 1985). That grid system is shown in Figure 3.4 . The grid consists of a coarse grid of spacing 1.25° latitude and 2.50° longitude, extending from 25°N to 67.5°N and from 20°W to 80°W, and a nested grid in which the grid spacing is half that of the coarse (i.e., 0.625° by 1.25°). The time step of the model is 2 hours, each of which consists of a full time step of propagation between two half time steps of growth. The present model has 24 directional bands spaced 15 degrees apart and 15 frequency bands spaced as shown in Table 3.7 .

The ODGP growth algorithm developed by Cardone, Pierson, and Ward (1976), is a part of the family of PTB discrete–type spectral models described by Pierson, Tick, and Baer (1966). While the ODGP spectral growth/dissipation algorithm is of the PTB type, significant differences between it and the U.S. Navy SOWM model (also a PTB type) evolved in the application and verification of the ODGP model against measured wave spectra in hurricanes. An important difference is in the calculation of the wave growth as a function of the angle between the wave direction and wind direction. In the SOWM, the energy in a given frequency component summed within +/–90 degrees of the local wind is the quantity subjected to growth. The incremental growth is then spread out over the same components.

In the ODGP model, each downwind spectral component is grown separately, and after computation of growth for all components within +/–90 degrees of the local wind direction, energy is redistributed over angles. This algorithm leads to slower growth of wave height with time in a turning wind than in a wind of constant direction.

TABLE 3.7

The 15 ODGP Frequency Bands

Band	Nominal Frequency (Hz)		Bandwidth (Hz)
1	7.285/180	= 0.0405	0.43/180
2	16/360	0.04444	1/180
3	18/360	0.05000	1/180
4	20/360	0.05556	1/180
5	22/360	0.06111	1/180
6	24/360	0.06667	1/180
7	26/360	0.07222	1/180
8	29/360	0.08056	1/ 90
9	33/360	0.09167	1/ 90
10	37/360	0.10278	1/ 90
11	42/360	0.11667	1/ 60
12	48/360	0.13333	1/ 60
13	57/360	0.15833	1/ 30
14	75/360	0.20833	1/ 15
15	111/360	0.30833	2/ 15

The modelling of directional processes in the ODGP model is apparently sufficient to provide reasonably skilled simulation of the integrated properties of the directional spectrum of peak sea states in storms characterized by stationary or moving circular wind fields. In over 60 individual comparisons in 19 different storms. Reece and Cardone (1982) found that the model exhibited negligible bias and rms errors

of less than 1 m in significant wave heights and 1 second in peak spectral period.

3.5.3 Input Winds

Winds are provided to the wave model from sea level pressure analysis and forecast fields which are derived in a man–machine procedure from NOAA NMC facsimile products. A Marine Planetary Boundary Layer Model(MPBL) is used to specify the winds from sea level pressure gradients.

The basis of the sea level pressure analyses, which are used to generate the wave analysis in the real–time hindcast/update part of each forecast cycle, is the NMC North Atlantic surface pressure map distributed over the DIFAX network at 6–hourly intervals. This map is a section of a Northern Hemisphere Polar Stereographic projection of scale 1:10,000,000 on which are shown computer plotted land and surface ship reports and hand analyzed isobars drawn at 4 mb intervals. Positions of lows, highs and fronts are also indicated.

This chart has a data cut–off of about 1 hour and the maps are received about 4 hours after nominal map time (0000Z, 0600Z, 1200Z, 1800Z). At NMC, a so–called Final Analysis is performed about 5 hours after map time but these analyses are not distributed in real time.

At Oceanweather, there is sufficient time before the NMC forecast products are received to add ship reports transmitted over the GTS up to about 9 hours after map time for the 0600 GMT and 1800 GMT and about 3 hours after map time for the 0000 GMT and 1200 GMT analyses.

Such reports are plotted manually directly onto the DIFAX maps and the isobaric pattern is redrawn where the late data support modification of the NMC analysis.

The pressure fields are then digitized over the domain of the wave model using a digitizing table. The procedure involves digitization of locations of centers of action and their central pressures and of each isobar. An objective analysis program then recovers pressures on a regular grid of points spaced .625° in latitude and 1.250° in longitude.

Forecast wind fields are specified at 12–hourly intervals between t_o (analysis time) +12 hours through t_o + 48 hours, from 12–hourly surface pressure fields provided by the NOAA Nested Grid Model (NGM). Before the pressure fields are digitized, however, the isobaric patterns are modified through forecaster intervention in an attempt to remove systematic errors in specification of cyclone and anticyclone central pressures and corresponding pressure gradients. Initialization and persistence errors are also accounted for at this step. Wind

fields are calculated from the modified pressure fields, using the same MPBL applied to the analysis pressure fields.

The MPBL model applied is an improved and updated version of the model proposed by Cardone (1969). The model has been found by numerous investigators to effectively link the external factors governing the MPBL to the near surface wind structure. Those external factors, in a steady state horizontally homogeneous MPBL, may be listed as follows:

- latitude (or Coriolis parameter, f)
- surface roughness parameters, z_o
- air–sea temperature differences $T_a - T_s$
- geostrophic wind vector, V_g
- horizontal temperature gradient ∇Ta

The model considers the MPBL as consisting of two layers. In the lower layer, the wind and temperature variation with height is governed by the effective roughness of the surface and the heat flux across the air–sea interface. The similarity theory of Monin–Obukov is applied there to provide a framework for the description of the mean wind profile. The theory is quasi–empirical in that general expressions are formulated from dimensional considerations and constants that appear in the expressions are derived from experimental data, Variations in the mean wind with height, Z, in the layer are related to u, z_o, and the Monin–Obukov length, L, which is a function of both u and the heat flux.

4.0 LEWEX/LIMEX WIND/WAVE HINDCAST

After the experiment, all available meteorlogical data was used to reanalyze the wind fields during the LIMEX/LEWEX study period.

For the wind/wave hindcast the model domain was extended as shown in Figure 4.1 . The new model domain extends from 25° – 67.5°N, 20°–80°W with grid spacing every 1.25° latitude and 2.5° longitude. The fine mesh grid was also extended to 40° – 52.5°N and 45° – 75°W with grid spacing every 0.625° latitude and 1.25° longitude.

4.1 WIND HINDCAST

The wind fields produced by the wind model were adjusted by performing a kinematic analysis over the fine mesh region of the domain. The kinematic analysis replaced calculated winds with measured winds in the fine mesh region wherever possible.

The reanalyzed wind fields consist of wind speeds and directions at each grid point every 6 hours. The wind speeds are effectively neutral winds at 20 m height.

The wind fields were reanalyzed during the following time periods.

- LEWEX: 1987/03/09 1800z to 87/03/19 1800z
- LIMEX: 1987/03/19 1800z to 87/03/26 1800z

The start of the LEWEX period coincided with the establishment of a strong blocking pattern in the central North Atlantic. This anomalous general circulation pattern strongly disturbed the normal pattern of cyclogenesis and storm movement throughout the LEWEX/LIMEX periods. During the LEWEX period, the blocking ridge was strong enough to cause cyclones to turn sharply northward and weaken rapidly off the east coast of Canada. During the LIMEX period, cyclones which formed off the east coast were able to penetrate the ridge and move northeastward along a more normal track, but their intensification remained rather limited until they approached Europe.

The general pattern of sea–level pressure weather systems during the LEWEX/LIMEX period is shown in the sequence of 1200 GMT surface maps (taken from the NOAA Final Analysis series). Early in the LEWEX period, on March 13th – 14th, a storm is seen to weaken rapidly as it drifts northward off the East Coast, at about 50W. This sequence created an elongated north–south trough of low pressure which divided the wind flow sharply between the Tydeman and Quest.

A second storm, which deepened south of Nova Scotia on the 15th, also turned sharply northward and filed with the center crossing eastern Newfoundland on the 17th. A third weather system followed the same evolution on the 19th and 20th.

The weak cyclone which formed over the U.S. East Coast on the 19th was the first in the series to penetrate the ridge on the 22nd. This and the following cyclone passed basically well south of Newfoundland, and together with high pressure building over the Maritimes between the 23rd and 26th, caused mainly light easterly winds in the LIMEX area.

4.2 WAVE HINDCAST

The hindcast wind fields were used to run the ODGP deep water model.

The LEWEX hindcast period is defined as the period 87030912 87031912. This run was started from flat calm initial sea–state conditions, but ample spinup was allowed before the interesting LEWEX wave data sets became available on the 14th.

The LIMEX wave hindcast period extended from 87031918 to 87032618 and was initialized from a file of restart spectra saved from the LEWEX wave hindcast run.

The wave hindcast runs produced archive files of fields over the whole grid of significant wave height, peak spectral period, and vector mean wave direction, and files of two dimensional wave spectra at selected points. Different points were selected in each run as follows (see Figure 4.2):

LEWEX RUN: 3469, 3536, 3590, 3716 (BOW DRILL 2). 3886, 3890 (QUEST), 3892 (TYDEMAN)

LIMEX RUN: 3469, 3536, 3590, 3716 (BOW DRILL 2), 3712, 3713, 3741, 3742, 3770, 3771, 3799, 3800, 3828, 3829

The wave model accepted one ice specification per run. Figures 4.2 and 4.3 indicate the ice edge adopted for each run.

We have also prepared the following graphical output summaries of each run:

1. time series of wind speed (20 m), wind direction, vector mean wave direction (going towards), significant wave height, and peak period at selected grid points (see Figures 4.4 , 4.5 and 4.6);

2. cluster plots (significant height and vector mean wave direction) at 12–hourly intervals over the coarse and fine grids, except we have excluded areas on the coarse grid north of 60N and south of 30°N as shown in Appendix C.

It should be mentioned here that the ODGP hindcast wind fields for the LEWEX period was delivered to several Modelers to run their wave models (e.g. GSOWM, ODGP, NOAA, 3GWAM, BIO, HYPA) using same winds. An intercomparison between the models results is currently underway by

Dr. Robert Beal of APL, who is also evaluating the models prediction against directional wave measurements both from in situ measurements (e.g. WAVEC, wavescan, Endco) and remote sensing (i.e. SAR. ROWS, SCR).

The ODGP wind and wave hindcast results were loaded onto a 9–track magnetic tape which was delivered to the Scientific Authority for the study.

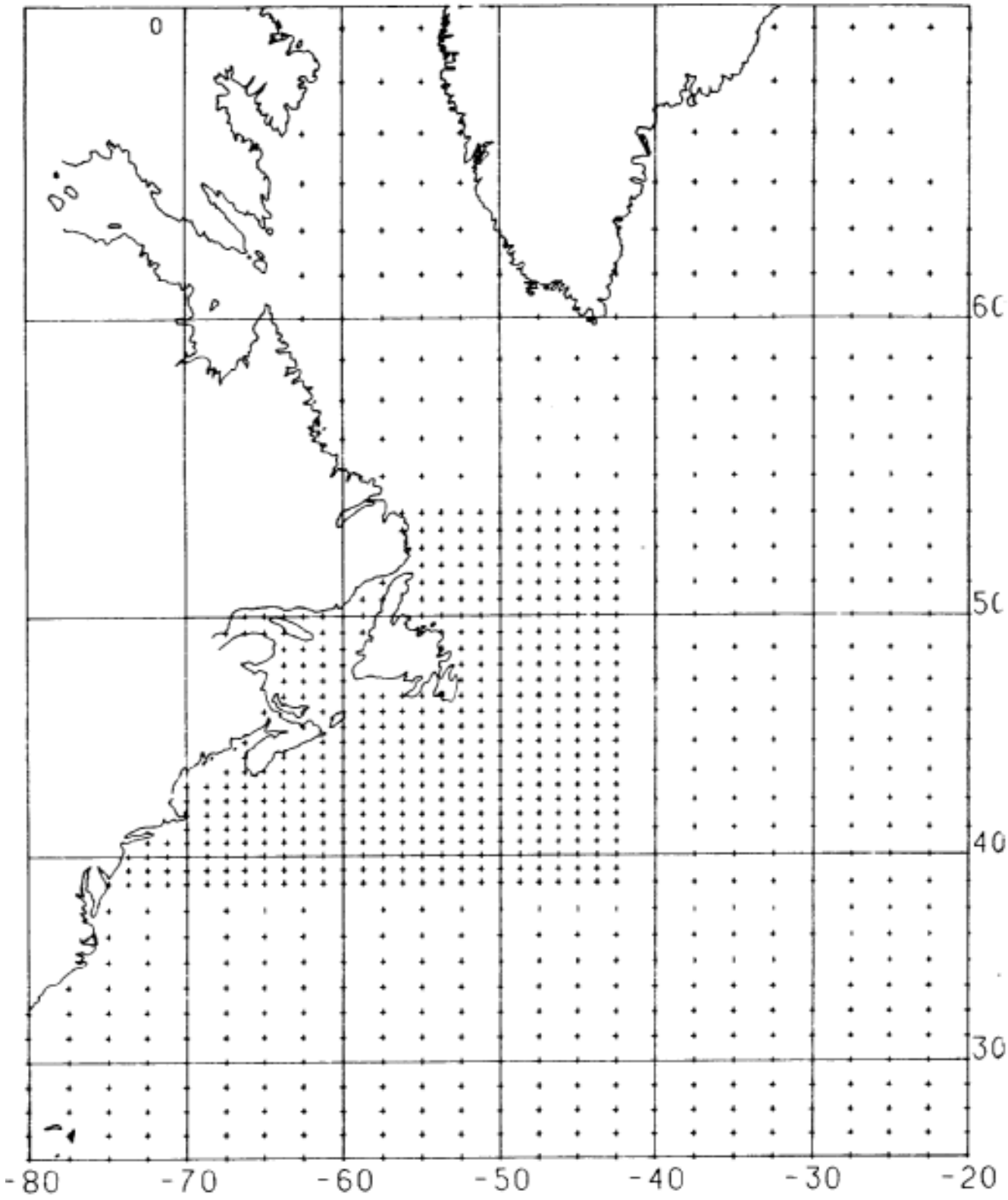

FIGURE 4.1 THE ODGP (LEWEX) MODEL GRID

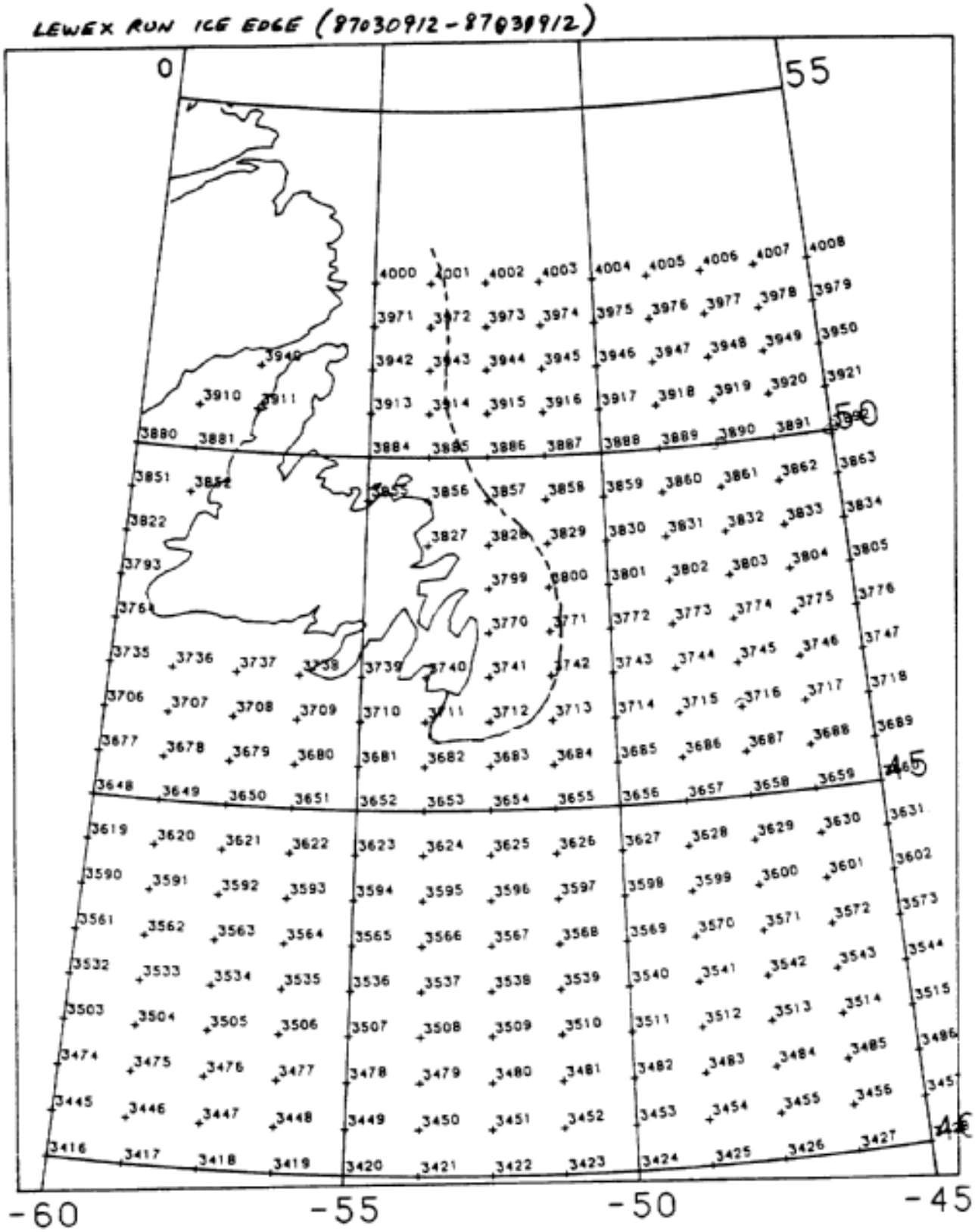

FIGURE 4.2

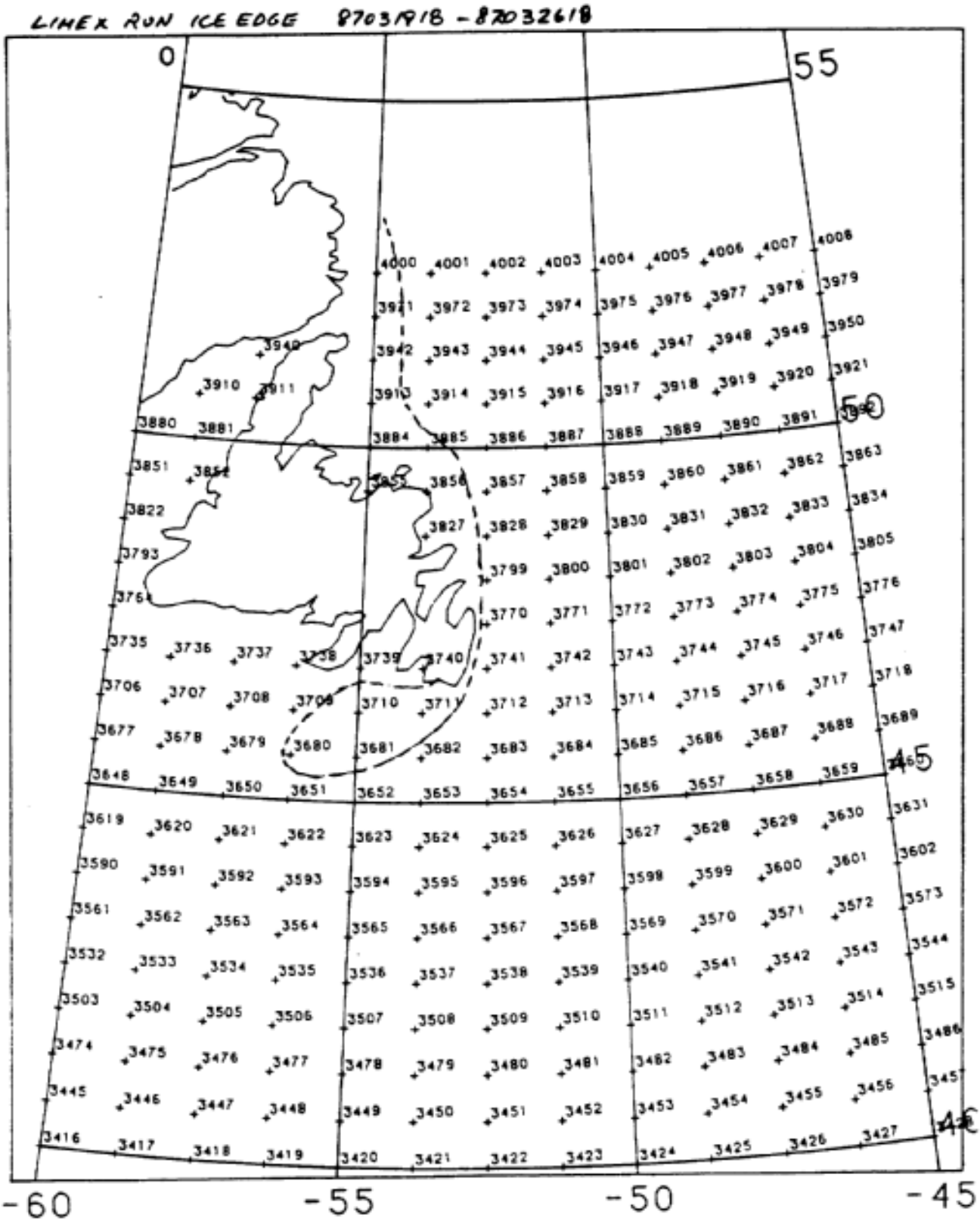

FIGURE 4.3

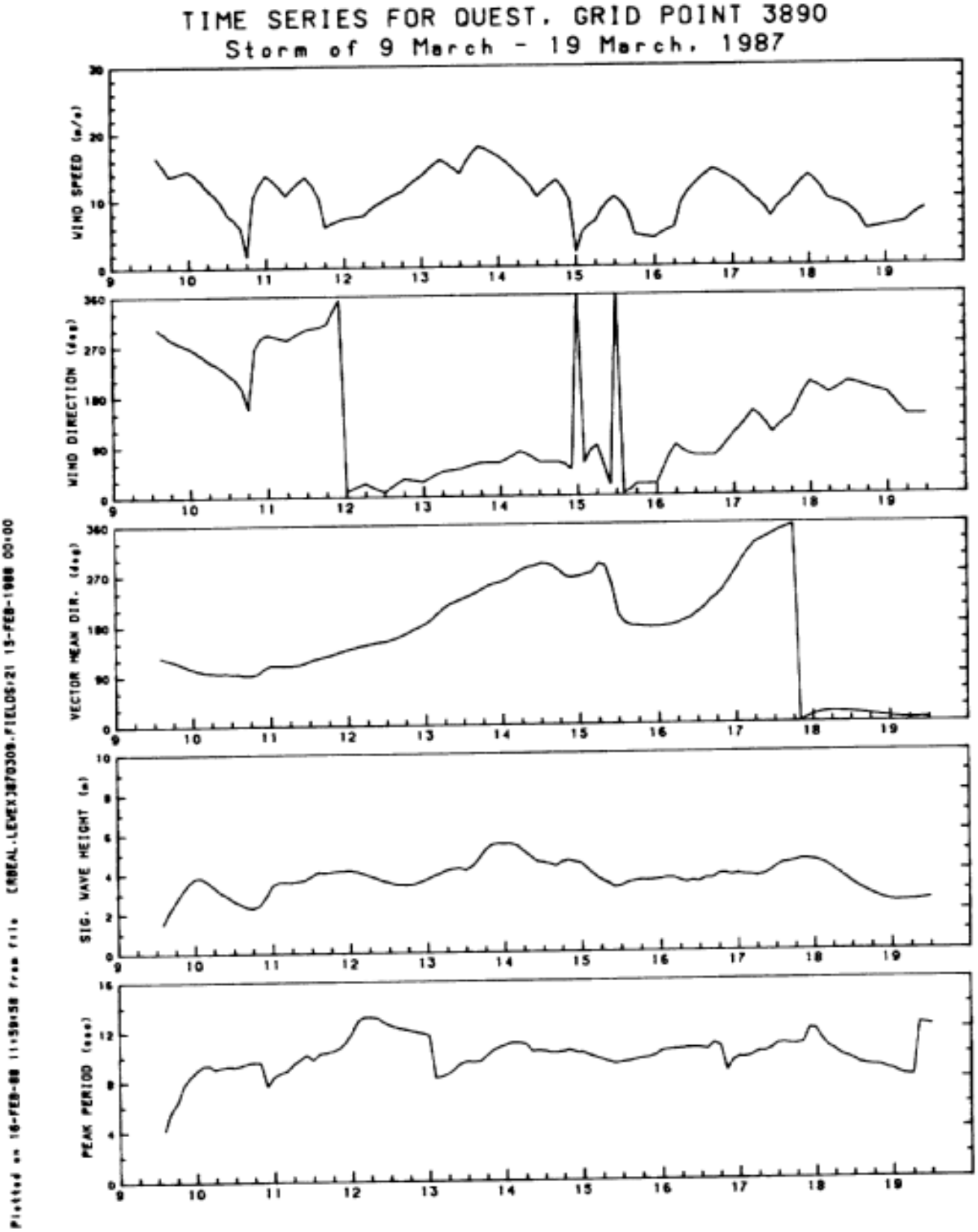
TIME SERIES FOR OUEST. GRID POINT 3890
Storm of 9 March - 19 March, 1987
WIND SPEED (m/s)
WIND DIRECTION (deg)
VECTOR MEAN DIR. (deg)
SIG. WAVE HEIGHT (m)
PEAK PERIOD (sec)
9
10
11
12
13
14
15
16
17
18
19
Plotted on 16-FEB-88 11:58:58 from file [OBEAL.LEVEX]870309.FIELDS;21 15-FEB-1988 00:00

Figure 4.4

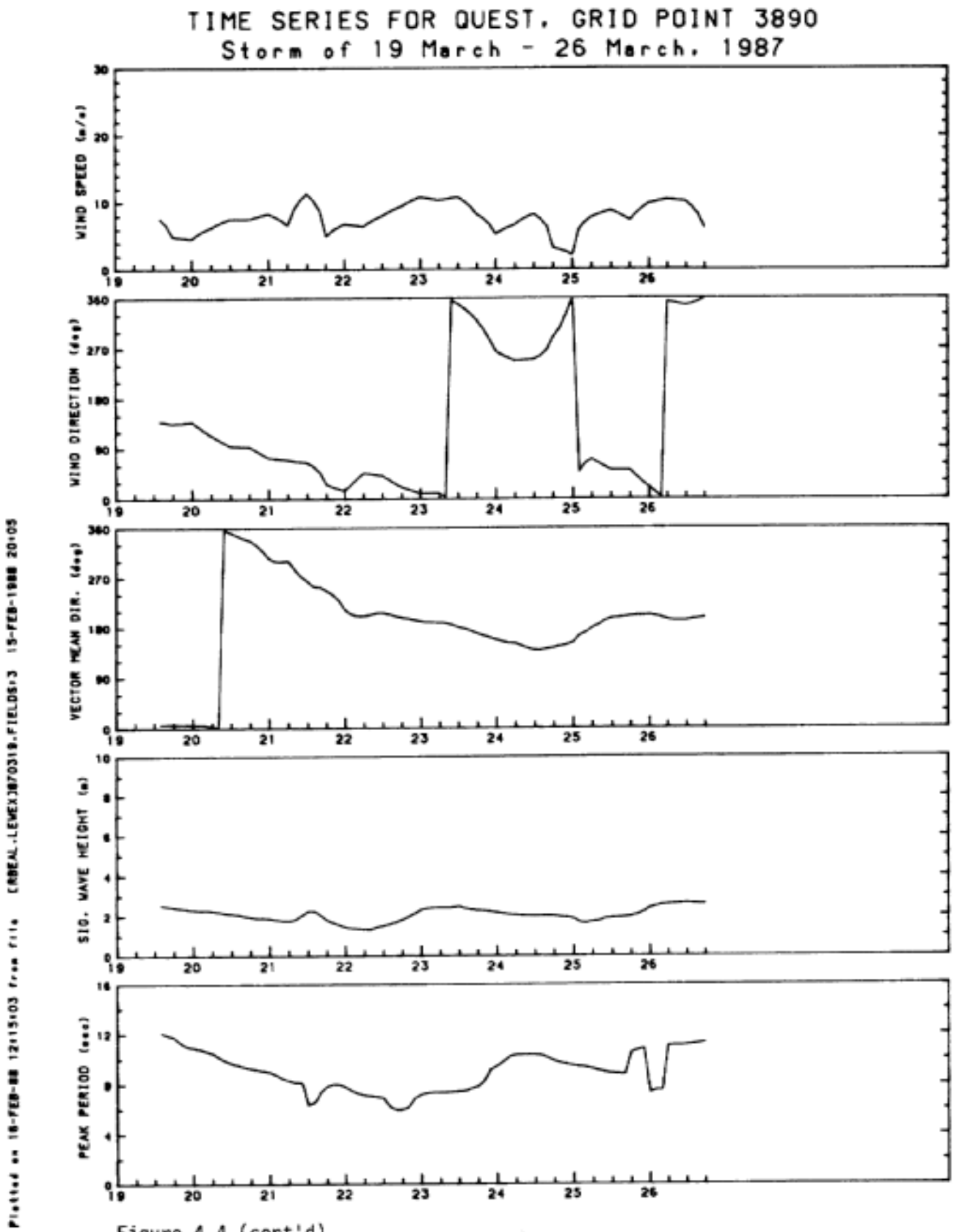

Figure 4.4 (cont'd)

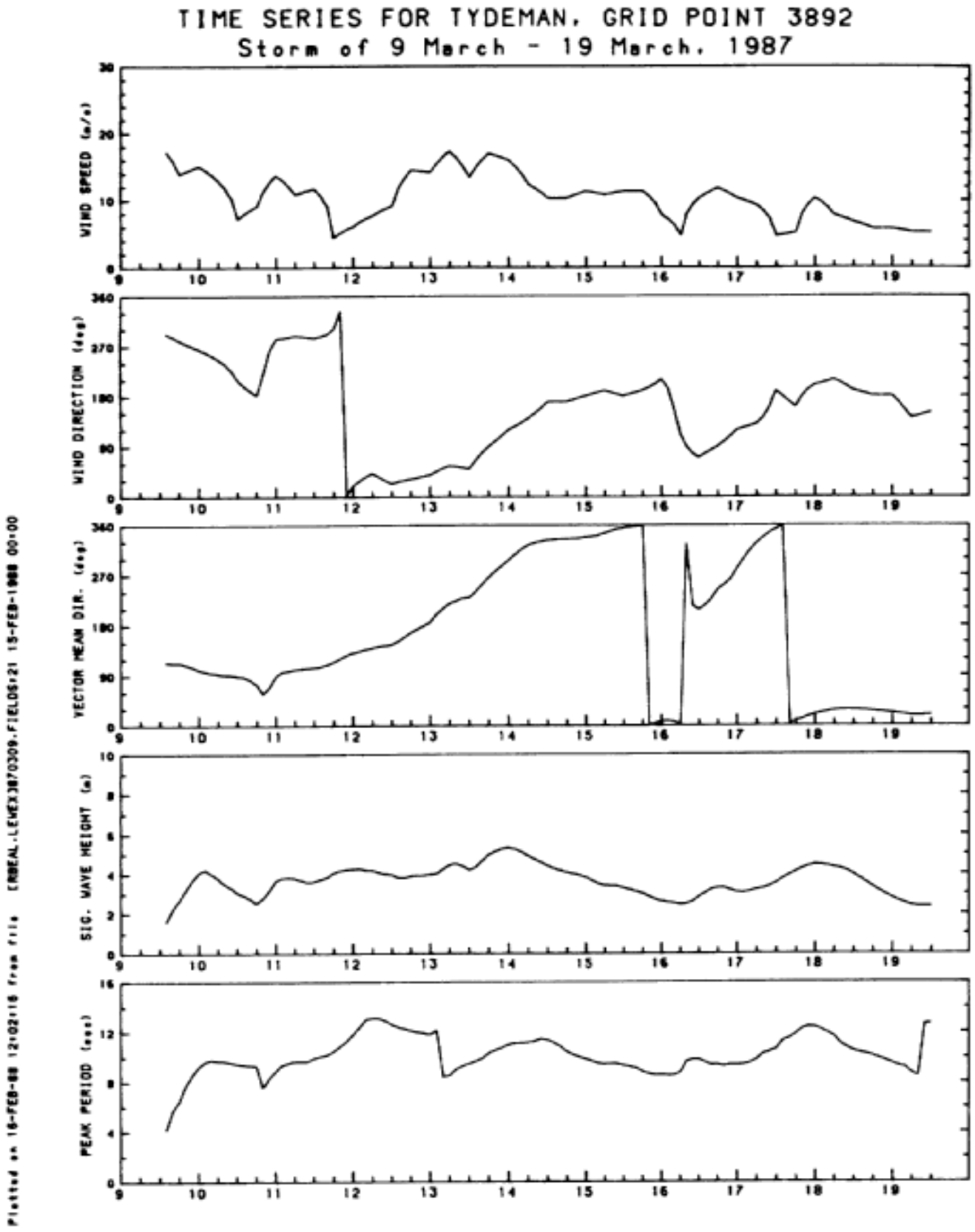
TIME SERIES FOR TYDEMAN, GRID POINT 3892
Storm of 9 March - 19 March, 1987
WIND SPEED (m/s)
WIND DIRECTION (deg)
VECTOR MEAN DIR. (deg)
SIG. WAVE HEIGHT (m)
PEAK PERIOD (sec)
9
10
11
12
13
14
15
16
17
18
19

Figure 4.5

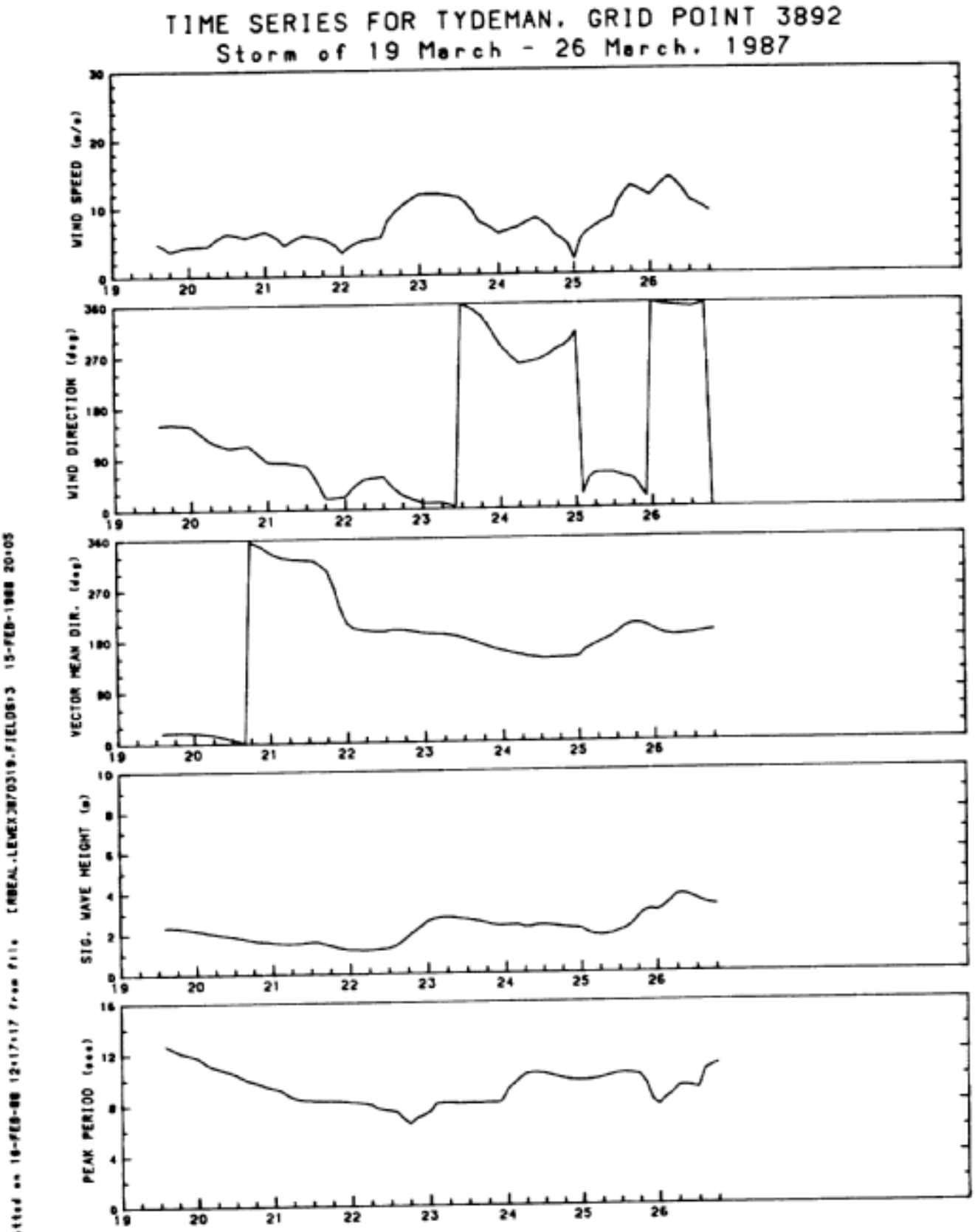

FIGURE 4.5 (con't)

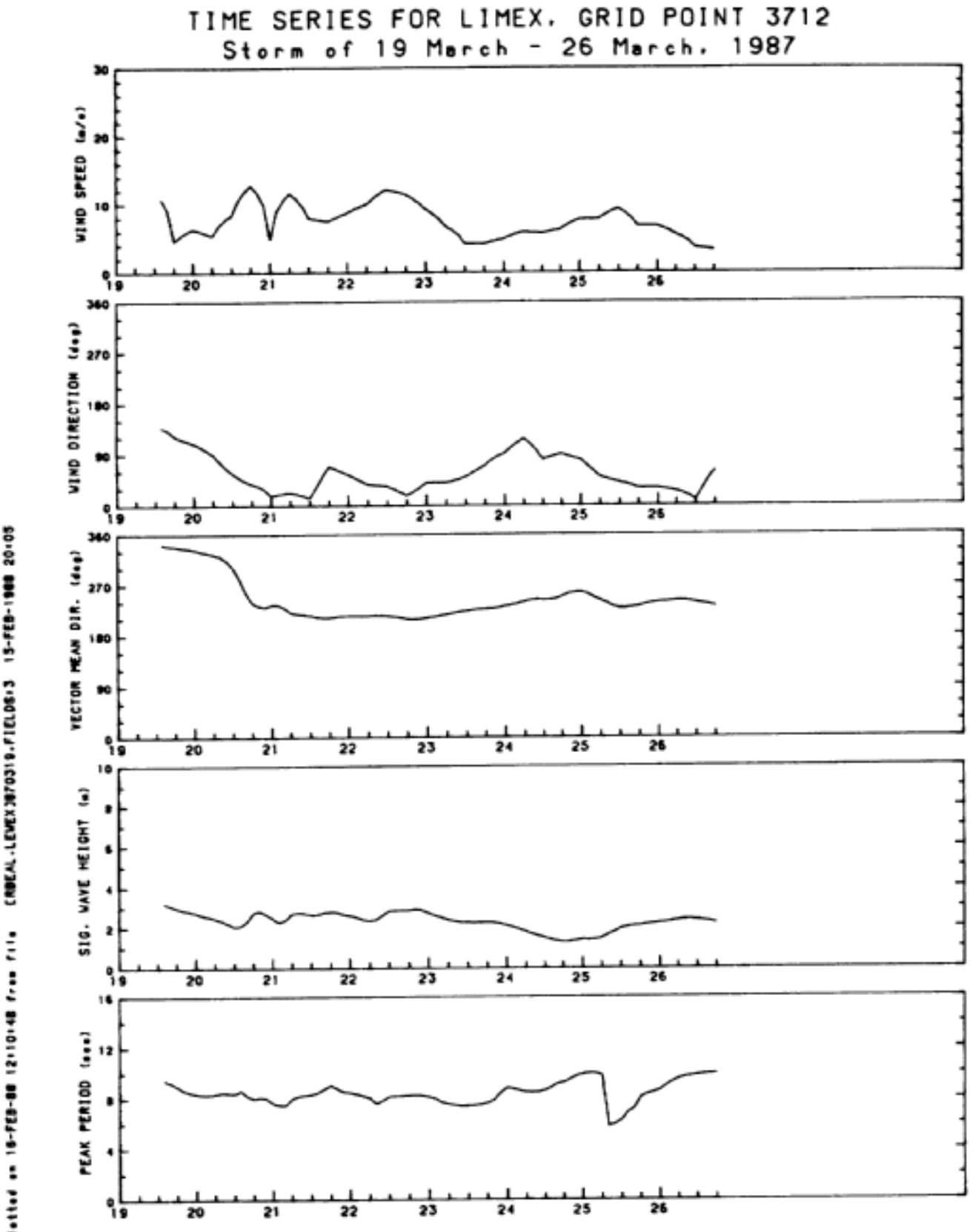
TIME SERIES FOR LIMEX. GRID POINT 3712
Storm of 19 March - 26 March. 1987
WIND SPEED (m/s)
WIND DIRECTION (deg)
VECTOR MEAN DIR. (deg)
SIG. WAVE HEIGHT (m)
PEAK PERIOD (sec)
19
20
21
22
23
24
25
26
Plotted on 16-FEB-88 12:10:48 from file [NBEAL.LEWEX]870319.FIELDS;3 15-FEB-1988 20:05

FIGURE 4.6

5.0 ICE PROPERTIES AND ICE MECHANICS

5.1 ICE COVER DESCRIPTION

The steady on shore winds pushed the pack ice west. All the strips and patches joined and exhausted most of the lead water within the ice field. The series of five AES Ice charts show the ice field compacting against the Newfoundland coast. The Ice Charts show the ice behaviour for the period from March 15th to March 28th. The easterly boundary of the ice field contracted 170 km West at 48 degrees North and 200 km west at 47 North. This means the winds compressed the ice field by 20,000 Km^2 over a one degree interval of latitude. This estimate assumes equal ice flows across the northern and southern boundaries. This compacting of the ice field to the West created the ice conditions experienced through the LIMEX ’87 research cruise.

The ice cover observed during the LIMEX Project displayed a series of interesting phenomena. There was a progression of ice conditions experienced. Each condition related to the events which proceeded it. The ship sailed south on March 15th and met heavy ice conditions which slowed its progress. There were periods when the ship was unable to maintain the desired heading through the ice field. During these periods, the Master stopped the ship and waited for ice conditions to ease and allow the ship to proceed. The ice cover which beset the ship was composed of small thick floes tightly compacted together. The ice cover was completely broken into small distinct floes. At this stage, there was little evidence of ground brash in the interstitial gaps between the packed floes. The on shore winds applied a tangential load to the ice cover forcing it into compression adjacent of the coast.

Vessel traffic to St. John’s harbour experienced difficulty transmitting through this ice field. The ice cover along the shore displayed short ridging networks. This feature is distinct from the classic shore ridge that parallels the coastlines in the Arctic. These short ridge features had randomly distribute directional axes. The ridges are a deformation features of the stress transfer in highly deformed sea ice cover.

An appropriate model for compacted pack ice cover is a weak plate on an elastic foundation. The wind and current apply drag forces tan–gent to the surface of the plate. When a solid boundary restrains an edge of the ice cover it experiences a static compressive stress field. The edge adjacent to the coast has the longest over ice wind exposure and experiences the highest stress. The strength of the ice cover is heterogeneous on a scale of tens of metres. The progressive failure of weak zones generated ridge networks within this ice plat. Therefore, the failure tends to strengthen portions of the plate. The strength of the cover increases until ice sheet grows strong enough to carry the applied load. The distance the ridge networks grow seaward depend on

the magnitude of the stress developed in the ice field. The driving force building the stress field is a combination of wind and current drag and the momentum of the ice cover. During the LIMEX ’87 period, the wind and current drag were acting at about 90 degrees to each other. The eastward drift had resulted in a fully compacted ice cover by March 21. The total ice cover displayed some degree of rigidity and the resulting cover was able to transfer a lateral stress.

The team deployed ice motion package to measure wave penetration in this condition on March 21, 1988. There was visual evidence of relative motion between individual floes. The ice cover 2 km from the ice edge consisted of solid floes packed edge to edge. The floes oriented themselves to minimize the water gaps between the floes. The compaction of flat rigid particles would develop by a network of contacts between particles. Intuitively, this would cause a cover with a relatively large area of interstitial gaps. The ice cover suggests the ice floes rotate, shear, and split and completely fill the surface. These are the same ice failure mechanisms that will operate to move floe ice pass fixed or moored offshore structures.

On a larger scale, the ice cover compacted to a solid band along the coast with a well defined ice edge. The formation of the distinct ice edge was an important step in the marked change of ice condition observed through the LIMEX ’87 experiment period. The ice cover had strength to resist wave bending moment initially. This condition was evident in the SAR imagery of March 21, when the ice floe boundaries were visible out to the ice edge.

Wave penetration into the ice field was not apparent in the first set of imagery. An ice plate composed of ice floes held together by surface forces has little strength to resist bending moments. The ocean swell striking to the ice edge induces a large bending moments in the ice cover. Hence, this particular ice plate fails in order to accommodate the bending and vertical shear loads. The ice cover suggests the failure is dominated by crushing and abrading the floe perimeters. These failure modes produce a large volume of ground brash. The failing ice consumes a portion of the incident wave energy. The ground ice flows into the interstitial gaps between the floes. When the surface stress is high the distinct floes push together until their edges contact. The ground ice is forced down by the floes pushing together and forms a layer of ground ice beneath the floe cover.

This ground brash ice serves to lubricate the contact between the floes. As the failure proceeds, the ice adjacent to the ice edge offers less resistance to bending moments. Then the incident ocean wave field is able to penetrate deeper into the ice cover. The travelling wave attenuates, as it meets still compacted ice floes. The

wave energy is absorbed by failing (grinding) solid ice at the floe to floe contacts. The incident swell component induces a cyclic load with a period of 1/f, For example, a 10 second swell would induce 8,640 stress reversals per day, Every point into the pack experiences this bending moment, until the wave height is attenuated and the bending stress does not exceed the failure threshold. The low tensile strength of the ice floes makes them weak in bending. Hence, ice floes will begin to split on wave crests as soon as the floe thickens enough to resist conforming to the shape of the wave. Failure occurs when the stress in the flexing floe exceeds the tensile strength of the ice. This mechanism probably dictates a maximum floes size for the marginal ice zone. Therefore, ice fields exposed to wave loading would have characteristic floe size distributions.

It should be possible to estimate a maximum floe size which is unlikely to split for a range of incident wave conditions. This will be an important consideration, when choosing a stable floe for making long term deployments of the ice motion package.

The research team conducted the next set of ice observations on March 23, 1987. The ship penetrated the ice edge to find a safe ice flow where the research team could work. The researchers established the ice station about 1 km from the ice edge. A large volume of ground ice brash filling the interstitial spacing between the individual floes, which ranged in size from 1 to 20 m. characterized the ice condition. The ice cover no longer behaved as a plate resisting the bending moments induced by the wave field. The longer wave lengths of incident ocean swell tends to penetrate deeper into the ice cover. The ground brash between the floes lubricated tilt of the individual floes. The viscous shear strength of the ground brash and the shape of the solid floes are sufficient to attenuate the higher frequencies.

The crew deployed motion package on a small floe and the field party boarded an adjacent larger floe. The field party were unable to move from floe to floe, because the gaps between the solid were too large to cross at this station. The grinding process appears to have decreased at the edge because floe to floe contacts had decreased. It is postulated that as the tangential force on the ice cover decreases the ground brash trapped beneath the ice floes floats up. The buoyant force of the ground ice acts to separate the individual floes and stop further grinding.

March 25, 1987 was the next observation period for ice motion measurement and ice observations. A large portion of ground brash characterized the ice condition adjacent to the ice edge. The ship penetrated the ice cover to conduct four ice motion stations. There were motion measurements collected at the ice edge and at 1 km, 2 km, and 4 km from the ice edge. The ice conditions along the measurement

line showed a progressive reduction in the ratio of exposed area of floe ice to ground brash ice. The measurement of this ratio is time consuming with existing methods. One method being considered is to measure the total area of ice floes in a specified area. Then compute the area and ratio of brash ice as a difference. One weakness of any difference method is its insensitivity to law concentrations of ground brash. Another is its sensitivity to the shape of the floes, and hence requires doing fine resolution digitization.

Image analysis techniques may provide more efficient ways to separate these two ice types within the ice cover. The development of such a method is beyond the scope of the present study. The floe ice and the ground brash are different forms of the same ice material, and often they are the same material, where the ground brash has refrozen into floes. Hence, it will probably not be practical to distinguish the two ice types by tonal methods like density slicing. In image analysis, tonal distinction are the simplest methods to carry out. Any future development should initially test density slicing . If density slicing does not given the required results, some methods to incorporate spatial correlations will be necessary the filter these two components.

The ice cover appeared uniform on a large scale by March 26, 1987. A matrix of ground brash ice separated the solid floes. The propagation of the swell in the ice cover was obvious visually. Interestingly, the swell appeared to have more than a single directional component.

A single component swell propagating in an ice field is a very distinct condition. The author observed such an ice condition during the ship–in–the–ice experiment in 1977. The visual effect is memorable. The wave crests appear as a series of parallel lines over the full ice cover. Extending away from the observer to the horizon. The ice cover did not display this type of pattern on March 26 1987.

The pattern was one of crests and troughs of limited extent, suggesting that the motion had two or more swell components. The measurements made by the motion package and wave field shown by the wave patterns of the SAR imagery confirm this observation.

The SAR imagery for the full ice cover provides an excellent means to investigate the ice condition and ice behaviour. The CCRS Convair 5800 collected imagery for three days during the LIMEX ’87 project. There was full coverage of the East coast of Newfoundland on March 21, 23, and 26, 1987. The imagery displayed the changing nature of the ice cover through the period.

The imagery on March 21 showed the ice cover compacted to solid ice cover by the tangential surface forces. A network of edge to edge floe contacts restrains the ice cover from any further drift compaction.

Initially, the ice cover effectively absorbed the incident wave energy. The coastal boundary to the west held the ice field along the Avalon coast. The ice adjacent to the ice edge did not exhibit and evidence of wave pattern.

The imagery collected two days later on March 23 was very interesting. It shows a distinct transition boundary within the ice cover. East of the transition, there was a wave pattern in the ice cover. West of the transition, the ice cover maintained enough floe to floe contact strength to absorb the incident wave energy. The transition zone had progressed about 5 km into the pack the ice edge, by the time of the second overflight.

The final set of SAR imagery collected on March 26. It showed the full ice cover penetrated by ocean swell. It is possible to trace wave crest through networks right to the coast all along the east coast of the Avalon. The ice cover did not show any evidence of any reflected wave patterns from the shore. One region north of the LIMEX ’87 interest area showed waves penetrating 40 km into the ice cover.

5.2 PHOTOGRAPHY OF ICE CONDITIONS ENCOUNTERED

There were four helicopter flights dedicated to aerial photography. The helicopter photography collected exposed ten bulk film cassettes. Each averaged between 70 to 100 frames per strip totaling about 850 frames over ice. The parameters for each flight line are summarized in Table 3.4 . Figure 5.1 shows these flight lines plotted on a map of the LIMEX ’87 study area. The selection of a 600 m flight elevation gave a reasonable width for the photographic lines. The could ceiling limited the camera height to 300 m on March 25.

All the photography shot from the helicopter was overexposed. It is difficult to measure exposure for snow or ice scenes, because these scenes contain typically high levels of reflected light. Normal light meter settings give the correct exposure for average photographic conditions, 18 percent grey is considered average reflectivity, and the usual calibration for a light meter. There are two methods to deal with this high ratio of reflected light in ground based photography. One is to use a light meter with a diffusing window to measure the incident light. The second is to read the light reflected from a standard 18 percent grey cord. The grey card reflectance is not a practical reading for helicopter aerial photography.

On the LIMEX ’87 cruise, the C–CORE photography employed the incident light method. The diffusing window was placed over the photo sensor. The light meter directed at the sky, pointed away from the sun’s glare. This method worked well for the ship board oblique photography. The light meter readings did not give the proper exposure for the helicopter aerial photography. The incident light readings, caused the

film to be about 4 stops overexposed, Fortunately several test film strips were exposure. Hence, it was possible to correct for some of the overexposure during the film processing. The incorrect reading resulted in a lower contrast negative for a low contrast ice scene.

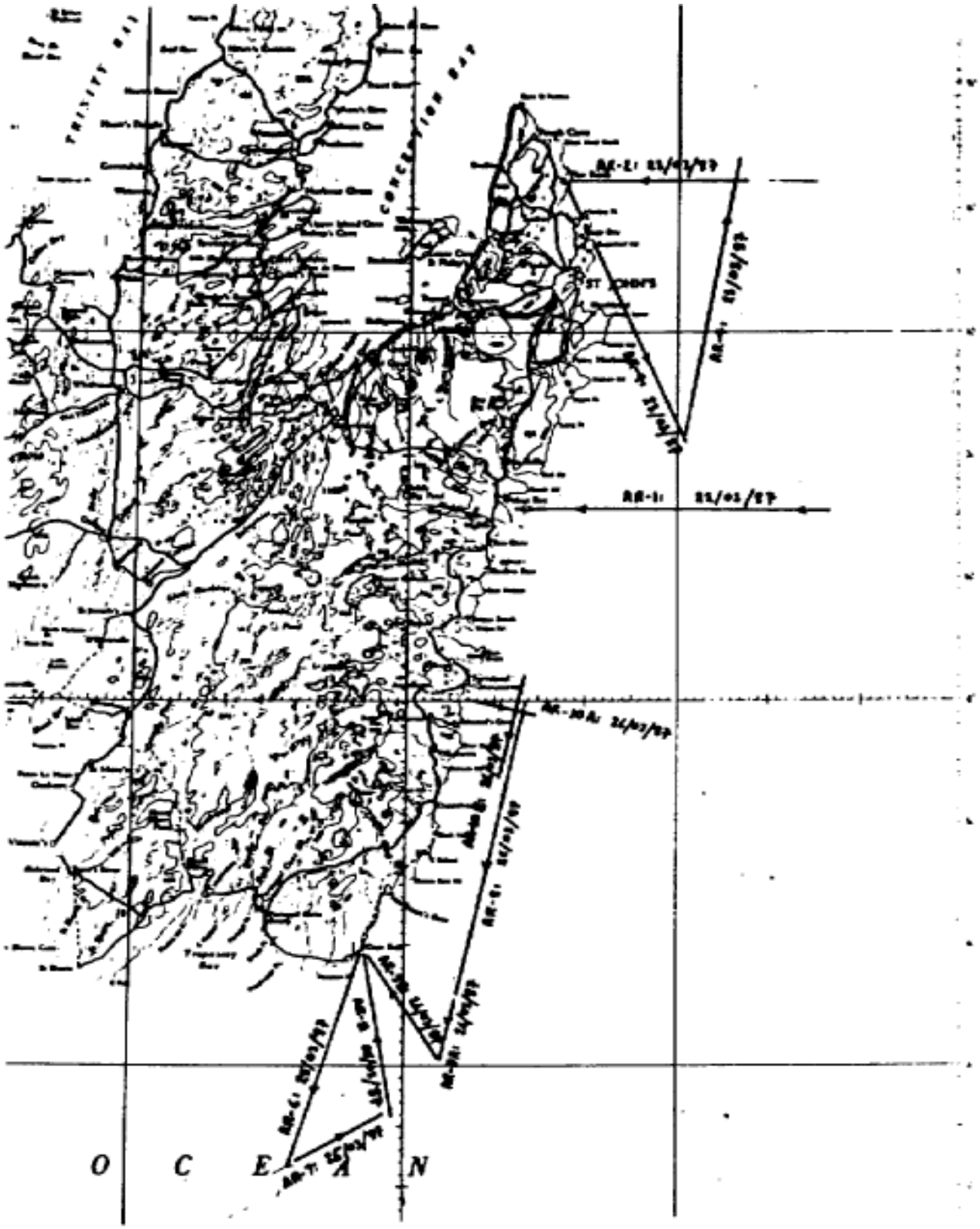

Figure 5.1 The helicopter aerial photograph lines plotted on a map of the LIMEX–87 experiment coverage area.

The helicopter camera platform compromises a number of factors which governs photographs quality. Many of the frames were blurred where adjacent frames are distinct. This condition suggests that aircraft motion caused the blurring. The helicopter speed was 45 m/s. The camera shutter speed setting was 1/500 seconds. The scene would move 93 m relative to the camera centre while the shutter was open, if the camera's optical axis was held steady. Many factors influence photographic resolution. These include the particular camera system, image exposure, and film processing. These were no measurements carried out to determine the resolving power of the system employed during LIMEX '87 system. The ability to distinguish distinct lines establishes a film's resolving power. Resolving power is expressed in lines per mm. A typical contrast ratio for a medium contrast panchromatic film would be about 50 lines/m. This is about 1.5 times the forward steady image motion. Therefore, the forward motion of the aircraft would not cause the blurring pictures. These motions are caused by environmental considerations like wind buffeting. The helicopter cannot correct for this type of motion. Therefore, the forward motion of the aircraft would not cause the blurring seen in the photographs. The rotations of the aircraft and the tilt of the optical axis are probably the cause of the blurred pictures. These motions are caused by environmental considerations like wind buffeting. The helicopter cannot correct for this type of motion. A gyroestabilized mount would improve the alignment of the optical axis but are not practical solution for a temporary camera mount. A higher shutter speed and better contrast control would improve picture quality.

It is not usually necessary to resolve fine detail for most application of ice imagery. The measure of floe sizes, floe shapes, deformation patterns, and ice concentrations only require coarse measurements. This work does not require high picture quality or accurate picture controls, Careful geographic control is pointless considering the ice field which is drifting through the region at about 0.5 m/s; the average ice drift measured during the LIMEX '87 cruise. Therefore a scene of ice drifts through the 400 metre wide swath of the photographic line in 12 minutes.

Photographic film imagery is time consuming to prepare and difficult to digitize. Digitizing with a 100 micro–metre pixel (picture element) spot will allow 10 lines/mm resolution on the resulting digital image, which is an order of magnitude less than a high contrast negative. A video camera system could replace a film camera for many photographic applications recording ice conditions. The recent models of video cameras capture each scene on a solid state CCD (charger coupler device). The commercial versions of this electronic device samples and stores the video signal on an array of 250,000 pixels. That compares to 9 lines/mm for a 55 mm, or 14 lines 3mm for a 35 mm film format.

Hence, the spatial resolution for a video scene now compares with the digitized resolution for a small format camera. The same types of cameras are practical to operate from a helicopter. High speed shutters are available for video cameras, 1/1,000 second. This feature will help decrease blurring of moving scenes. A camera height that would give a one kilometre swath scene would yield a 2 metre pixel resolution. Such imagery would be adequate for most ice applications and would be robust to blurring.

The video signal is straight forward to digitize, Commercial equipment is available to capture specific frames from pre–recorded tapes. The video camera offers intensive coverage. Moving pictures require more than 30 frames per second to simulate continuous motion. A second video camera with a different focal length lens could collect a higher resolution image for a portion of the scene. A single mounting unit could support both cameras.

A video system would fill C–CORE's requirements for recording ice conditions. If required, a film camera could be attached to the same camera mount as the video camera. A video system would be very simple to operate. A single tape will record continually for 160 minutes. The camera system meters the lighting of the scene automatically. Video recording permits a good adjustment of contrast control during playback.

Still video cameras are about to come on the market. These cameras will collect a video record for specific scenes. The camera will have a disk drive and will store the CCD pixel set for a particular scene to magnetic disks. Each disk will store about fifty frames. The playback unit will randomly access any one scene for playback. it will be simple to prepare a frame for computer image analysis. The photographic equipment suppliers have agreed on a standard picture format and standard interface. Although the concept of still video is interesting, the proven technology of the motion video camera will be the better choice for the LIMEX 189 programme.

5.3 FLOE SIZE DISTRIBUTION ANALYSIS

The floe size distributions for the ice edge zone were estimated from the helicopter aerial photographs. The helicopter was equipped with a standard altimeter. The picture dimension error resulting from camera height error takes the form of $(h - h_{avg})/h$ where h is the camera height and is not important for the accuracy required to measure ice cover features. Figure 5.1 shows the ten helicopter photographic flight lines plotted on a map of the Eastern Avalon, Floe size distributions were measured for aerial photograph lines AR #3, AR #5, and AR #10.

The floes sizes were extracted from the aerial photographs using a table digitizer. The floe sampling was randomized by describing lines

on the photographs and measuring every floe occurring along each line. A program was written to scale the photographs and compute floe sizes from the data files of digitizer coordinates. Then size interval frequency counts were enumerated for the range of floe sizes observed on each photograph. Floe size histograms were plotted based on these counts.

Figures 5.2 , 5.3 , and 5.4 are the histograms of the floe size distributions from photograph line AR #3, March 23rd, 1987. The three samples are taken from the seaward edge (Figure 5.2), the mid–point and the shore end (Figure 5.4). The distribution shown in Figure 5.2 indicates an ice cover of small floes and ice pancakes with a maximum floe size of 11 metres. Figures 5.3 and 5.4 suggest the form of the distribution changes and the mean floe size increases across the ice field to the coast.

Figures 5.5 , 5.6 , and 5.7 were measured for photograph line AR #5, March 25th, 1987. The set of floe size distributions associated with the main ice motion study, Four ice motion stations were established and motion records collected. The first station at the ice edge and the next three spaced into the ice cover. These histogram plots illustrate the ice cover floe sizes for the first 5 km, from the ice edge into the ice field. This set of histograms indicate a uniform ice floe size coverage over the experimental area.

The photograph flight line AR #10, March 26th, 1987 was collected in two parts across the field from the coast to the ice edge, denoted as (A) and parallel to the coast and over the ship, denoted as (B), Figures 5.8 , 5.9 , and 5.10 are the floe size distributions across the pack ice for AR #10 (A). Again, the three samples are taken from the ice edge (Figure 5.8), the mid–point and the landward edge (Figure 5.10). The shape of the distribution changes across the ice field and is similar to the change in the distributions observed for photograph line AR #3, discussed above, Figure 5.11 , 5.12 , and 5.13 are the histograms parallel to the ice edge for AR –10 (B). The mean floe size remains constant parallel to the ice edge. The change of the shape of the distribution in Figure 5.13 appears to be an artifact of the auto–ranging feature of the computer program producing the histogram plots. It was caused by the 28 metre maximum floe size which was encountered in the floe size enumeration.

The floe size histograms show the ice cover to be highly broken into small pancake floes. The means floe size increased as a function of distance from the ice edge. These results from the floe size distribution analysis provided additional evidence that the incident

ocean waves are a major factor in breaking the ice cover of the marginal ice zone into small floes.

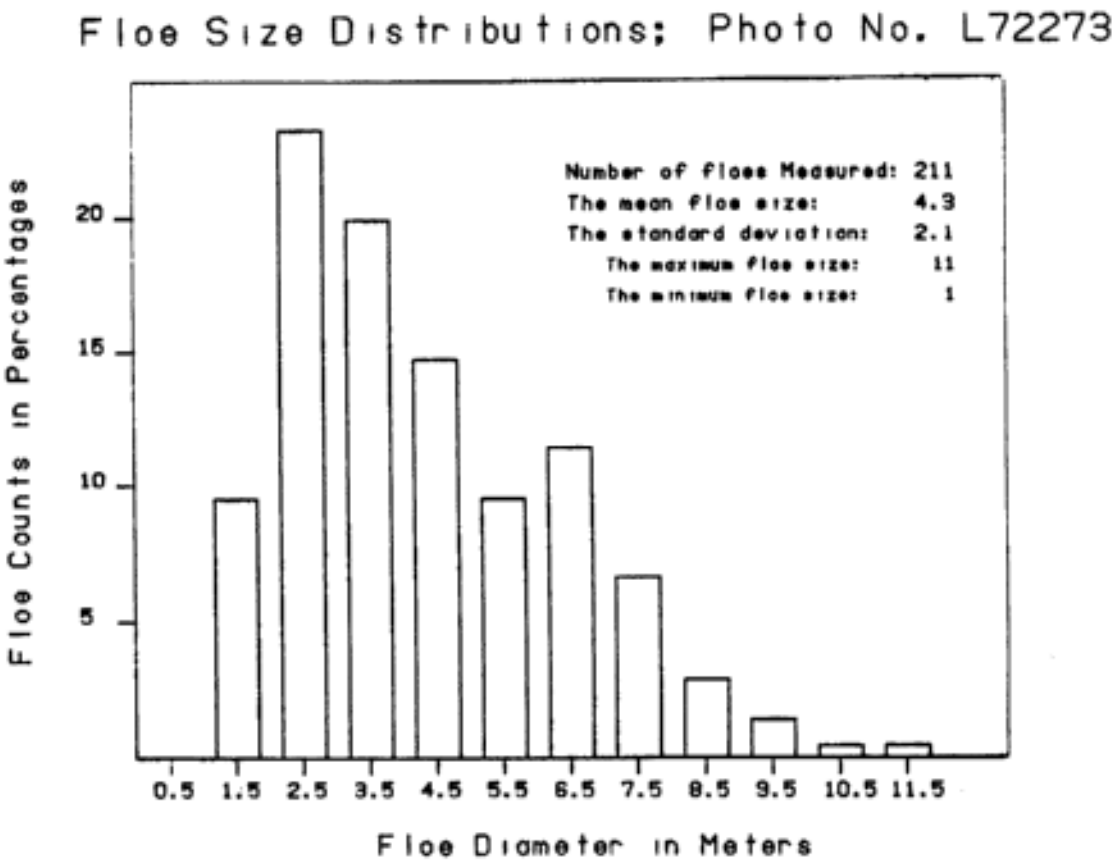

Figure 5.2 Histogram of floe size counts for AR #3, at ice edge

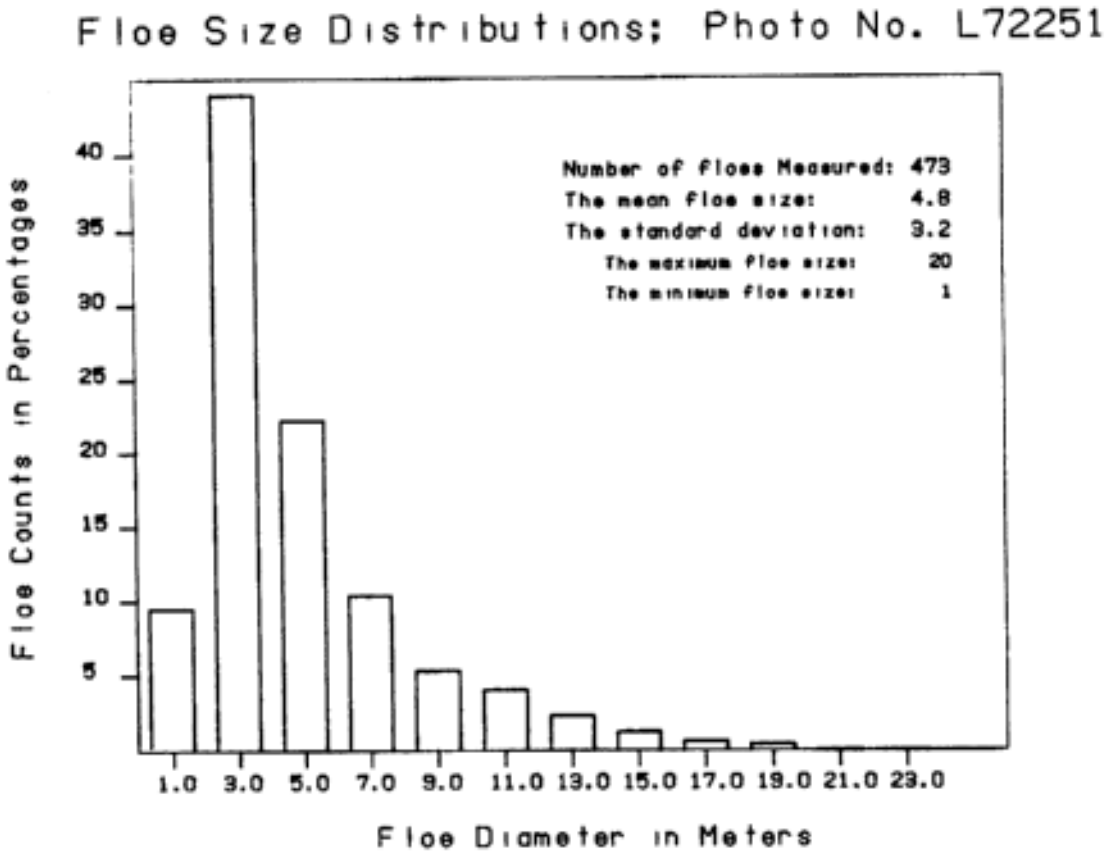

Figure 5.3 Histogram of floe size counts for AR #3, at mid-point.

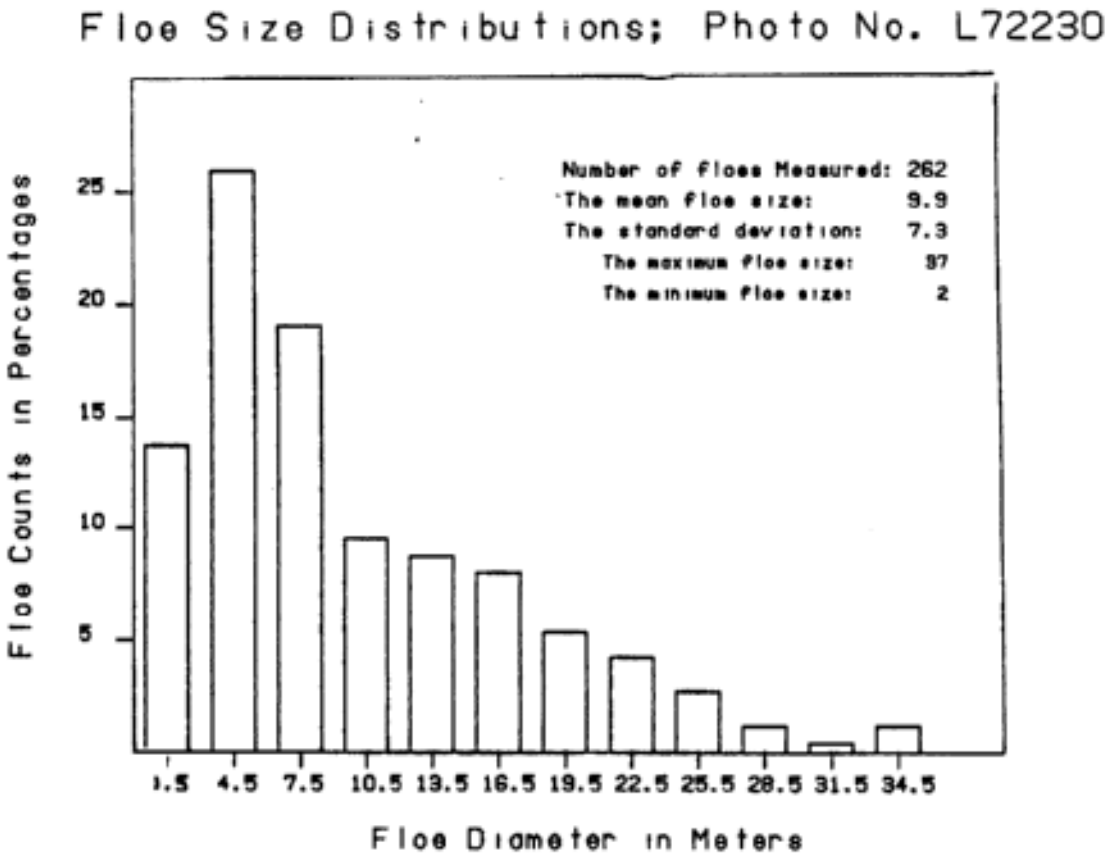

Figure 5.4 Histogram of floe size counts for AR #3, at coast edge.

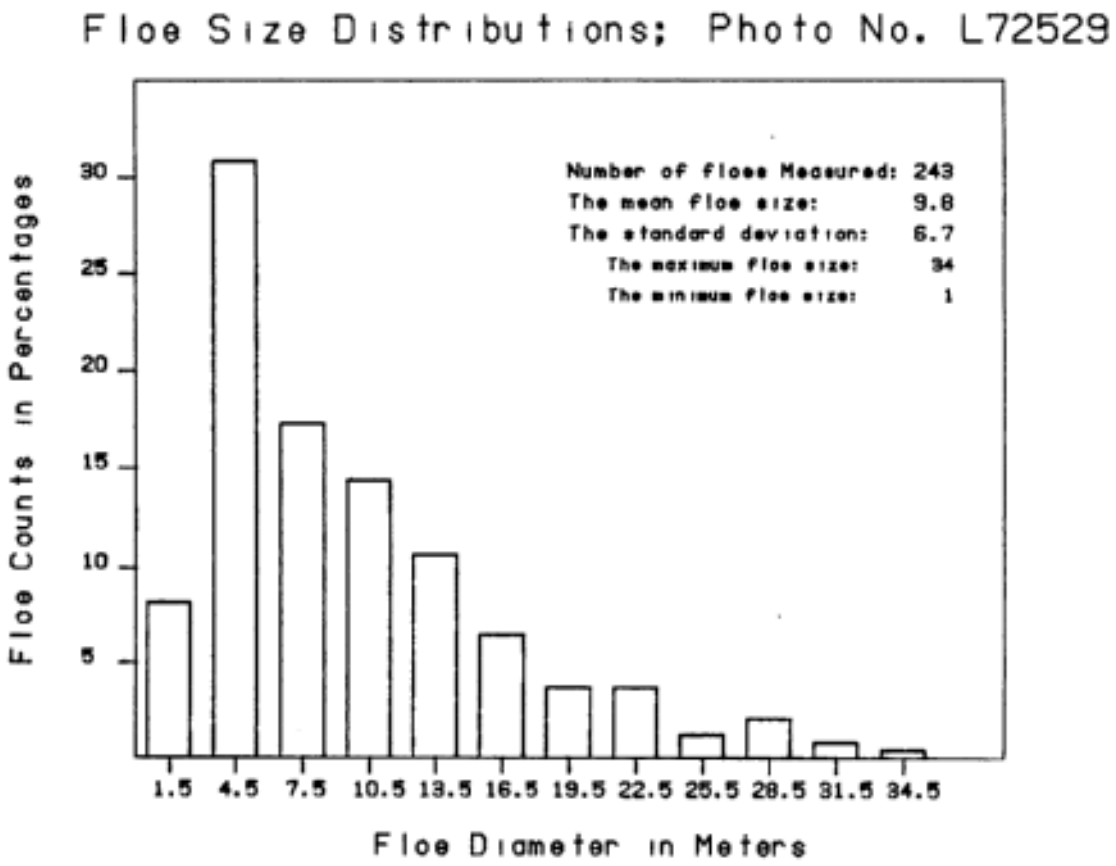

Figure 5.5 Histogram of floe size counts for AR #5, at ice edge.

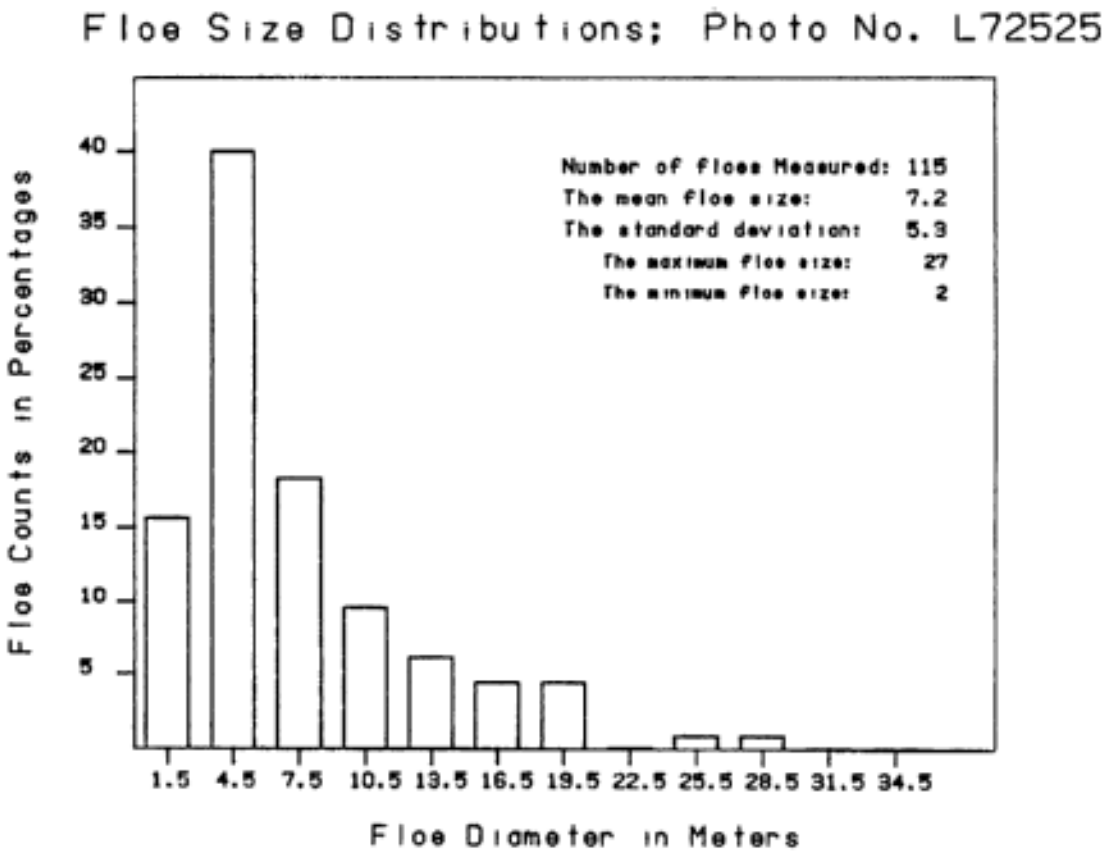

Figure5.6 Histogram of floe size counts for AR #5, at 2 km from edge.

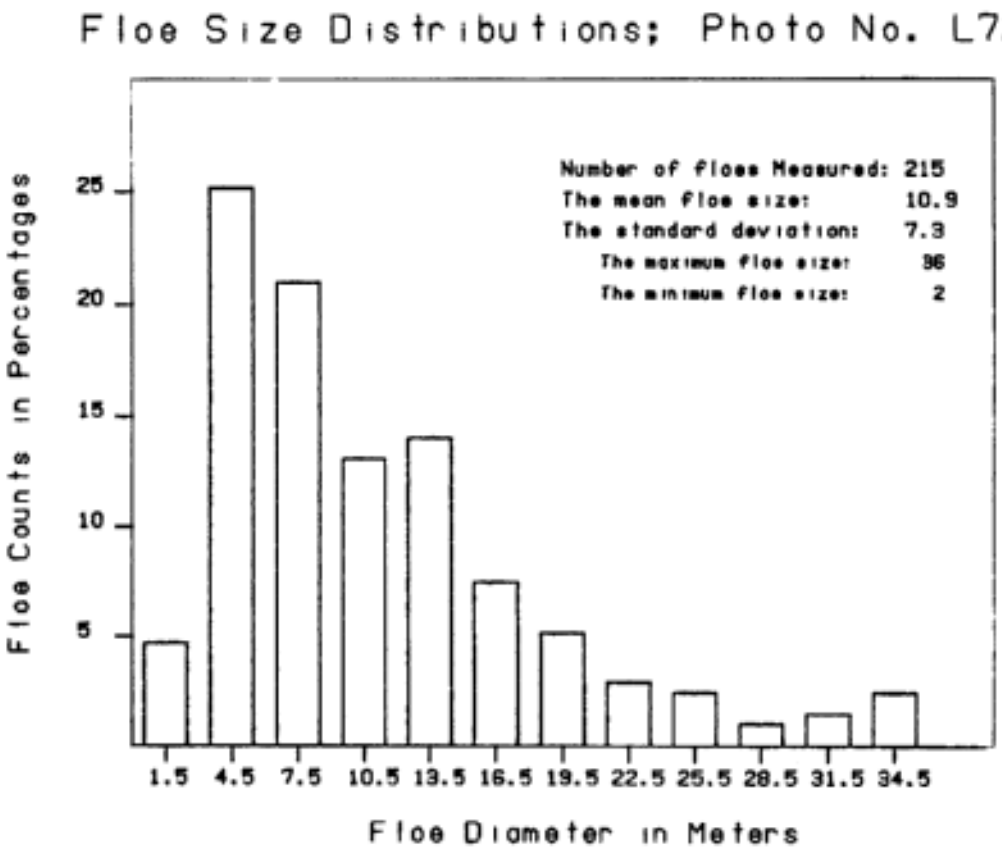

Figure 5.7 Histogram of floe size counts for AR #5, at 5 km from edge.

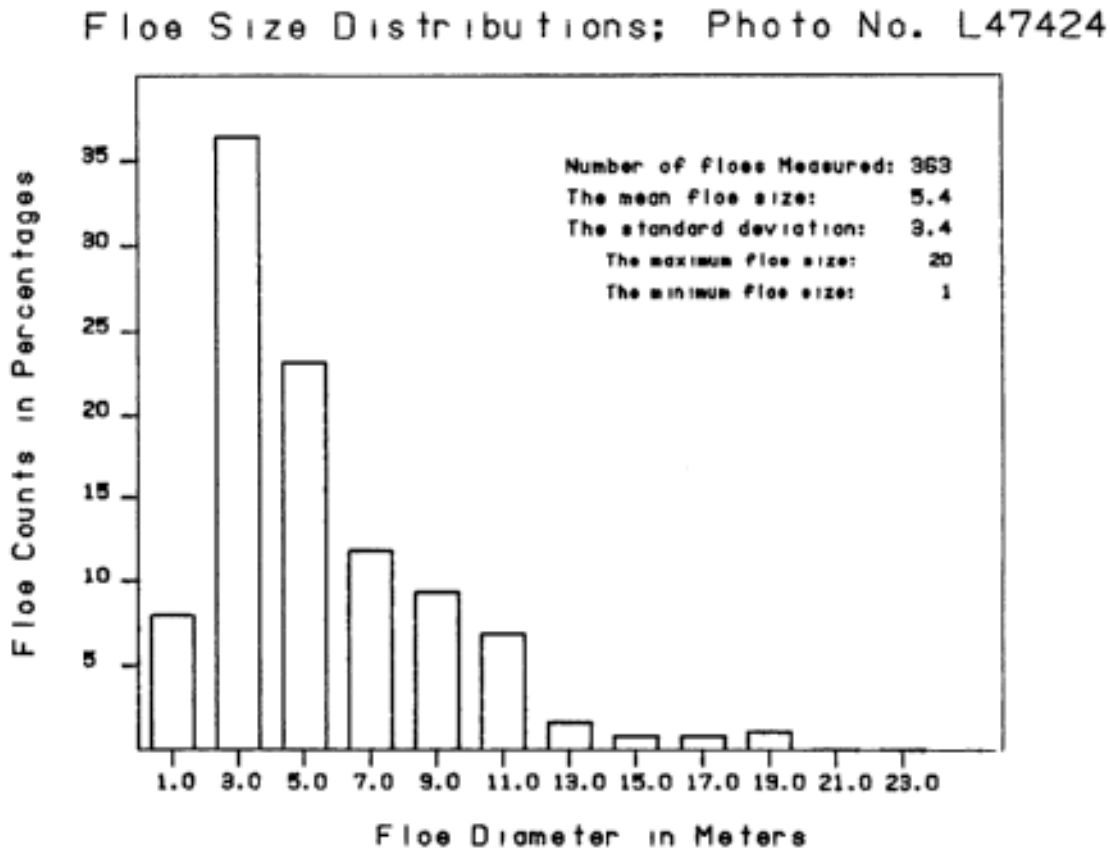

Figure 5.8 Histogram of floe size counts for AR #10(A), at ice edge

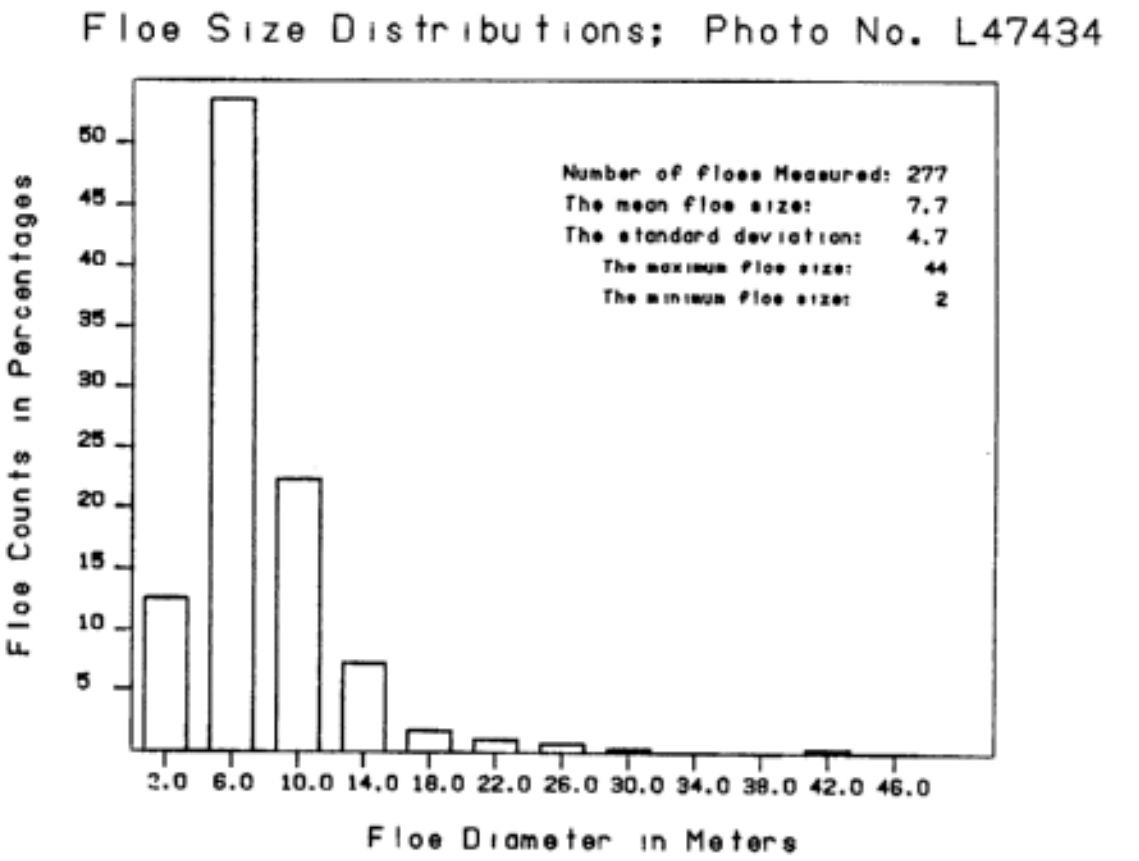

Figure 5.9 Histogram of floe size counts for AR #10(A), at ice edge.

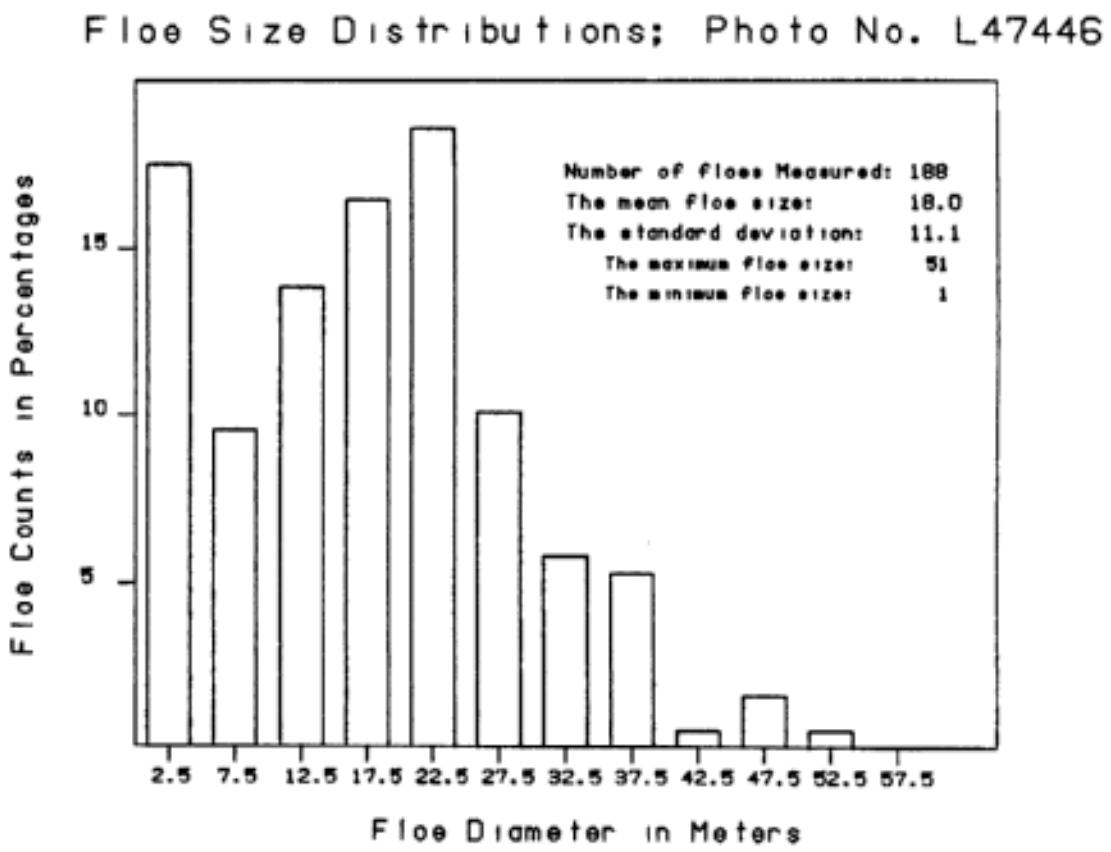

Figure 5.10 Histogram of floe size counts for AR #10(A), at coast edge.

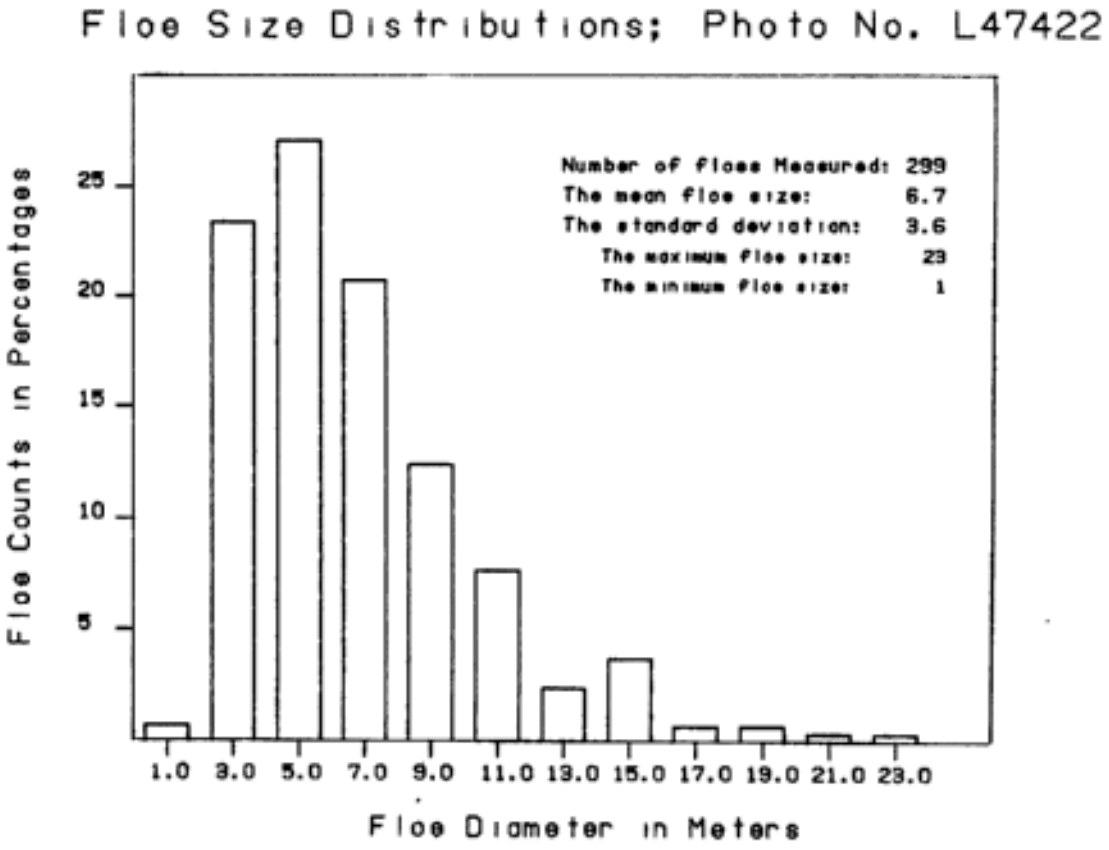

Figure 5.11 Histogram of floe size counts for AR #10(B), at north end.

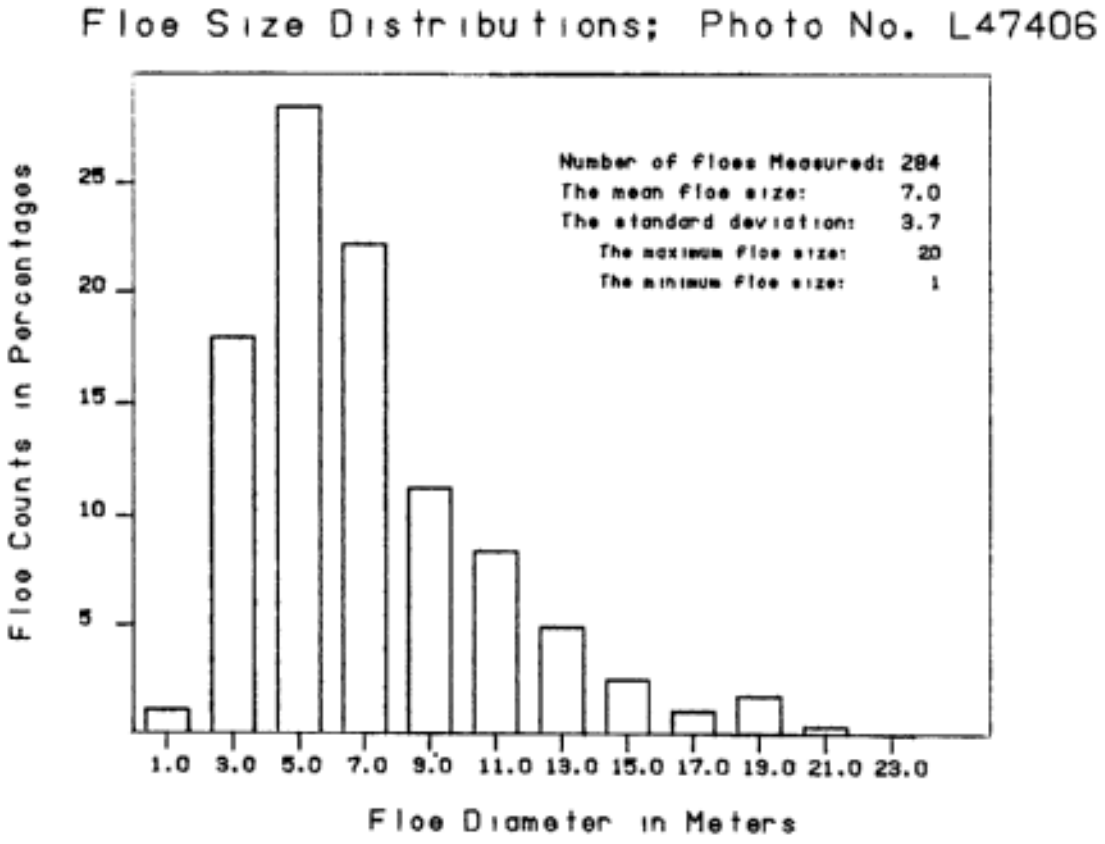

Figure 5.12 Histogram of floe size counts for AR #10(B), at research ship.

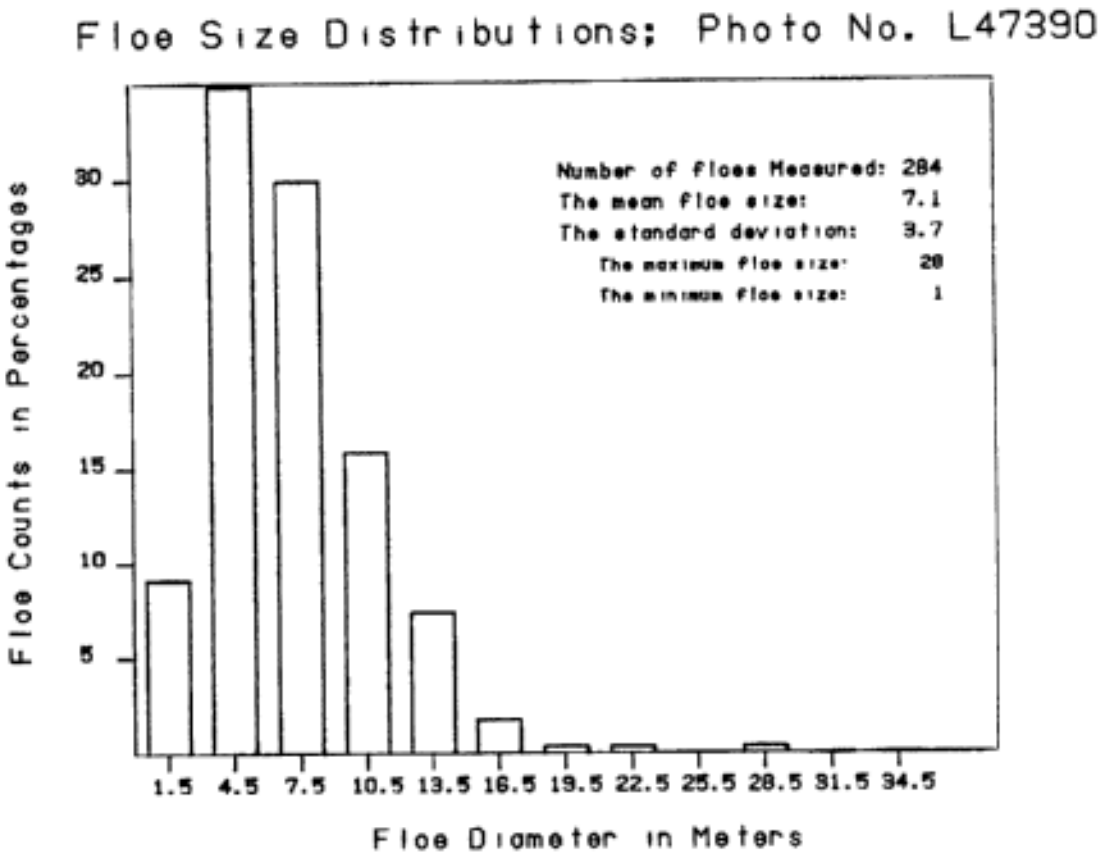

Figure 5.13 Histogram of floe size counts for AR #10(B), at south end.

6.0 WAVE–ICE INTERACTION ANALYSIS

6.1 ICE MOTION DATA ANALYSIS

6.1.1 Ice Package Instrumentation

During LIMEX ’87, two ice motion packages were deployed on ice floes in the marginal ice zone, as described in Section 3.0 . Both instruments were six degrees–of–freedom motion sensors. The two packages (designated B and C) differed primarily in their measurement of tilt components and the manner in which the data were logged. The sensor measurement convention is shown in Figure 6.1 for the case of small package tilts.

Both packages contained 3 Sundstrand QA800 Servo–Accelerometers to measure linear acceleration along orthogonal axes. The two horizontal accelerometers (x, y axes) were scaled to ±1g, while the vertical one (z axis) was scaled to 0–2g. These sensors have a maximum linearity error of ±60μg, a resolution of 5μg and a frequency response error of ±0.1% over the range 0 – 10Hz.

Both packages also contained an Endeco 86900128 Solid State Compass to measure magnetic bearing (0 – 360°). The accuracy of the compass is ±1°, with a resolution of 0.5°.

To measure pitch and roll (angular rotation about x and y axes, respectively), package B contained a Humprey VG24–0825–1 Vertical Gyro. This gyro has ranges of ±60° for pitch and 360° for roll. The vertical accuracy is ±O.5° with a maximum linearity error of ±2%.

The pitch and roll measurements in package C are made using two Penny & Giles 3910/60 Tilt Sensors. These have a range of ±30°, with a maximum linearity error of ±0.15°.

Each 6–sensor cluster was flexibly mounted to an aluminum plate installed within the respective package enclosures, Natural frequencies of the mounts in various directions were 7 – 15 Hz, giving a degree of vibration isolation without compromising frequency response.

The 6 sensors signals from each cluster were individually low pass filtered to –40 dB at 6 Hz, with negligible attenuation and phase shift as 0.6Hz. In package B. the 6 signals together with ±5v reference voltages were multiplexed at 12 Hz and recorded on a single channel of a Racal Store 4 Instrumentation Recorder. This arrangement provided approx, 1.5 hours of recording capacity on 550m tape, with a signal–to–noise ratio of 40 dB.

In package C, the 6 filtered sensor signals together with the ±5v reference voltages and ground were digitized at 12.5 Hz to yield 12

bit plus 1 sign bit digital equivalent data. The digitized serial data were buffered, then periodically written to a Rosscomp D161 Cartridge Tape Drive. This data logging configuration has sufficient storage capacity for approximately 8 days continuous use, although operational considerations during LIMEX ’87 restricted deployments to a few hours maximum.

Unfortunately, the data logger design was still under development in March 1987 and problems were encountered with the tape write/read capability, resulting in some data loss.

Both types of sensor configurations (gyro and tiltmeter based) have been calibrated under static and dynamic test conditions. When fully processed through to physical units in a fixed horizontal reference frame, computed accelerations, velocities and displacements were found to agree with the imposed values to within approximately ±5% over the frequency range of interest, 0.02 – 0.5 Hz. In absolute terms, the computed vertical displacements obtained from the LIMEX ’87 deployments should be accurate to within ±3 cm. The pitch and roll measurements obtained from the gyro in package B should be accurate to within ±0.1°, while those obtained from the tiltmeters in package C should be accurate to within ±1°.

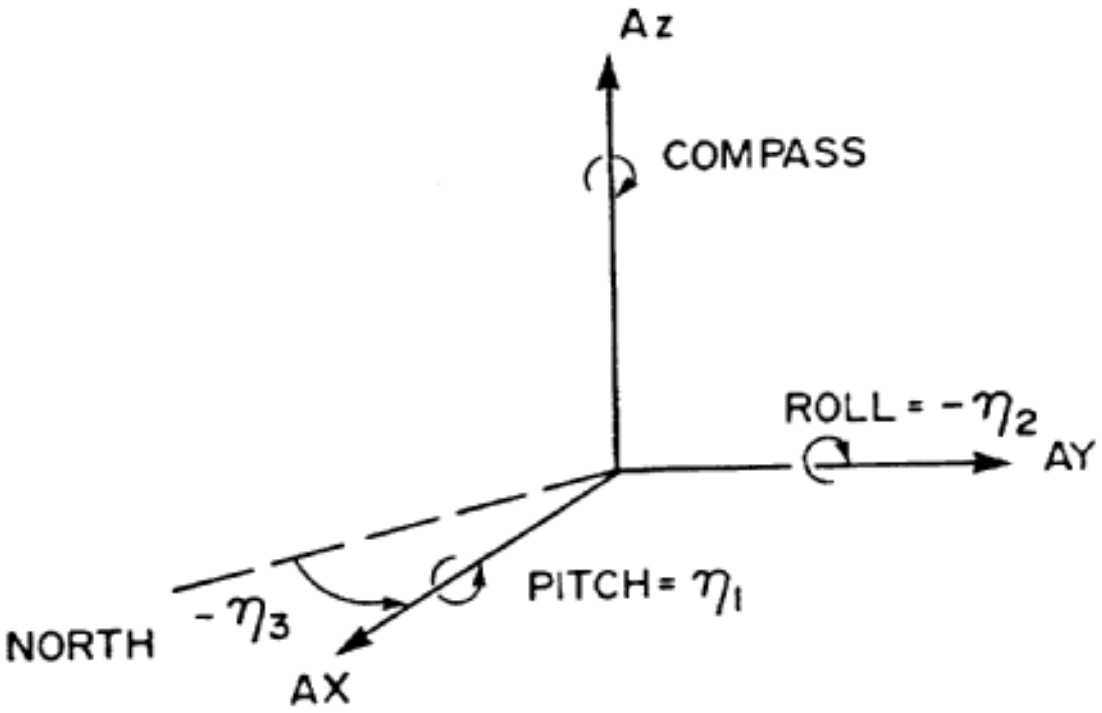

Sensor measurement convention for small package tilts. AX, AY, AZ are the three orthogonal linear accelerations; PITCH, ROLL, COMPASS, are the measured rotations and η_1, η_2, η_3 are the corresponding Euler angles defining the package orientation with respect to a fixed horizontal reference frame of North, West and Vertical.

Figure 6.1

6.1.2 C–CORE Ice Package Measurements

As mentioned in Section 3.2 , there were 13 deployments and recoveries of the instrument packages during LIMEX ’87. The first three B package deployments (19–1B, 20–1B, 21–1B) yielded no data due to battery failure. Also, two deployments of package C yielded no data (21–2C, 23–1C), as a result of tape write/read failures. The remaining 8 deployments yielded a total of approximately 8 hours of motion data on 3 different days (March 22, 25, 26).

The processing steps may be separated into 3 overall functions. The first, primary processing, involved reading the source data tapes (multiplexed analogue tape for package B. digital cartridge tape for package C), and converting the voltage signals to the corresponding sensor physical units as measured in the motion package reference frame XYZ.

The second main function, secondary processing, transforms the accelerometer readings from the package frame to a space fixed horizontal reference frame with axes pointing in the North, West and Vertical directions. The rotational measurements are similarly converted to a set of Euler angles which uniquely define the orientation of the package with respect to the fixed reference frame. The fixed frame accelerations are then integrated to velocity and displacement, with filtering performed between each integration to control the low frequency noise components.

As a form of quality control of the data, time series plots of the six degrees of freedom were obtained as a function of time. An example is shown in Figure 6.2 .

The third overall function is the production of the frequency spectra used in the computation of directional wave spectra.

Table 6.1 contains a list of frequency files, obtained during the experiment. As outlined by Longuet, Higgins et al. (2963) the co–spectra C_{ij} and quadrature–spectra Q_{ij}, obtained from correlations involving $z(t)$, $\partial z/\partial x$, $\partial z/\partial y$ (i,j = 1,2,3 respectively), may be used to obtain an approximate representation of the directional wave energy spectrum $E(f,\phi)$ based on angle ϕ.

Each record was divided into 20 minute blocks, Each block of data constitutes a separate data file. The 6 spectra C11, C22, C23, C33, Q12, and Q13, are used to compute the first Fourier Coefficients in the Fourier series expansion of $E(f,\phi)$. These spectra were generated for all data sets recovered.

The correspondent ODGP hindcast spectra at the nearest grid points to the motion package locations were compared to those obtained from the motion packages. Figure 6.3 shows the ODGP grid points near LIMEX area (note: ice edge shown is that used in the model).

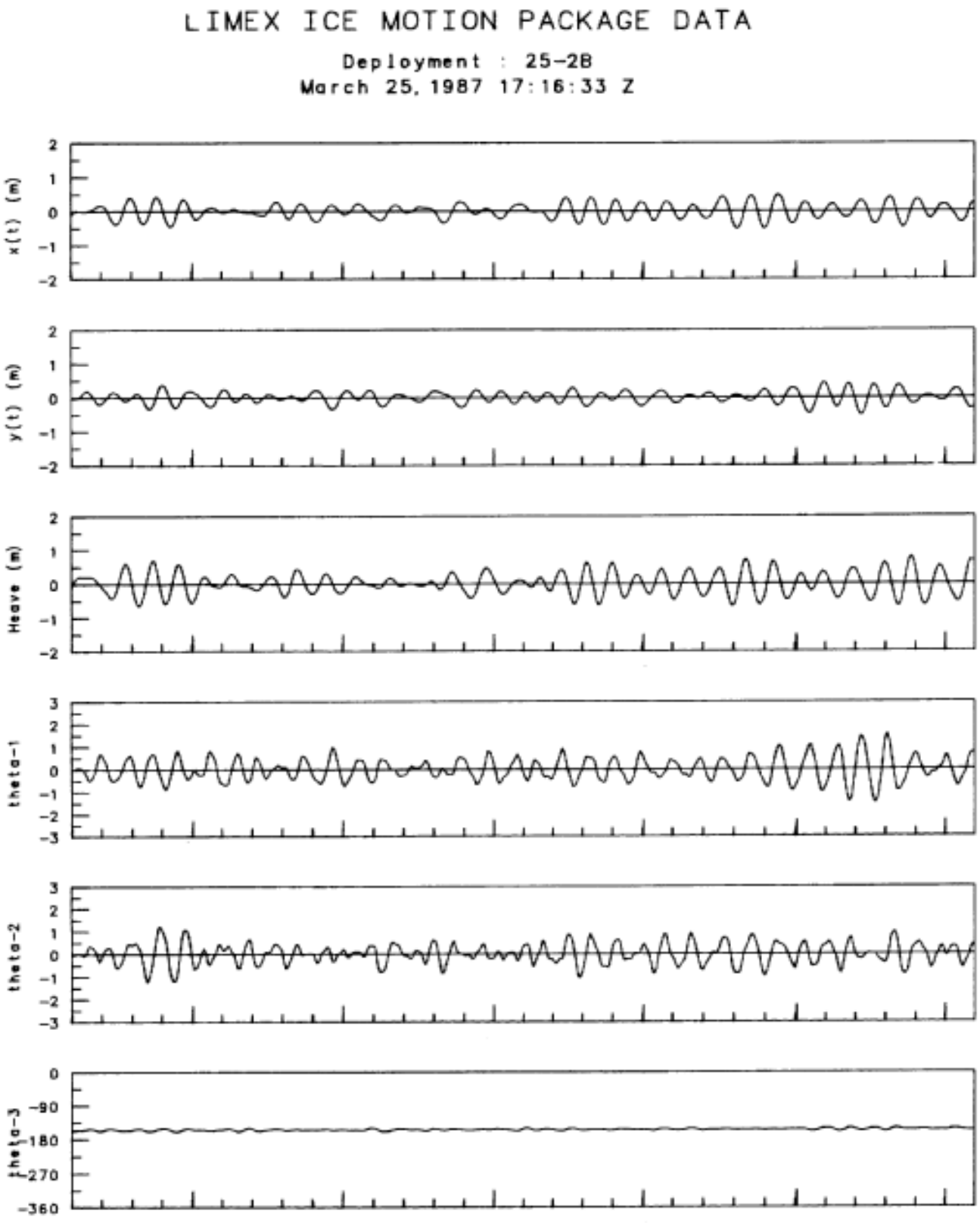

Figure 6.2 - First five minutes of deployment 25-2B.

6.2 ICE MOTION PACKAGE ENERGY SPECTRA

The standard measurement of wave elevation and slopes normally utilizes a wave buoy whose motion response characteristics are known over the range of ocean wave frequencies. In LIMEX ’87, motion measurements were made on ice floes within the pack ice. The motion characteristics of the instrumented ice floes are not known, and hence, in general, it is not possible to state how the measured heave, pitch and roll relate to the corresponding wave elevation and slopes, Furthermore, the dispersion relationship linking wave frequency to wavelength is modified by the presence of pack ice.

It is likely that for the predominantly long wavelength waves which penetrate the pack ice, moderately sized (< 10m dia,) ice floes follow the wave surface reasonably closely. Thus, the measured floe motions may be cautiously treated as being equivalent to the desired wave measurements .

Also, for uniform ice, the wave dispersion relationship is known. The derivation of this relationship required knowledge of the boundary condition at the ice/water interface, a condition which may readily be specified assuming a uniform ice cover of known material properties. However, in partial ice cover, this boundary condition varies locally from open water to ice covered conditions. It is not known how this affects the wave dispersion relationship or indeed if this relationship can even be determined except in some area–averaged sense.

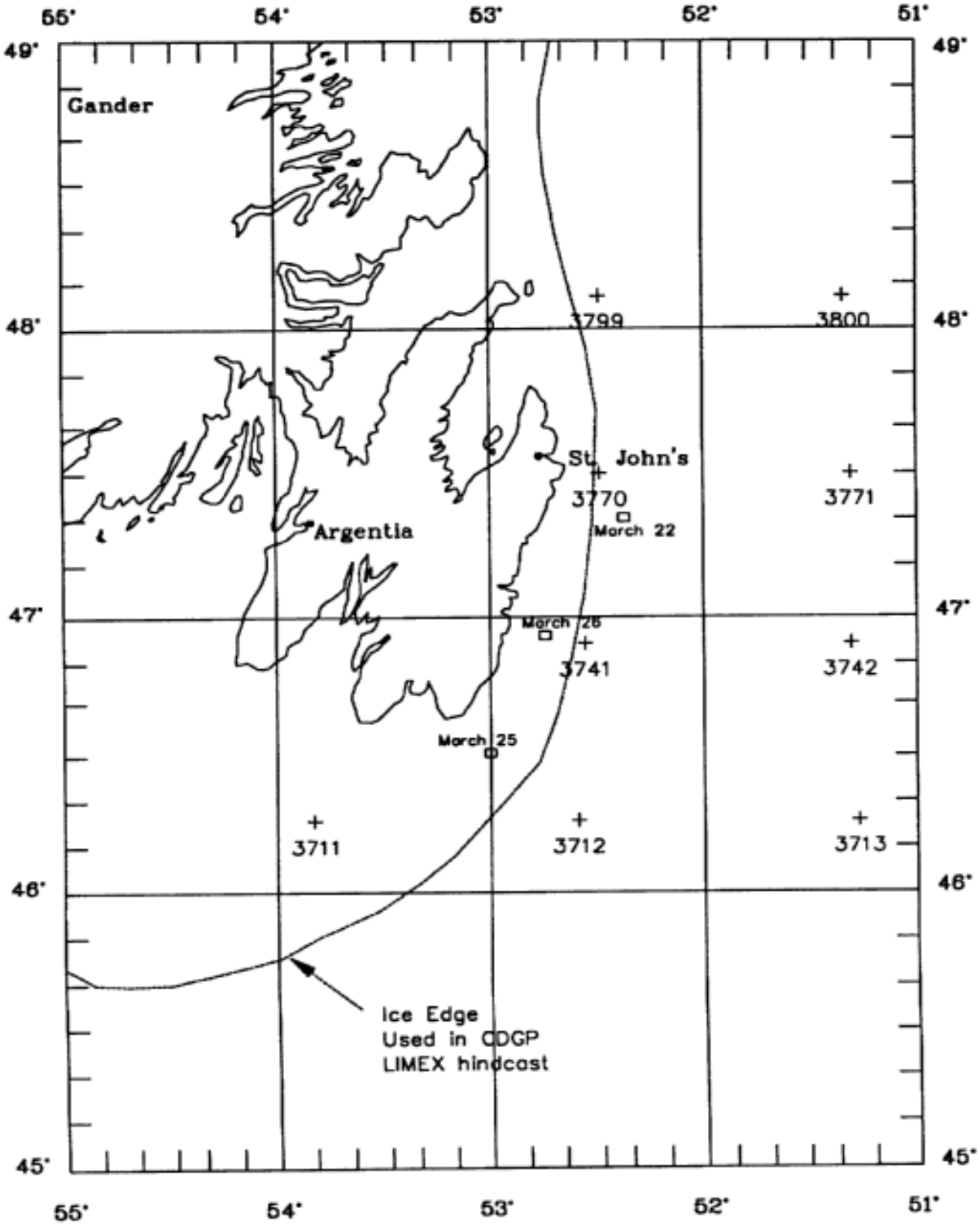
55°
54°
53°
52°
51°
49°
48°
47°
46°
45°
Gander
Argentia
St. John's
3799
3800
3770
3771
March 22
March 26
3741
3742
March 25
3711
3712
3713
Ice Edge
Used in CDGP
LIMEX hindcast

Figure 6.3

TABLE 6.1

List of frequency blocks for LIMEX deployments

TIME indicates the start of the time series. The length of the time series for a block is 1200 [s] or a portion greater than 300 [s], for the last block of a file. The resolution of all blocks is 0.005 Hz.

DEPLOY	BLOCK	LEN [s]	DATE	TIME (NST)	LAT	LONG
22-1C	1	1200	22-03-87	10:08:35	47.3492N	52.1609W
	2	1200		10:28:35	(average value)	
25-1C (1)	1	1200	25-03-87	11:54:42	46.4783N	52.9226W
	2	1200		12:14:42		
	3	1200		12:34:42	(in 5 files)	
	4	1119		12:54:42		
25-1C (2)	5	1200		13:23:12		
	6	1200		13:43:12		
	7	1200		14:03:12		
	8	1200		14:23:12		
	9	519		14:43:12		
25-1C (3)	10	1200		14:56:32		
	11	1200		15:16:32		
25-1C (4)	12	1200		15:42:40		
	13	1200		16:02:40		
	14	1200		16:22:40		
	15	1200		16:42:40		
	16	519		17:02:40		
25-1C (5)	17	1200		17:16:00		
	18	692		17:36:00		
25-2B	1	1200		13:46:29	46.4594N	52.9226W
	2	523		14:06:29		
25-3B	1	1200		15:35:15	46.4416N	52.9498W
	2	578		15:55:15		
25-4B	1	1200		16:41:39	46.4407N	52.9696W
	2	319		17:01:39		
26-1B	1	962	26-03-87	09:16:37	46.9680N	52.6830W
26-2C	1	1200		10:29:32	46.9730N	52.6830W
	2	591		10:49:32		
26-3B	1	1200		12:53:28	46.9730N	52.7930W
	2	1000		13:13:28		

6.2.1 Nondirectional Energy Spectra

Since the heave measurements, to a certain extent, are least affected by the shape and properties of the ice floe, nondirectional wave spectra obtained from ice floe motions are probably valid without correction. These spectra will yield information on the attenuation of wave energy by the ice cover.

The nondirectional or 1–dimensional energy spectra for the ice package deployments are shown in Figures 6.4 to 6.8 . The 1–dimensional spectra illustrates the energy density (given by co–spectra C11) as a function of frequency over a twenty minute recording period. During the LIMEX duration, the ODGP model was run in hindcast mode. The predicted nondirectional spectra at ODGP grid points in the open water near the ice package deployments (Figure 6.3) have been compared with the ice package spectra (also refer to Figures 3.2 and 4.3 , and Section 3.2 for description of ice conditions at deployment sites).

The deployment 22–1C yielded two nondirectional spectra plots. At the same time, a nondirectional waverider buoy (see Table 3.3) was deployed near the ice floe by L. Thomas of DTNSRD. The resulting waverider spectrum (taken from Thomas 1987) has been included with the ice package and ODGP spectra at grid point 3770 in Figure 6.4 . The spectra plots indicate that the ice motion did not vary much over the deployment. A comparison of the ice motion spectra with the waverider spectrum indicates that the nondirectional energy spectra of the ice package can be used to approximate the wave energy in an ice field. It should be noted that the motion package was deployed on a small ice floe in a narrow strip of sea ice seaward from the main ice pack as described previously in Section 3.2 . In this case the floe and the motion package acted as a waverider buoy.

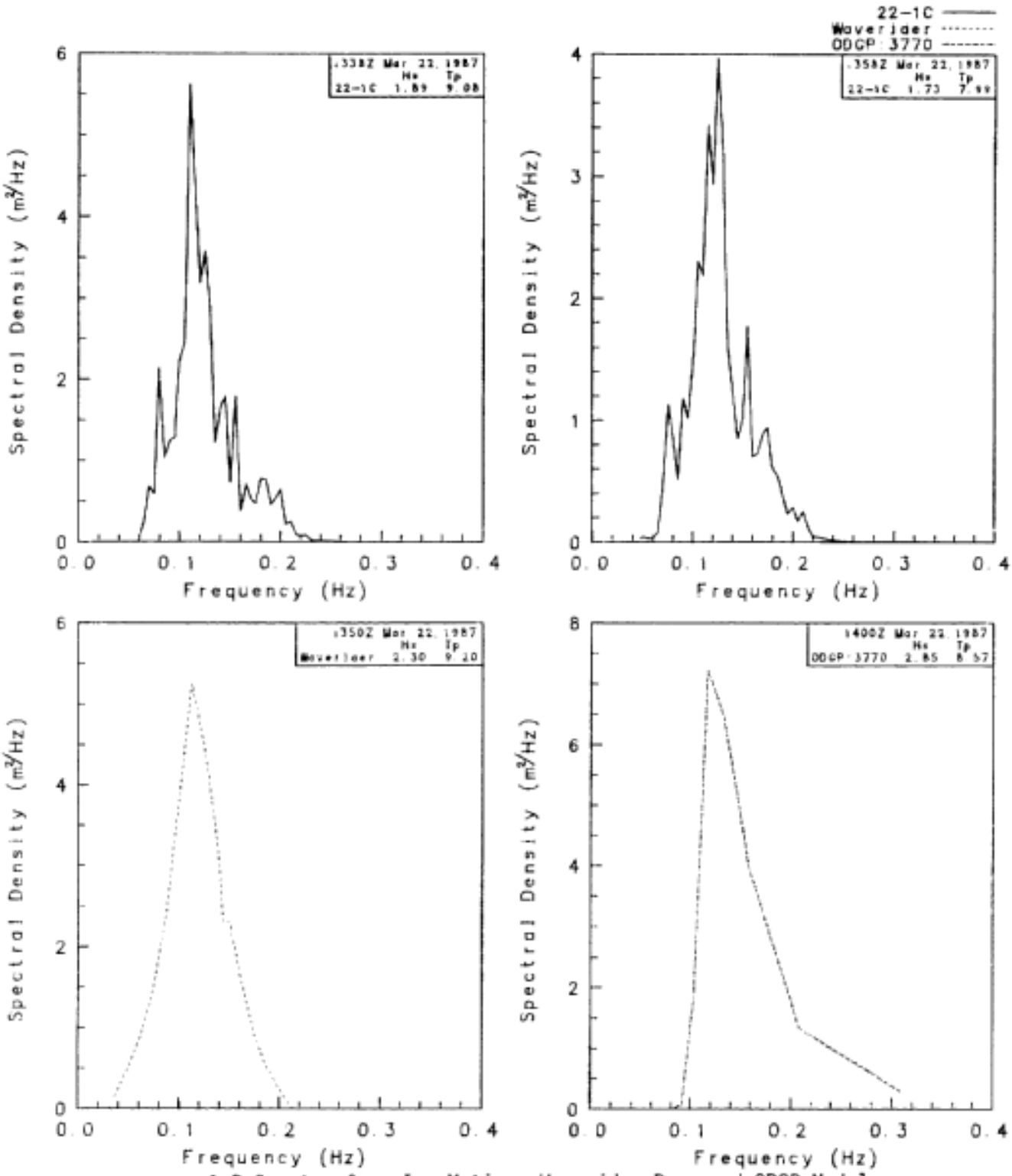

Figure 6.4 1-D Spectra from Ice Motion, Waverider Buoy and ODGP Model March 22, 1987.

LIMEX 87 ICE MOTION SPECTRA
Test No. 25-1C
25-03-87

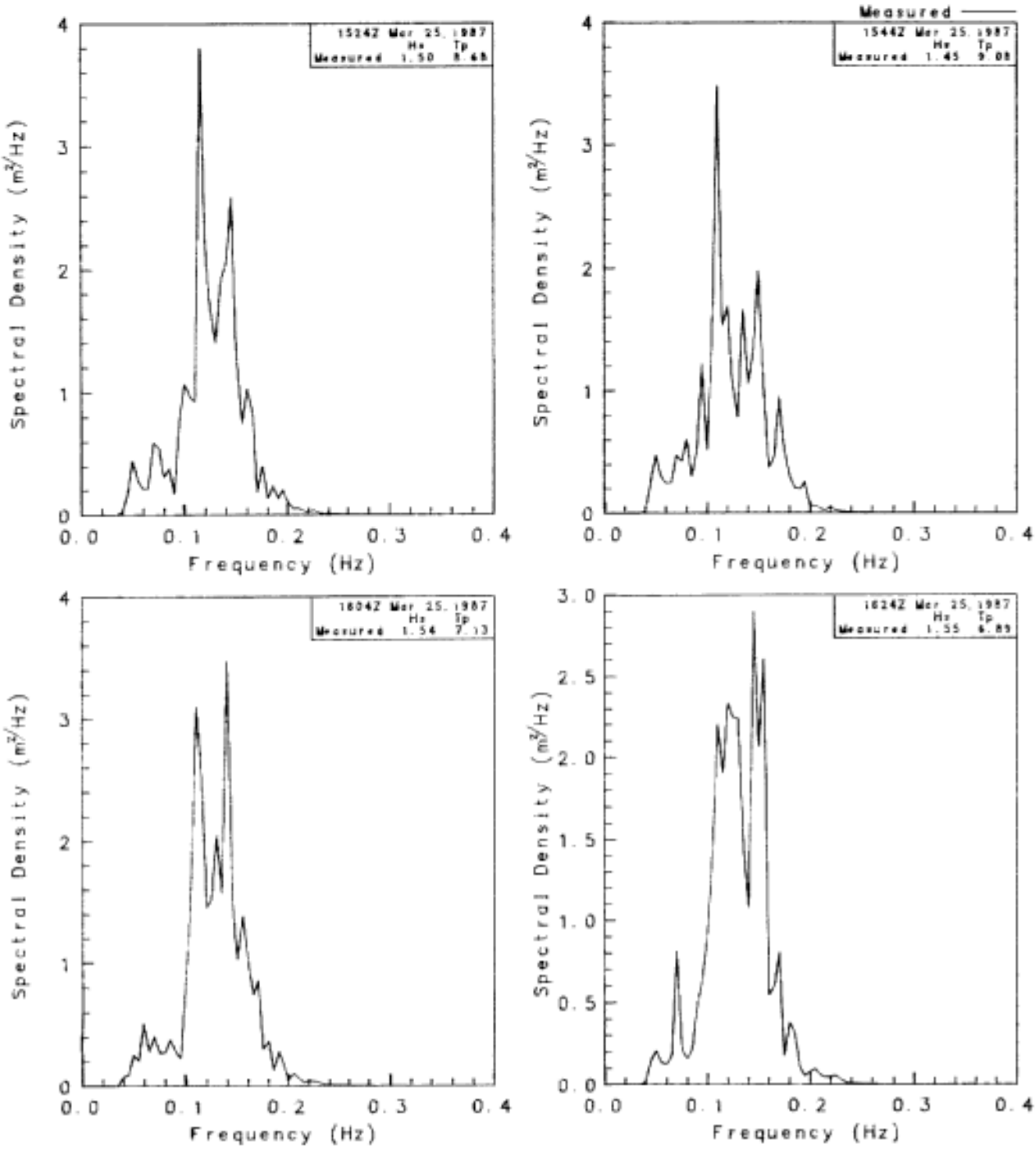

Figure 6.5

LIMEX 87 ICE MOTION SPECTRA
Test No. 25-1C
25-03-87

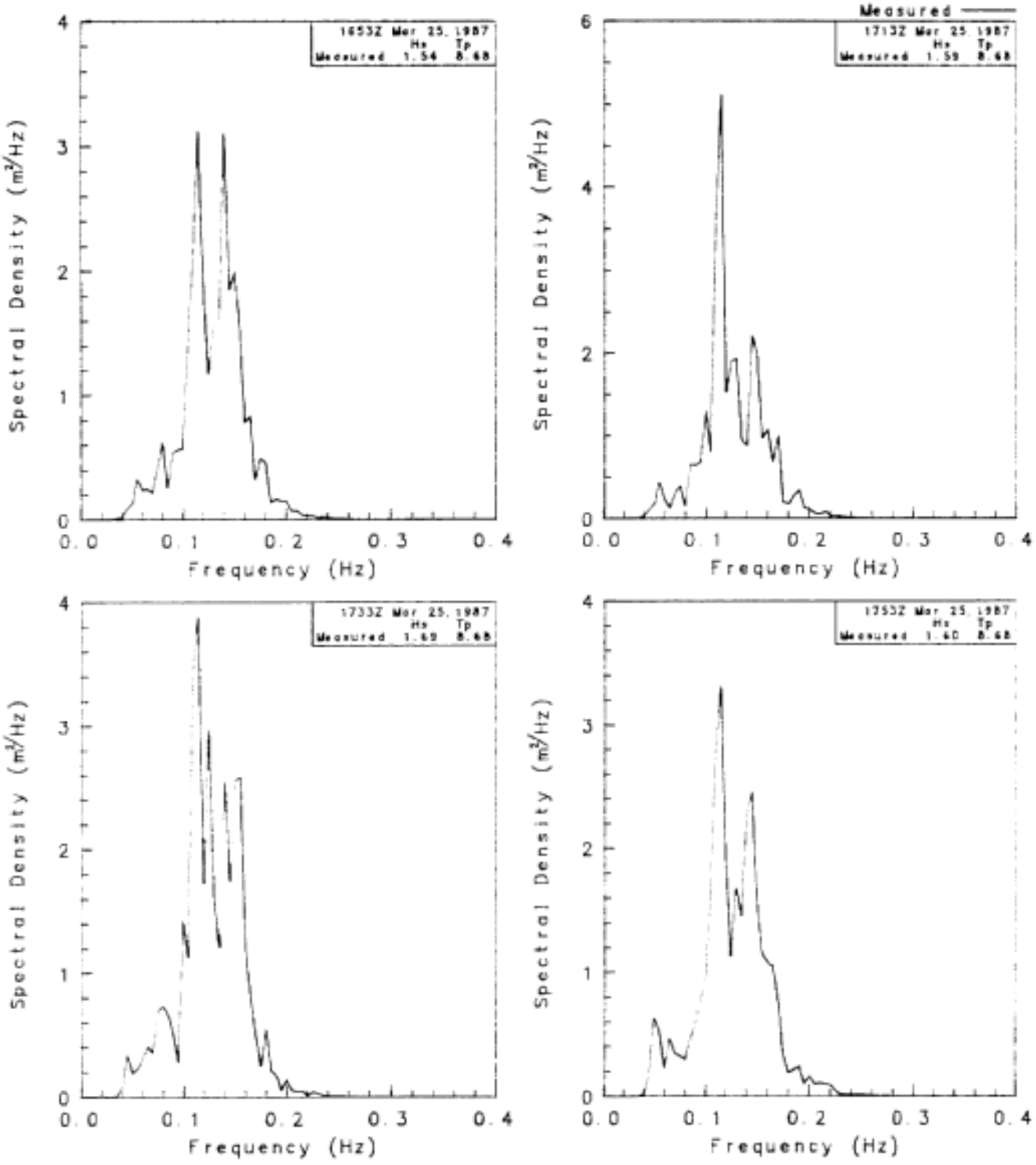

Figure 6.5 (cont'd)

LIMEX 87 ICE MOTION SPECTRA
Test No. 25-1C
25-03-87

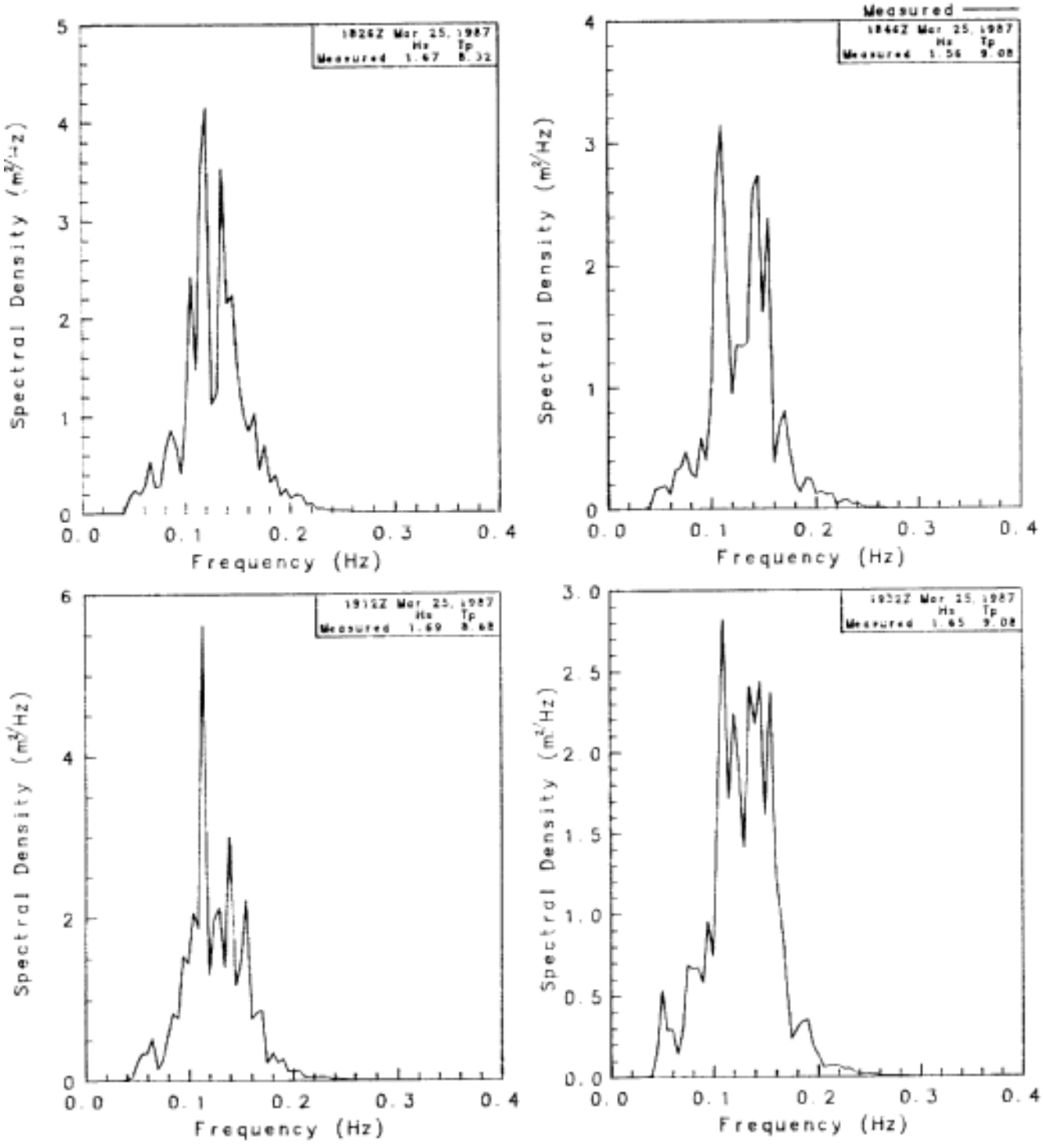

Figure 6.5 (cont'd)

LIMEX 87 ICE MOTION SPECTRA
Test No. 25-1C
25-03-87

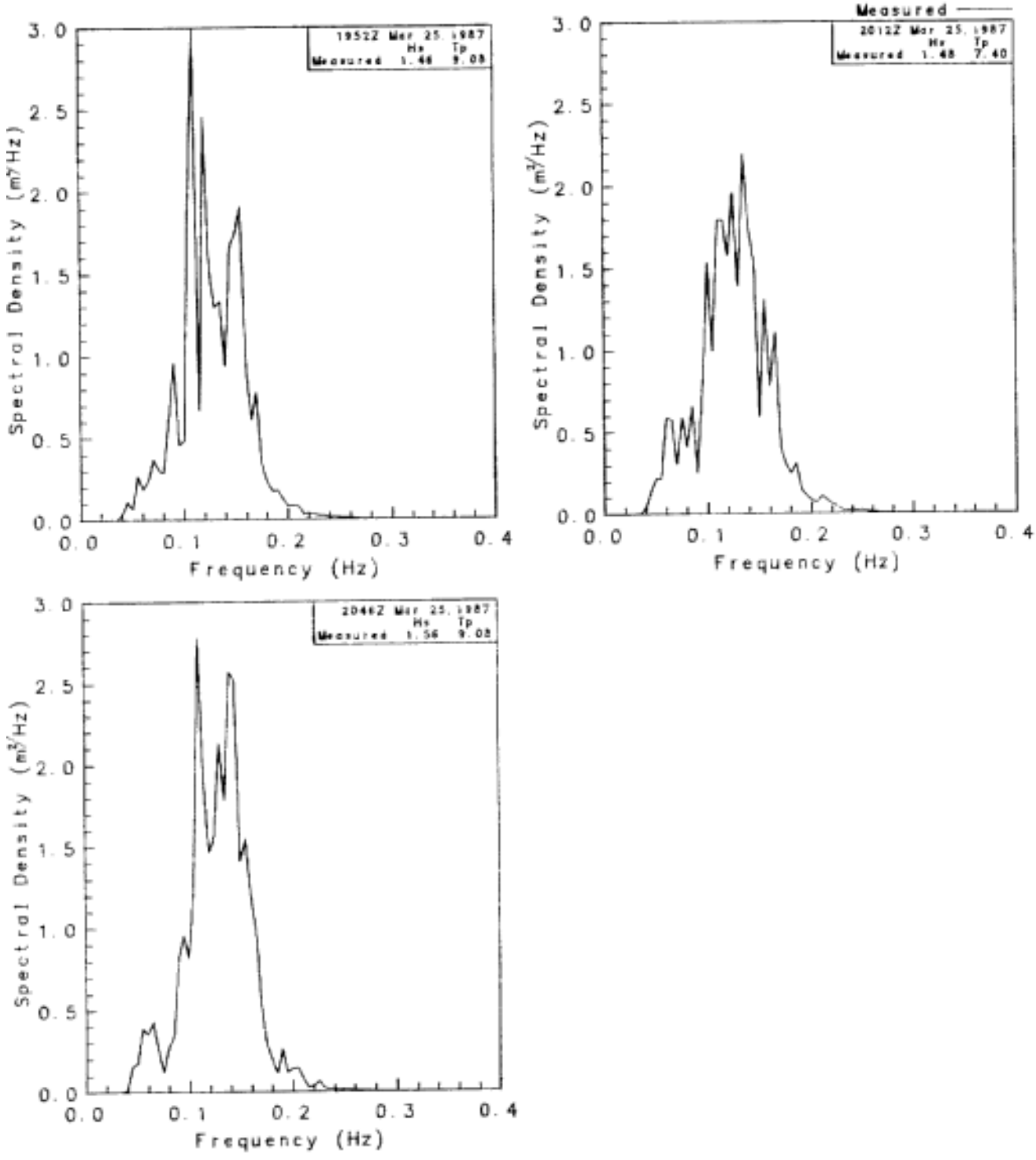

Figure 6.5 (cont'd)

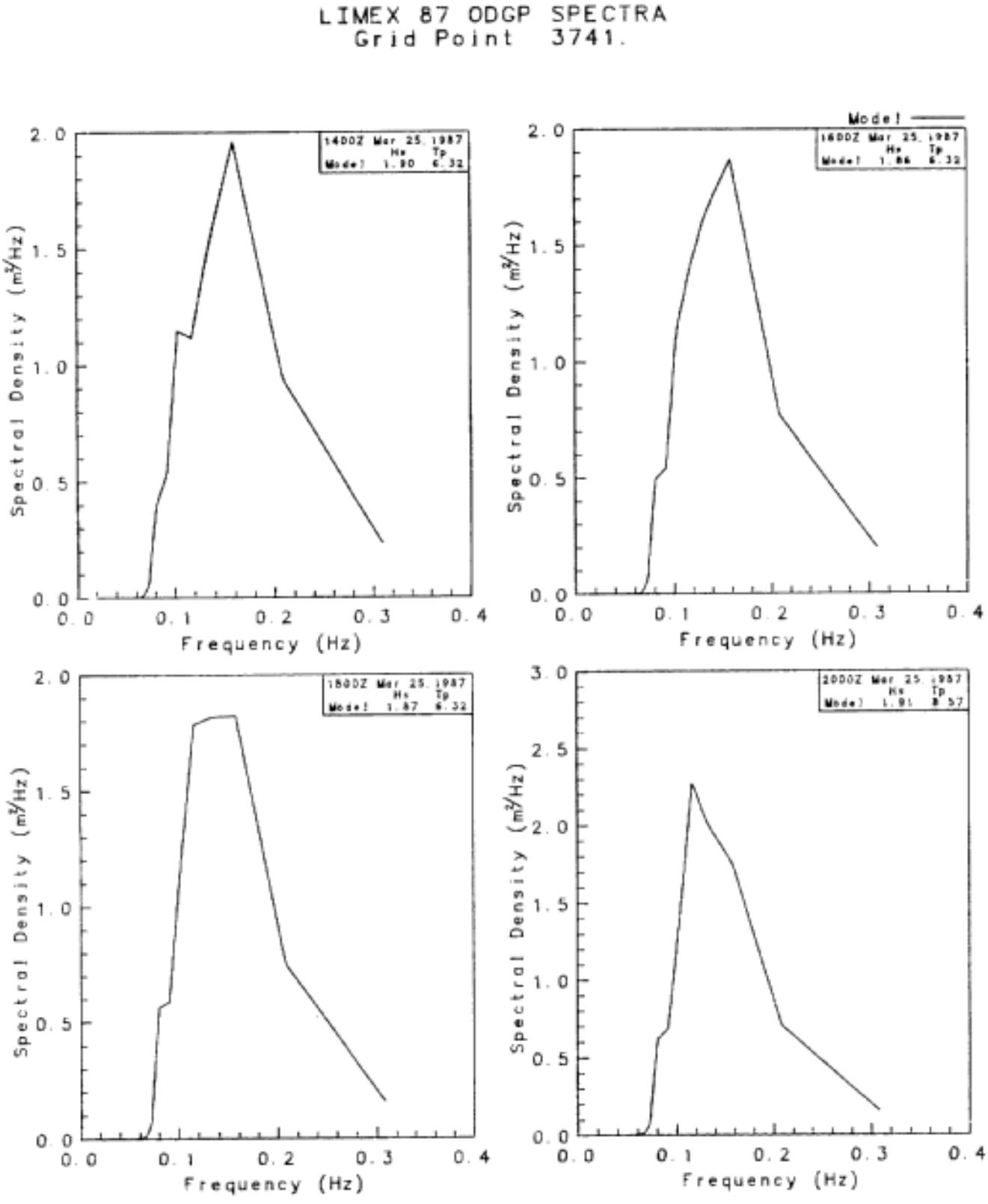

Figure 6.6 ODGP 1-D Spectra at Grip Point #3741
March 25, 1987

In Figure 6.4 , a noticeable attenuation in wave energy spectra, can be seen, especially in the high frequency side. A reduction in wave height from 2.85 m predicted by ODGP, and 2.3 m obtained from the waverider to 1.89 m from the ice motion package was found.

The deployment 25–1C extended over a period of 5% hours. The resulting nondirectional spectra from this deployment are shown in Figure 6.5 and the corresponding ODGP spectra are shown in Figure 6.6 . The spectral plots indicate that the ”wave” energy varied slightly with time during the deployment period. The variation in ”wave” energy indicates that dynamic conditions existed in the marginal ice zone near the ice edge. Although the ”wave” conditions varied with time, the prevailing ”wave” conditions remained relatively constant. Refer to Sections 3.2 and 5.3 for detailed description of ice condition near deployment locations.

Deployments 25–2B. 25–3B and 25–4B were placed at approximately 1, 2 and 4 km, respectively, into the ice zone whereas deployment 25–1C was near the ice edge, approximately 200–300 m inside MIZ. The ice motion of these deployments were obtained during the 25–1C deployment period. The objective of the deployments was to monitor the ”wave” energy as waves penetrated the ice zone, Figure 6.7 illustrates the change in the nondirectional ”wave” energy at various distances into the ice zone. In Figure 6.8 , the nondirectional spectra from deployment 25–1C during the same time period has been superimposed over the spectra from deployments 25–2B, 25–3B, and 25–4B.

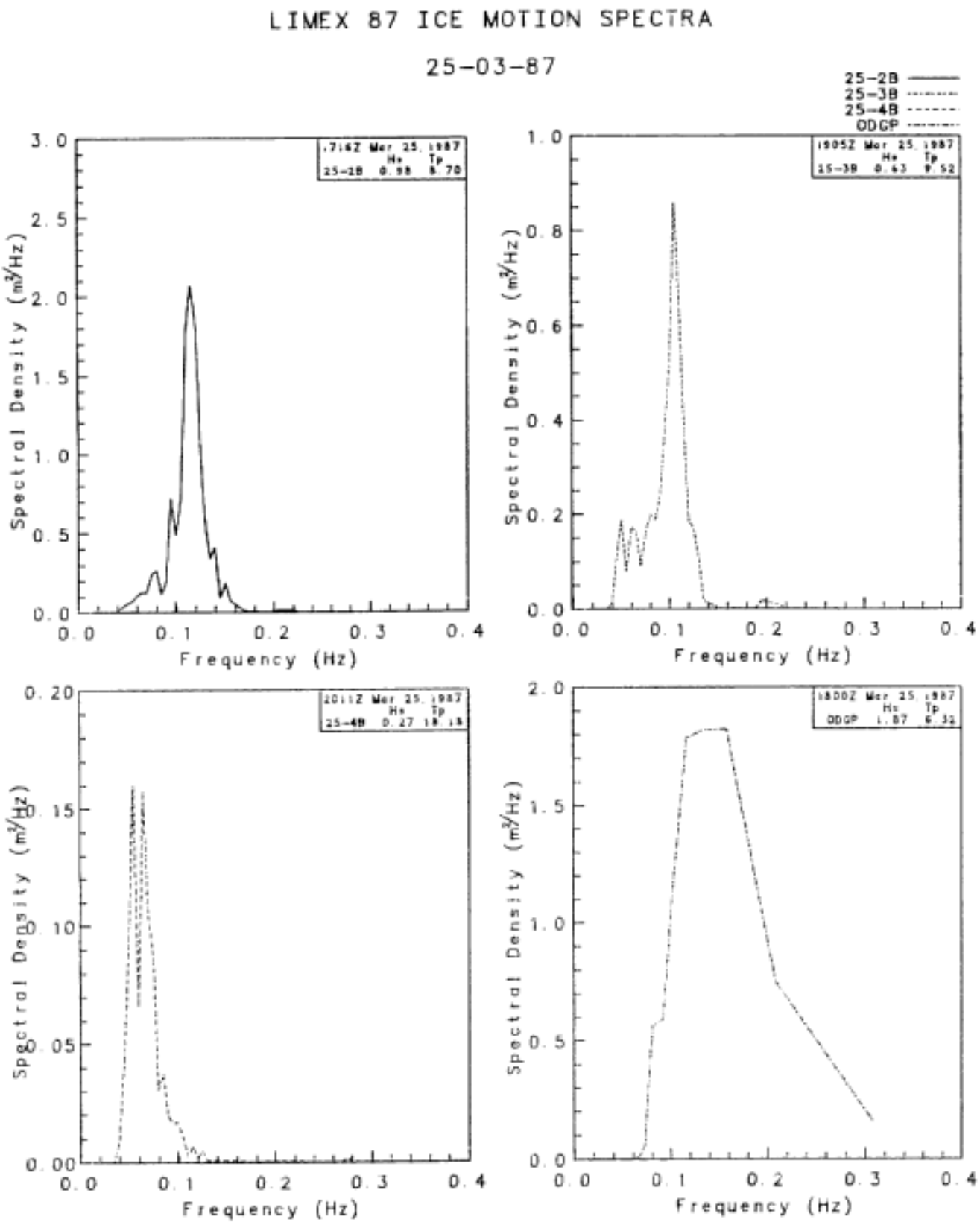
LIMEX 87 ICE MOTION SPECTRA
25-03-87
25-2B
25-3B
25-4B
ODGP
Spectral Density (m²/Hz)
Frequency (Hz)
0.0
0.1
0.2
0.3
0.4

Figure 6.7

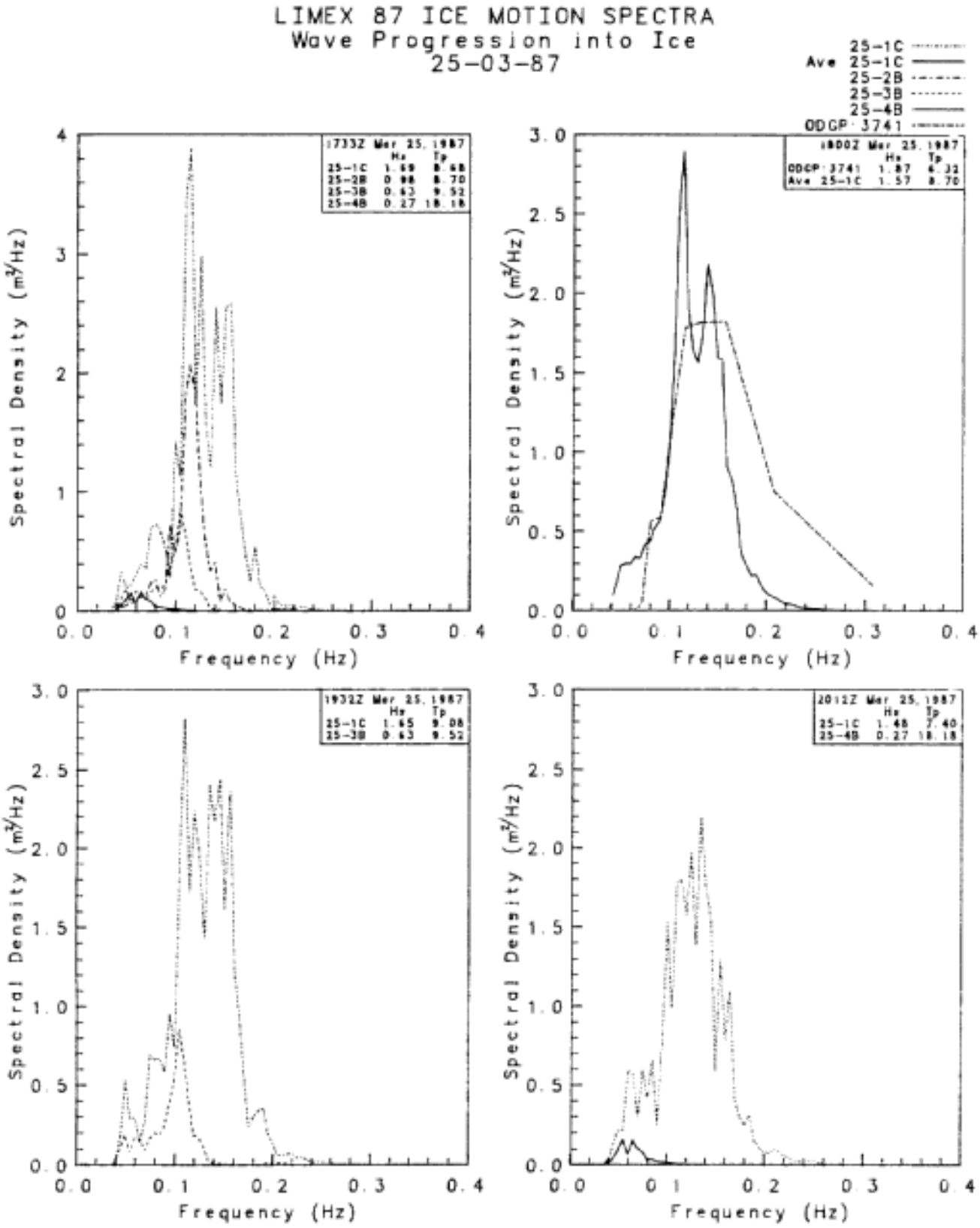
LIMEX 87 ICE MOTION SPECTRA
Wave Progression into Ice
25-03-87
25-1C
Ave 25-1C
25-2B
25-3B
25-4B
ODGP 3741
1733Z Mar 25, 1987
Hs Tp
25-1C 1.69 8.68
25-2B 0.98 8.70
25-3B 0.63 9.52
25-4B 0.27 18.18
1800Z Mar 25, 1987
Hs Tp
ODGP 3741 1.87 6.32
Ave 25-1C 1.57 8.70
1932Z Mar 25, 1987
Hs Tp
25-1C 1.65 9.08
25-3B 0.63 9.52
2012Z Mar 25, 1987
Hs Tp
25-1C 1.48 7.40
25-4B 0.27 18.18
Spectral Density (m²/Hz)
Frequency (Hz)

Figure 6.8

As shown in Figure 6.5 , the shape and characteristics of the spectral density plots from the 25–1C package measurements (i,e, 15–20 minute records) are similar. Each plot exhibited prominent primary and secondary peaks and several other smaller energy–contents peaks. The computed significant wave height from the 15 spectra did not vary significantly throughout the 5 hour deployment period (Hs varied between 1.5 m to 1.7 m). The primary and secondary peak periods were mostly about 9 and 6.5 s. respectively. The ODGP hindcast provided Hs in the order of 1.9 m and peak period about 9.5.

A comparison of the spectra at various distances into the ice zone indicates a decrease in the spectral energy with increasing distance into the ice zone. Further comparison indicates that the higher frequencies are attenuated much faster by the ice field than the lower frequencies.

The data recovered from deployment 26–1B covers only a 5 minute time period. For this reason, the nondirectional spectrum was not included since the data would not reflect the ”wave” conditions. Deployments 26–2C and 26–3B produced two similar nondirectional energy spectra and were included in Figure 6.9 . The nondirectional spectra from ODGP grid point 3741 have been included (see Figure 6.3 for ODGP grid points location). The ODGP spectra indicates a smaller wave height with a higher frequency than seen during the 22–1C and 25–XX deployments. The results from the 26–2C and 26–3B deployments are unusual in that the wave height and peak period appears to have increased at the ice edge. If this is the case, either the 15 second period of the ice motion represents the resonant frequency of the ice floe, or a shift in wave energy from 10 seconds to 15 seconds has occurred.

6.2.2 Directional Energy Spectra

The validity of any directional wave spectra obtained using ice floe motion measurements may have to be checked by comparing the directional spreading seen inside and outside of the pack ice on occasions where open water spectra are available.

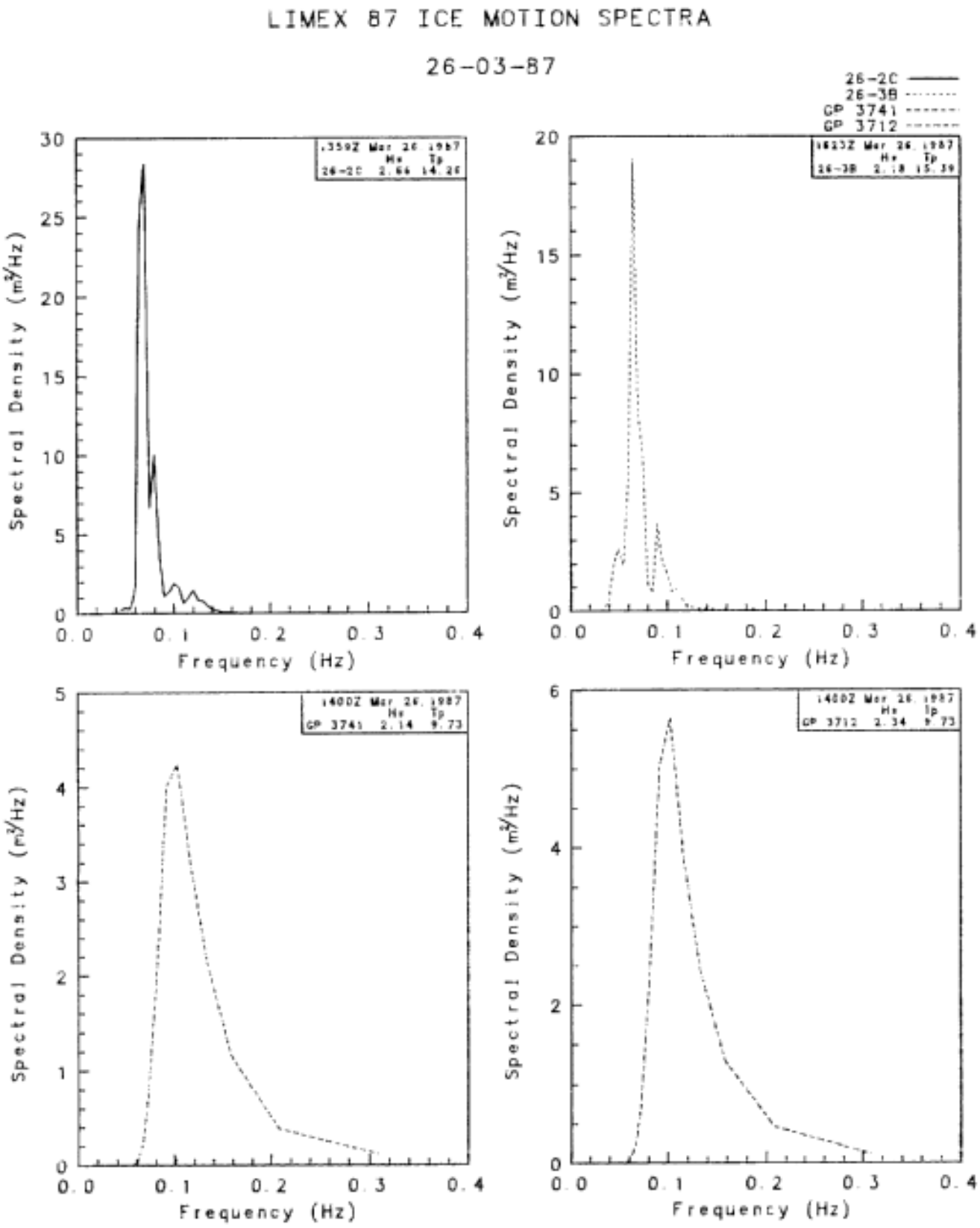
LIMEX 87 ICE MOTION SPECTRA
26-03-87
26-2C
26-3B
GP 3741
GP 3712
Spectral Density (m²/Hz)
Frequency (Hz)
0.0
0.1
0.2
0.3
0.4

Figure 6.9

The directional energy spectra $E(f,\phi)$ for the ice package deployments can be approximated using the co–spectra values C_{11}, C_{22}, C_{23}, C_{33}, and the quadrature spectra values Q_{12}, Q_{13} where the subscript 1 denotes heave, 2 denotes slope in the North direction, and 3 denotes slope in the West direction (see Figure 6.1). To change the left hand system to a right hand Cartesian system, the Signs Q_{13} and C_{23} are changed. The C_{ij} and Q_{ij} values represent spectral energies ”coming from” a certain direction.

Care must be taken when the 6 spectra are incorporated into an estimation of $E(f.\phi)$. Firstly, the angle $\phi = 0$ represents the average orientation of the sensor package x axis for that deployment. This will be an angle of η_3 degrees counterclockwise from magnetic nor that the package location for that deployment as shown in Figure 6.1 . The value of η_3 has been included in the file header on the supplied magnetic tape. The axis is then rotated by η_3 for magnetic North, and -25° to true North.

The directional energy spectra $E(f.\phi)$ can be approximated from the Fourier expansion.

$$E(F,\phi) = \tfrac{1}{2}a_o(f) + a_1(f)\cos\phi + b_1(f)\sin\phi + a_2(f)\cos 2\phi + b_2(f)\sin 2\phi$$

where the coefficients $a_i(f)$, $b_i(f)$ are determined from C_{11}, C_{22}, C_{23}, C_{33}, Q_{13}, Q_{12}, see Longuet–Higgins et al, (1963). However, the Fourier expansion often tends to produce negative energies. A modified version or weighted average of the Fourier expansion has been introduced which tends to eliminate these negative values, and is given by

$$E(f,\phi) = \tfrac{1}{2}a_o(f) + 2/3\, a_1(f)\cos\phi + 2/3\, b_1(f)\sin\phi + 2/6\, a_2(f)\cos 2\phi + 2/6\, b_2(f)\sin 2\phi$$

A more detailed description of the modified Fourier expansion can be found in Longuet–Higgins et al. (1963).

Alternative methods developed by Oltman–Shay and Guza (1984), called maximum likelihood method, and Lygre and Krogstad (1986), called maximum entropy method, were examined. In Taylor (1987), a maximum likelihood and a maximum entropy method was applied to the Fourier expansion. The results of the maximum likelihood and maximum entropy methods were compared to results from the modified or weighted average method obtained from a known input. The comparison indicated that the weighted average method tended to broaden the directional spectrum, and tended to ”overlook” small peaks in the spectrum. The choice of the most appropriate technique requires more investigation.

The 2–D directional energy spectra $E(f,\phi)$ can best be portrayed in contour polar plots, as shown in Figure 6.10 . In Figure 6.10 , the

weighted average and maximum likelihood methods were applied to the spectra obtained from deployment 22–1C. The weighted average technique indicates one broad peak, while the maximum likelihood method indicates two. The features of the two methods are very similar, but with the maximum likelihood method showing a better resolution. However, caution must be used in the interpretation of the results. The maximum likelihood method, will be used in the following analysis since it produces a tighter energy spectra.

The directional spectra from the ODGP hindcast have been obtained for grid points near the deployment sites. The ODGP directional wave spectra was compared to directional wave spectra obtained from in situ and remote sensing data period, and has shown fairly accurate conditions (Beal, 1988, personal communications). Since no directional wave measurements were collected outside the ice edge at the time of the deployments, the ODGP hindcast spectra can be used to indicate the open water wave conditions. The locations of the ice package deployments relative to the ODGP grid points are shown in Figure 6.3 .

The directional spectra obtained from deployment 22–1C is shown in Figure 6.11 . A comparison of the two plots indicates the ”wave” conditions did not change much with time. The directional spectra of the ODGP grid point 3770 is shown in Figure 6.12 . A comparison of the ice package spectra and the ODGP spectra indicates that the waves in the ice edge are affected by the ice floes. The ice package indicates the average wave direction is towards the south–west which agrees with the ODGP spectra. However, the ice package indicates two peaks of energy. It is not sure whether the motion is due to reflection or is due to energy dissipation. A directional waverider buoy will have to be deployed nearby the ice floe to determine the effects of the ice floe on the motion measured by the ice package.

In deployment 25–1C, the ice package was placed on a floe inside the edge of the ice zone. Since the deployment spans over 5 hours, any changes in wave conditions inside the ice field should be observed during the deployments 25–2B. 25–3B and 25–4B. During the 25–1C deployment, the directional energy spectra of the ice package is shown in Figure 6.13 . During the same period, the directional wave spectra from ODGP grid point 3741 is shown in Figure 6.14 . A comparison of the ice package spectra to the ODGP spectra shows that the ice package motion is very different during the first half of the deployment. Towards the end of the package deployment, the two spectra become more similar.

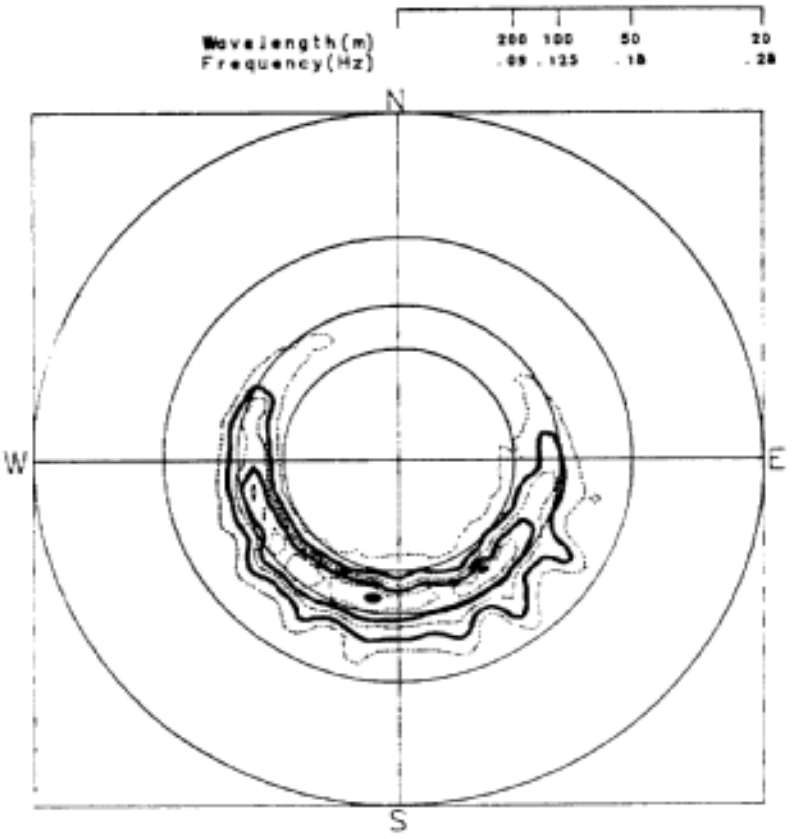

WEIGHTED AVERAGE METHO

ICE PACKAGE : 22-1C

22-03-87 13:38:35 GMT

Sig. Wave Ht. = 1.9 m
Peak Period = 9.1 s
Peak going towards 156. T
Contour spacing 0.134 m**2/Hz
Peak Energy 1.924 m**2/Hz

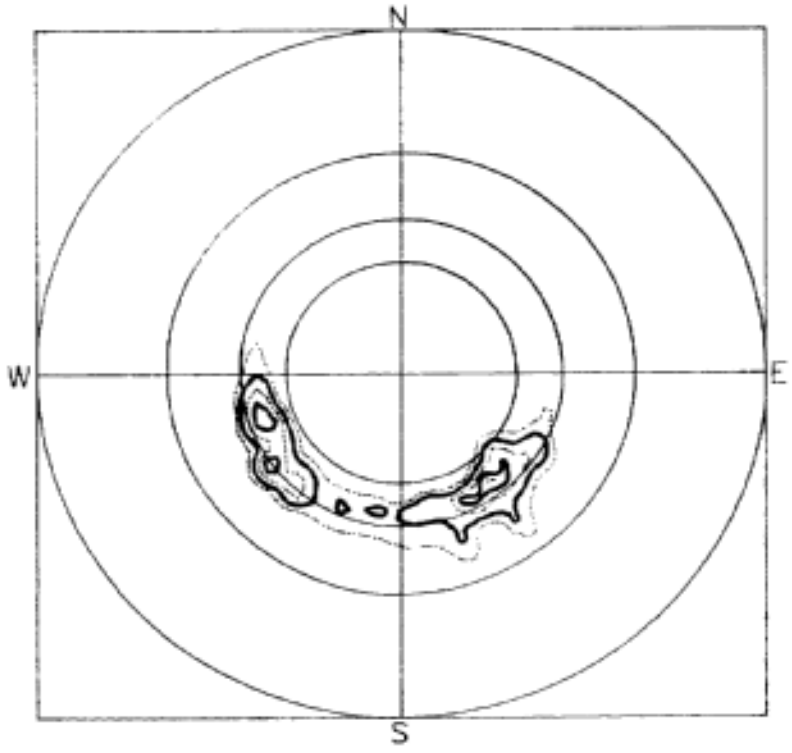

MAXIMUM LIKELIHOOD

ICE PACKAGE : 22-1C

22-03-87 13:38:35 GMT

Sig. Wave Ht. = 1.9 m
Peak Period = 9.1 s
Peak going towards 156. T
Contour spacing 0.279 m**2/Hz
Peak Energy 4.020 m**2/Hz

Figure 6.10

At the start of deployment 25–1C, 1524Z, the analysis produced two peaks. The larger peak, with a period between 6 and 7 seconds appears to be moving towards the north–northeast, and the second smaller peak with a period of approximately 9 seconds was moving towards the north–west. The ODGP model at 1800z. indicates two peaks; the larger peak at approximately 9 seconds was moving towards the south–southwest, and the smaller broader peak at 6–7 seconds is moving towards the west–southwest. A comparison of these two plots show no similarity between the ODGP spectra and the ice motion package.

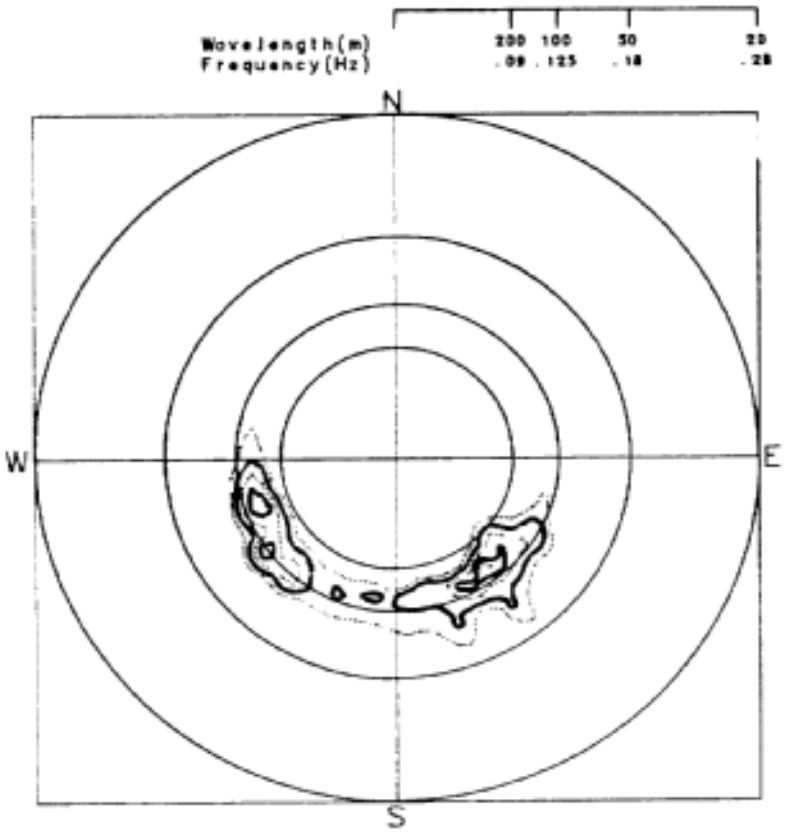

ICE MOTION PACKAGE

22-1C

22-03-87 13:38:35 GMT

Sig. Wave Ht. = 1.9 m
Peak Period = 9.1 s
Peak going towards 156. T
Contour spacing 0.279 m**2/Hz
Peak Energy 4.020 m**2/H

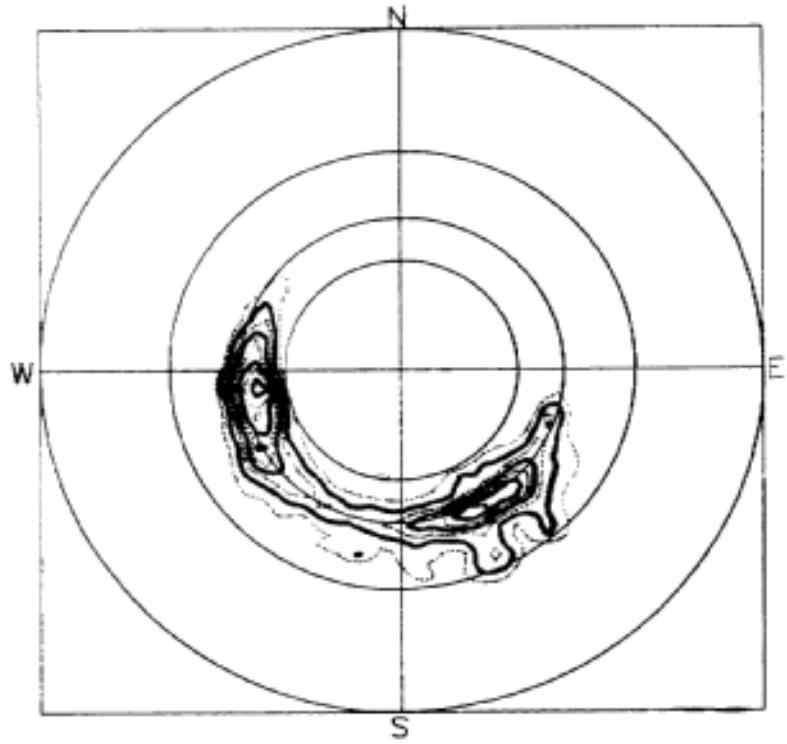

ICE MOTION PACKAGE

22-1C

22-03-87 13:58:35 GMT

Sig. Wave Ht. = 1.7 m
Peak Period = 8.0 s
Peak going towards 261. T
Contour spacing 0.161 m**2/Hz
Peak Energy 2.317 m**2/H

Figure 6.11

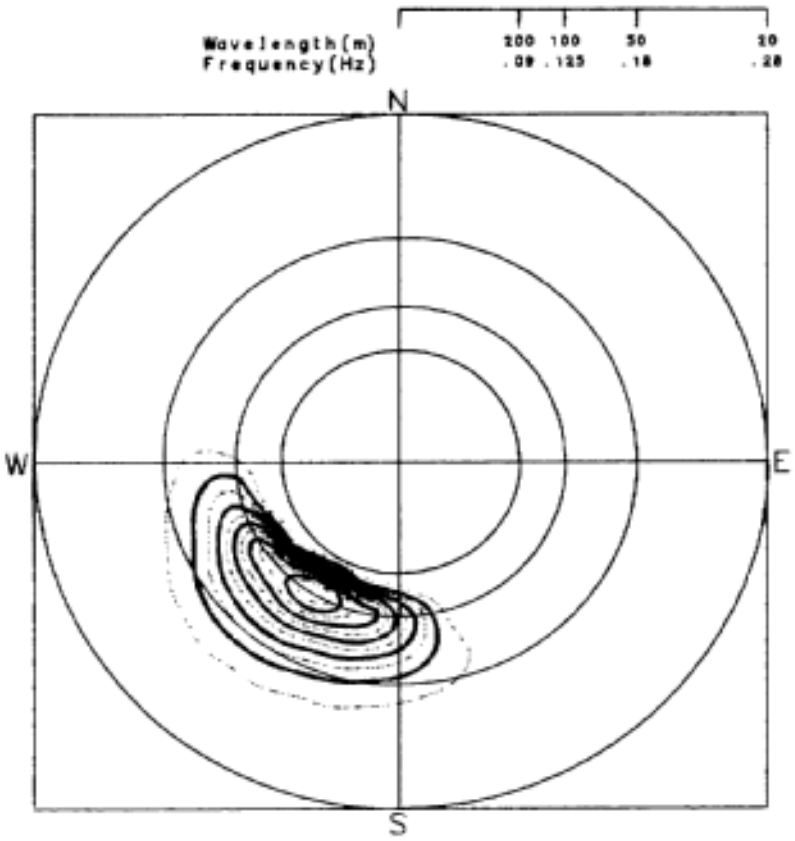

ODGP HINDCAST

Grid point : 3770.

8703.2212. GMT

Sig. Wave Ht. = 2.7 m

Peak Period = 8.6 s

Peak going towards 218. T

Contour spacing 0.095 m**2/Hz

Peak Energy 1.368 m**2/H

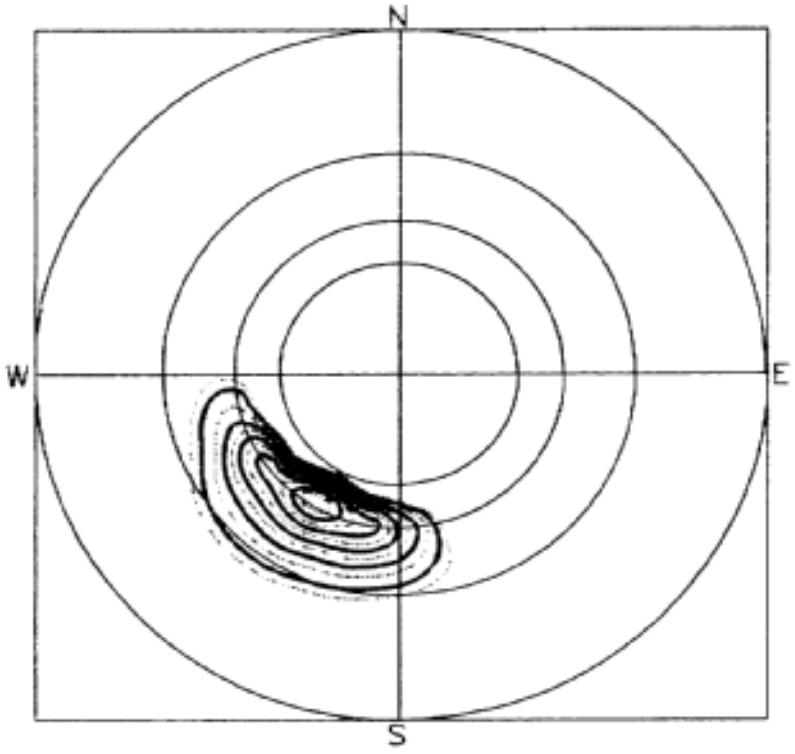

ODGP HINDCAST

Grid point : 3770.

8703.2214. GMT

Sig. Wave Ht. = 2.9 m

Peak Period = 8.6 s

Peak going towards 218. T

Contour spacing 0.108 m**2/Hz

Peak Energy 1.557 m**2/H

Figure 6.12

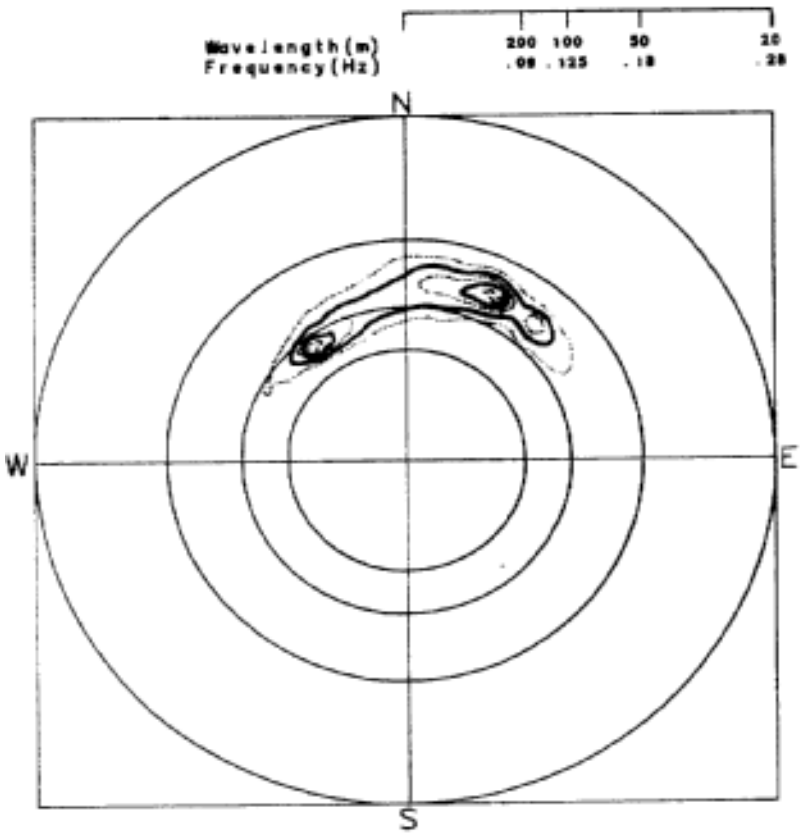

ICE MOTION PACKAGE

25–1C

25–03–87 15:24:42 GMT

Sig. Wave Ht. = 1.5 m
Peak Period = 8.7 s
Peak going towards 29. T
Contour spacing 0.215 m**2/Hz
Peak Energy 3.102 m**2/Hz

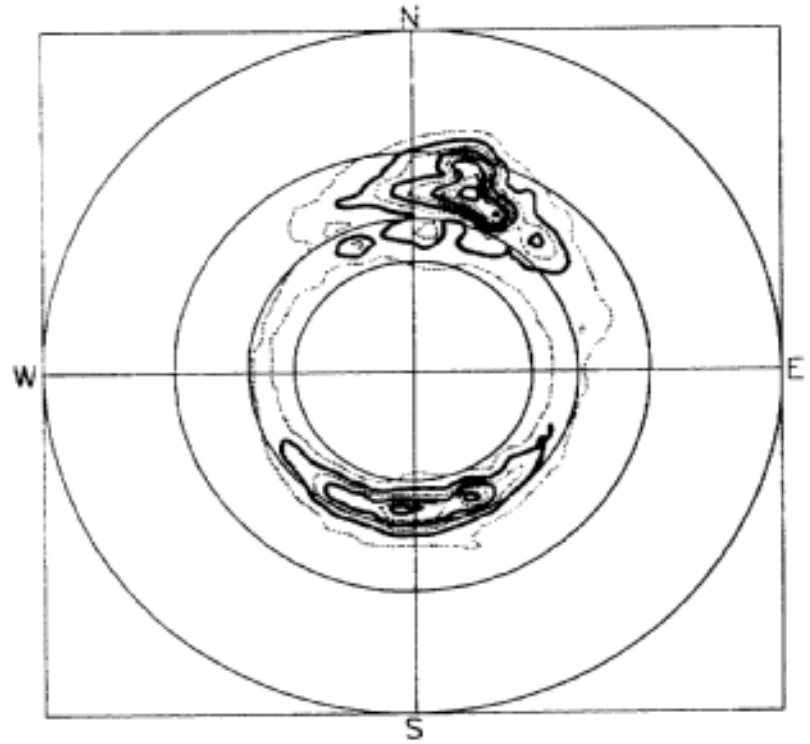

ICE MOTION PACKAGE

25–1C

25–03–87 15:44:42 GMT

Sig. Wave Ht. = 1.4 m
Peak Period = 9.1 s
Peak going towards 20. T
Contour spacing 0.094 m**2/Hz
Peak Energy 1.348 m**2/Hz

Figure 6.13

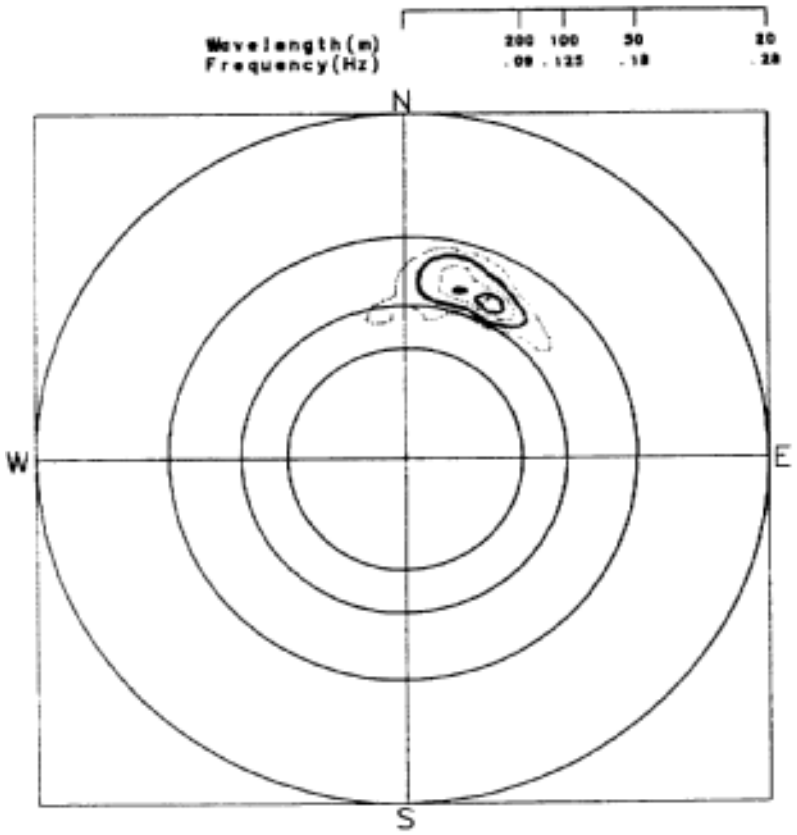

ICE MOTION PACKAGE

25-1C

25-03-87 16:04:43 GMT

Sig. Wave Ht. = 1.5 m
Peak Period = 7.1 s
Peak going towards 26. T
Contour spacing 0.238 m**2/Hz
Peak Energy 3.432 m**2/Hz

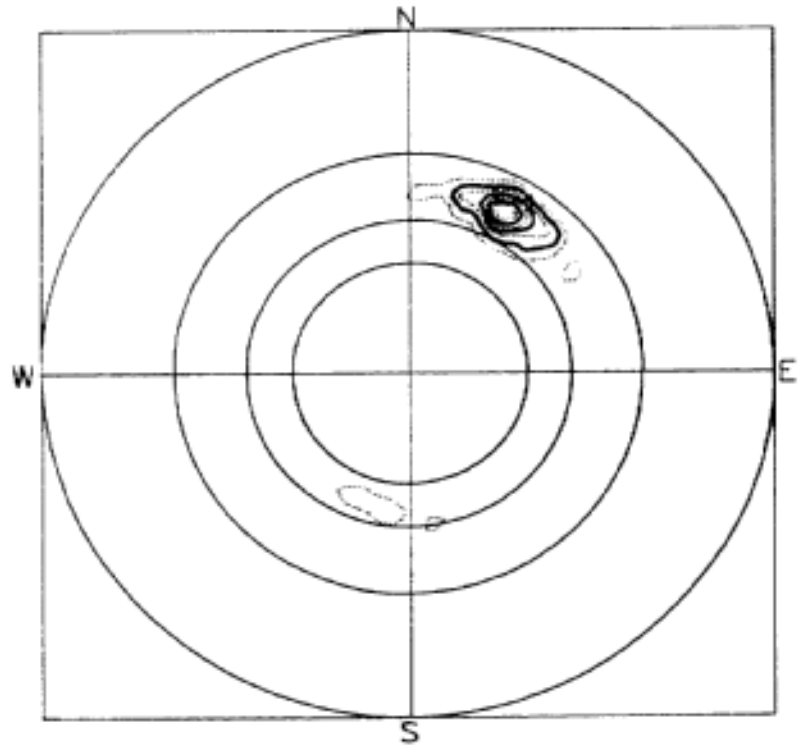

ICE MOTION PACKAGE

25-1C

25-03-87 16:24:44 GMT

Sig. Wave Ht. = 1.6 m
Peak Period = 6.9 s
Peak going towards 35. T
Contour spacing 0.245 m**2/Hz
Peak Energy 3.532 m**2/Hz

Figure 6.13 (Cont'd)

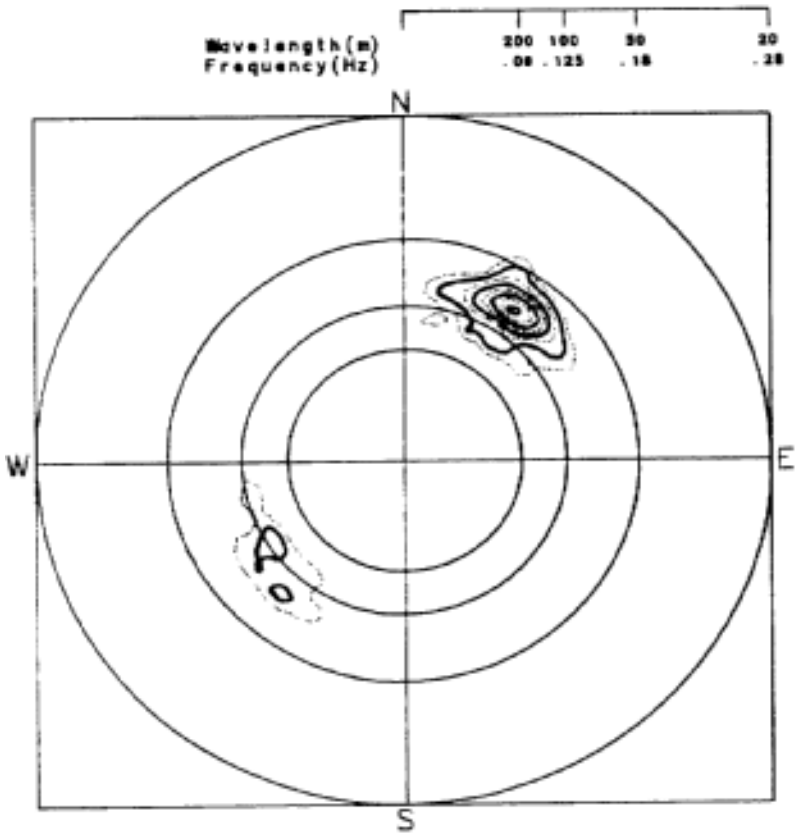

ICE MOTION PACKAGE

25-1C

25-03-87 16:53:12 GMT

Sig. Wave Ht. = 1.5 m
Peak Period = 8.7 s
Peak going towards 33. T
Contour spacing 0.196 m**2/Hz
Peak Energy 2.825 m**2/Hz

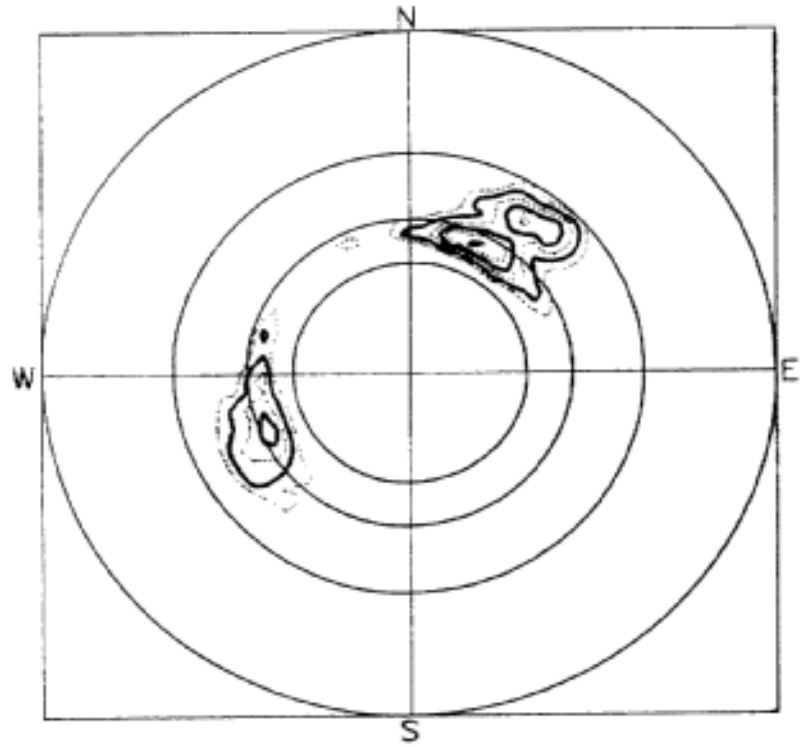

ICE MOTION PACKAGE

25-1C

25-03-87 17:13:12 GMT

Sig. Wave Ht. = 1.6 m
Peak Period = 8.7 s
Peak going towards 24. T
Contour spacing 0.198 m**2/Hz
Peak Energy 2.856 m**2/Hz

Figure 6.13 (Cont'd)

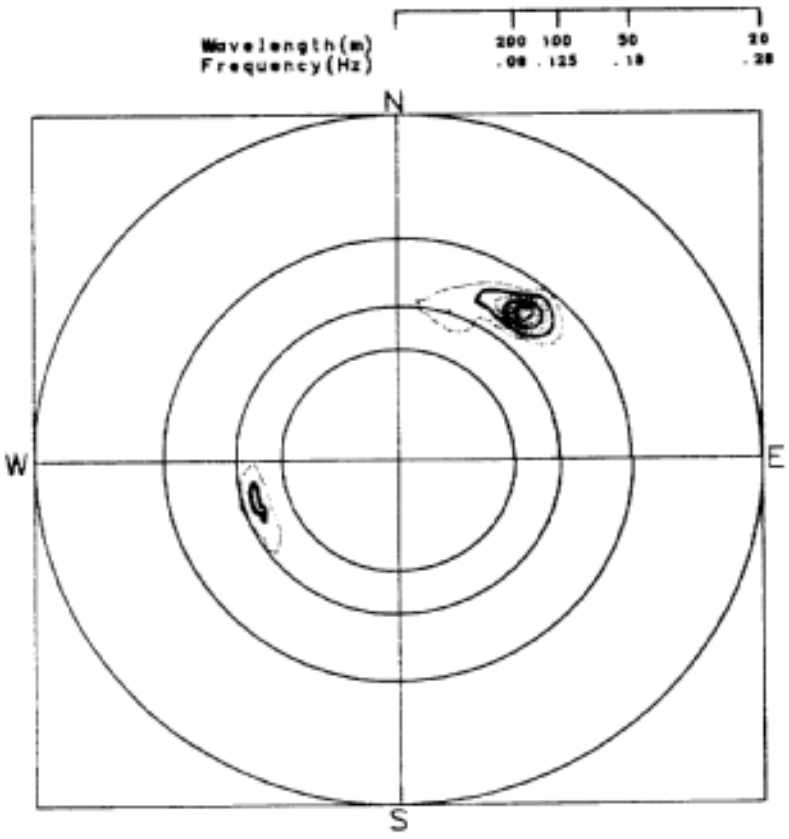

ICE MOTION PACKAGE

25-1C

25-03-87 17:33:13 GMT

Sig. Wave Ht. = 1.7 m
Peak Period = 8.7 s
Peak going towards 37. T
Contour spacing 0.391 m**2/Hz
Peak Energy 5.627 m**2/Hz

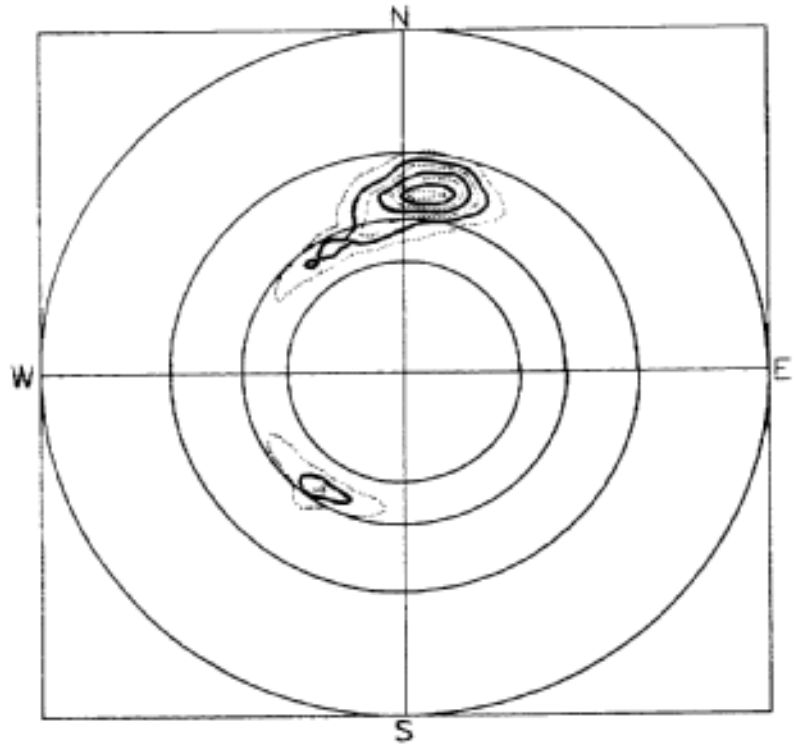

ICE MOTION PACKAGE

25-1C

25-03-87 17:53:14 GMT

Sig. Wave Ht. = 1.6 m
Peak Period = 8.7 s
Peak going towards 3. T
Contour spacing 0.228 m**2/Hz
Peak Energy 3.285 m**2/Hz

Figure 6.13 (Cont'd)

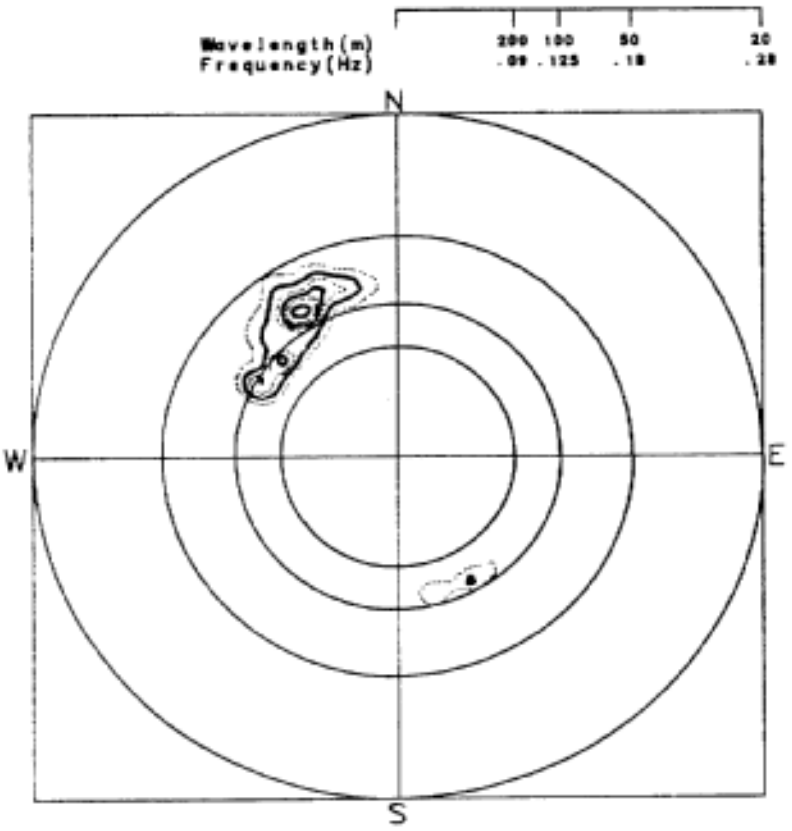

ICE MOTION PACKAGE

25–1C

25–03–87 18:28:32 GMT

Sig. Wave Ht. = 1.7 m
Peak Period = 8.3 s
Peak going towards 313. T
Contour spacing 0.327 m**2/Hz
Peak Energy 4.714 m**2/Hz

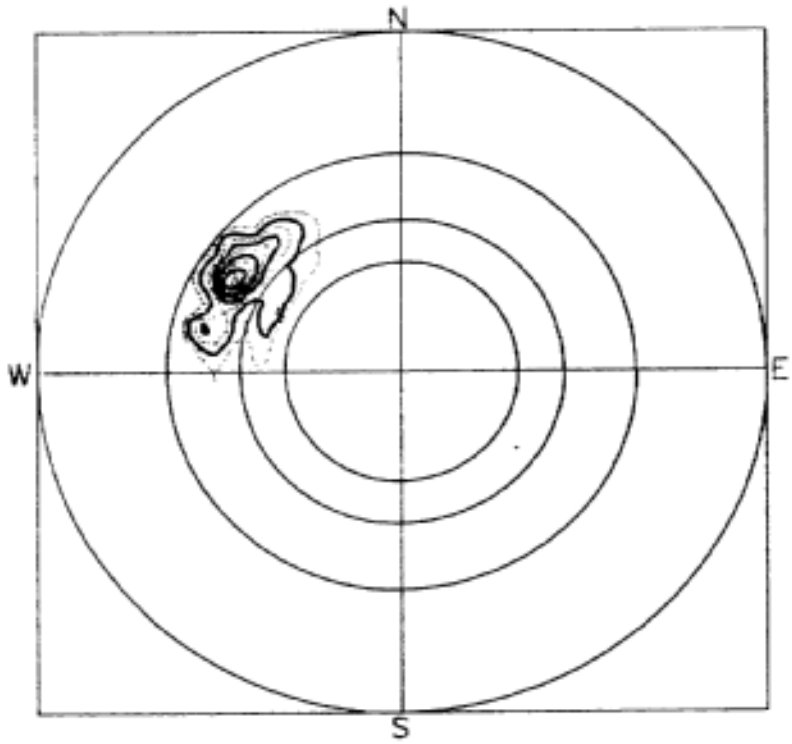

ICE MOTION PACKAGE

25–1C

25–03–87 18:46:32 GMT

Sig. Wave Ht. = 1.6 m
Peak Period = 9.1 s
Peak going towards 296. T
Contour spacing 0.245 m**2/Hz
Peak Energy 3.523 m**2/Hz

Figure 6.13 (Cont'd)

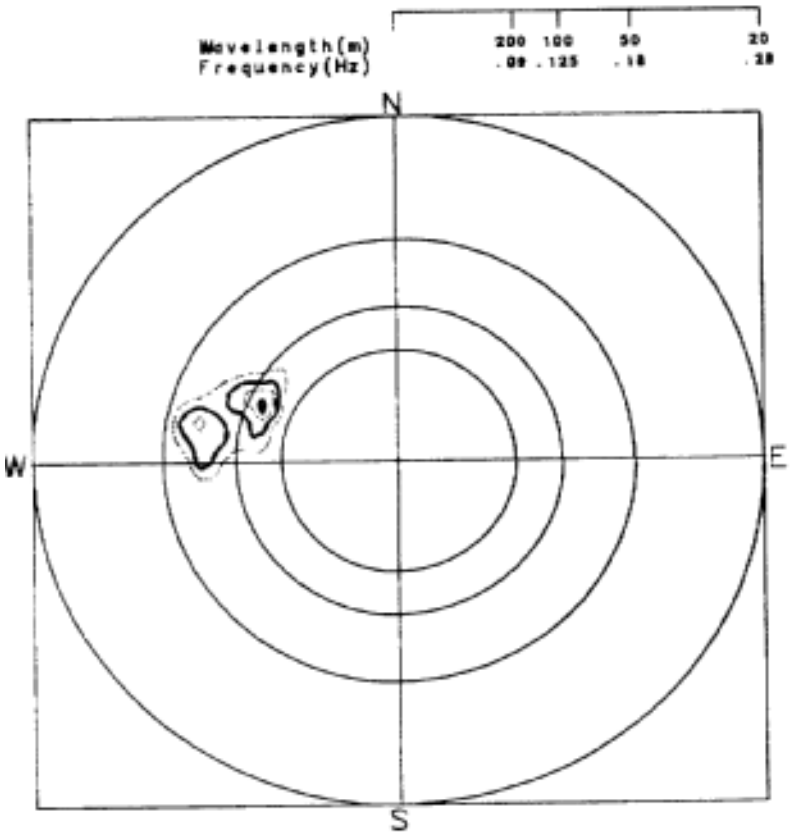

ICE MOTION PACKAGE

25-1C

25-03-87 19:12:40 GMT

Sig. Wave Ht. = 1.7 m
Peak Period = 8.7 s
Peak going towards 291. T
Contour spacing 0.495 m**2/Hz
Peak Energy 7.133 m**2/Hz

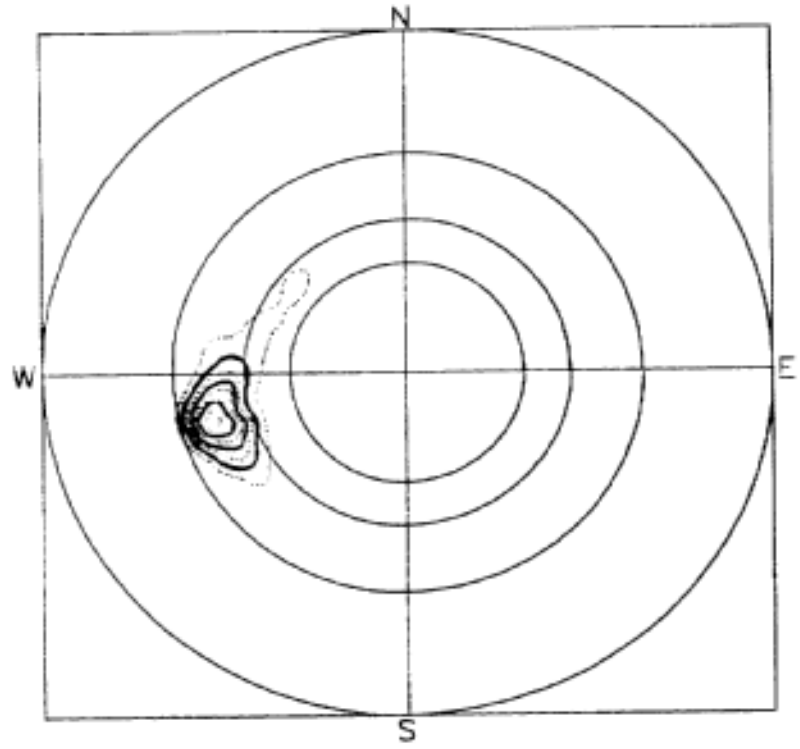

ICE MOTION PACKAGE

25-1C

25-03-87 19:32:40 GMT

Sig. Wave Ht. = 1.6 m
Peak Period = 9.1 s
Peak going towards 255. T
Contour spacing 0.353 m**2/Hz
Peak Energy 5.082 m**2/Hz

Figure 6.13 (Cont'd)

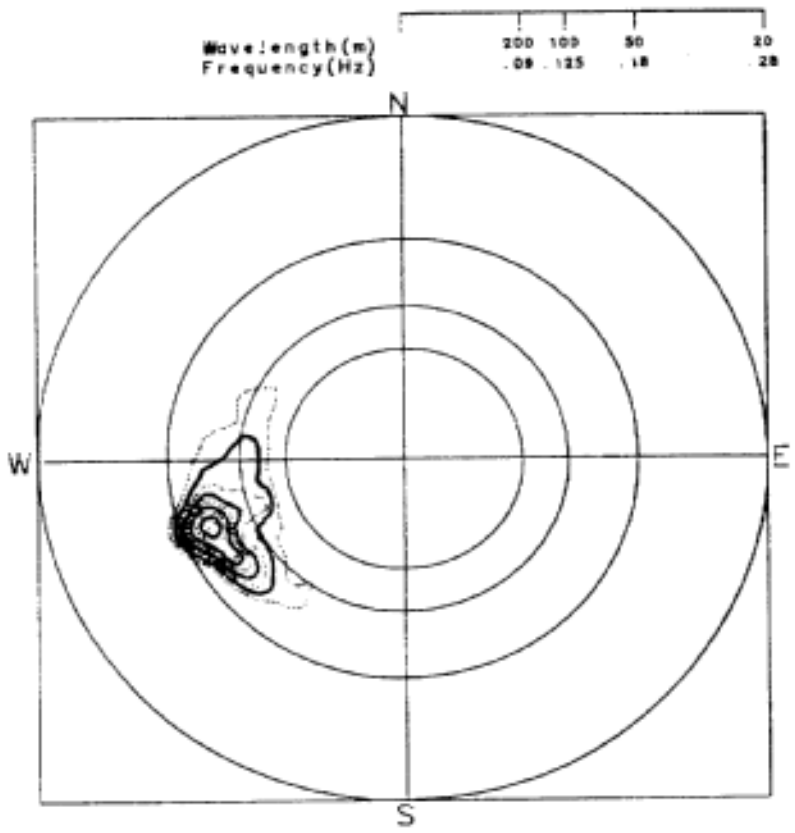

ICE MOTION PACKAGE

25-1C

25-03-87 19:52:41 GMT

Sig. Wave Ht. = 1.5 m
Peak Period = 9.1 s
Peak going towards 247. T
Contour spacing 0.214 m**2/Hz
Peak Energy 3.083 m**2/Hz

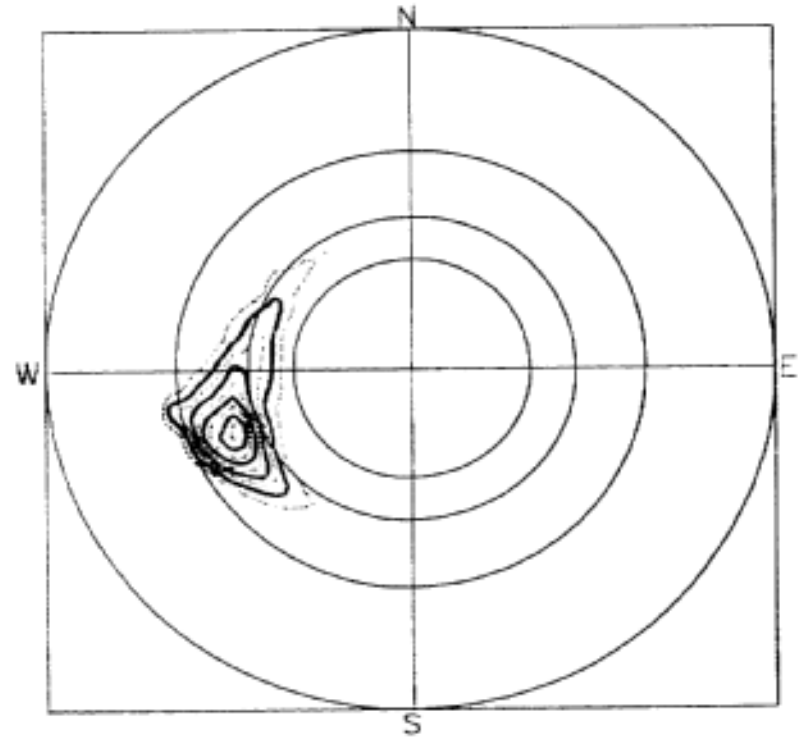

ICE MOTION PACKAGE

25-1C

25-03-87 20:12:42 GMT

Sig. Wave Ht. = 1.5 m
Peak Period = 7.4 s
Peak going towards 241. T
Contour spacing 0.172 m**2/Hz
Peak Energy 2.483 m**2/Hz

Figure 6.13 (Cont'd)

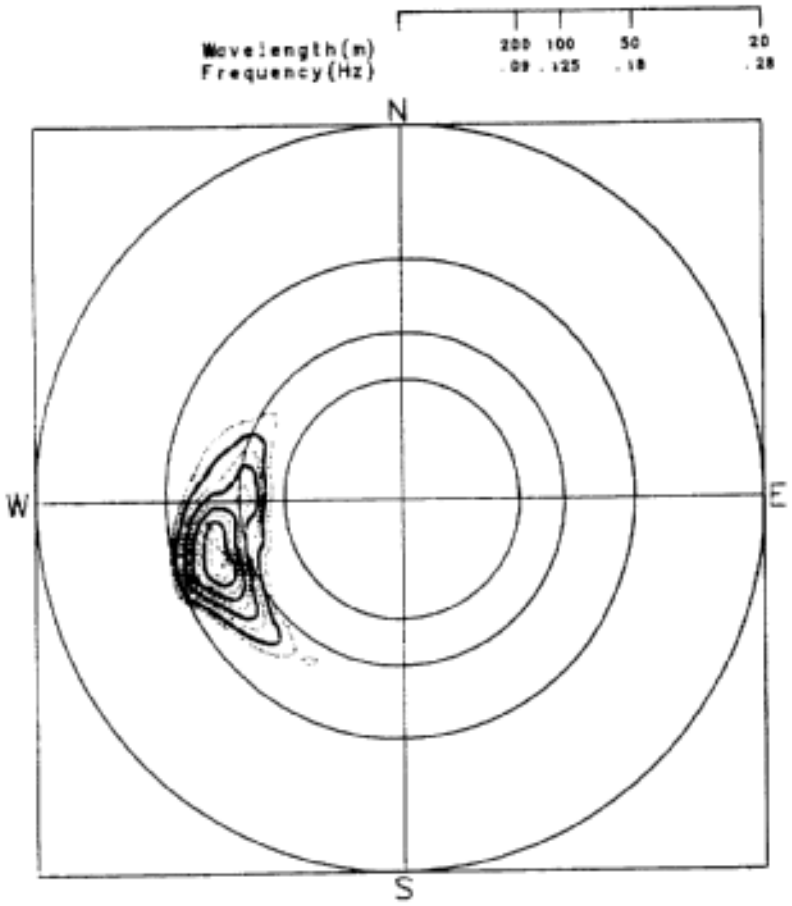

ICE MOTION PACKAGE

25-1C

25-03-87 20:46:00 GMT

Sig. Wave Ht. = 1.6 m

Peak Period = 9.1 s

Peak going towards 251. T

Contour spacing 0.203 m**2/Hz

Peak Energy 2.923 m**2/Hz

Figure 6.13 (Cont'd)

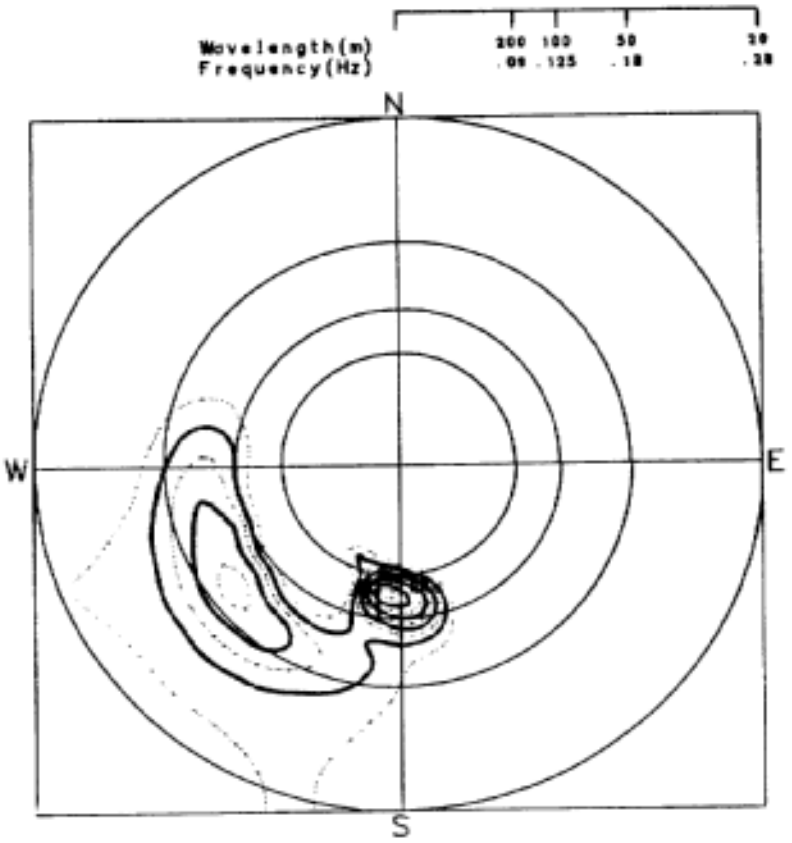

ODGP HINDCAST

Grid point : 3741.

8703.2514. GMT

Sig. Wave Ht. = 1.9 m
Peak Period = 6.3 s
Peak going towards 188. T
Contour spacing 0.046 m**2/Hz
Peak Energy 0.662 m**2/Hz

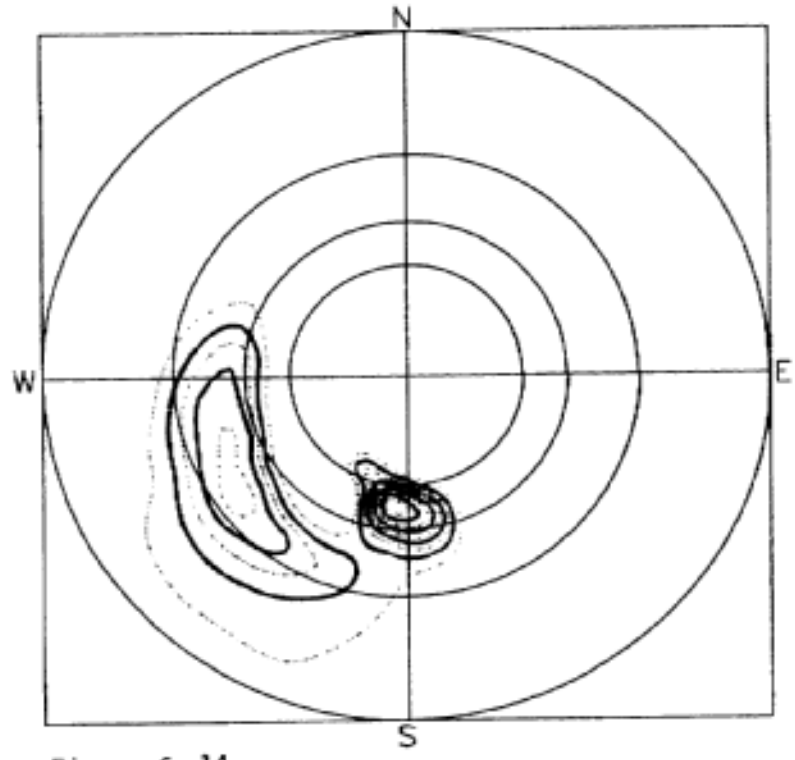

ODGP HINDCAST

Grid point : 3741.

8703.2516. GMT

Sig. Wave Ht. = 1.9 m
Peak Period = 6.3 s
Peak going towards 188. T
Contour spacing 0.045 m**2/Hz
Peak Energy 0.651 m**2/Hz

Figure 6. 14

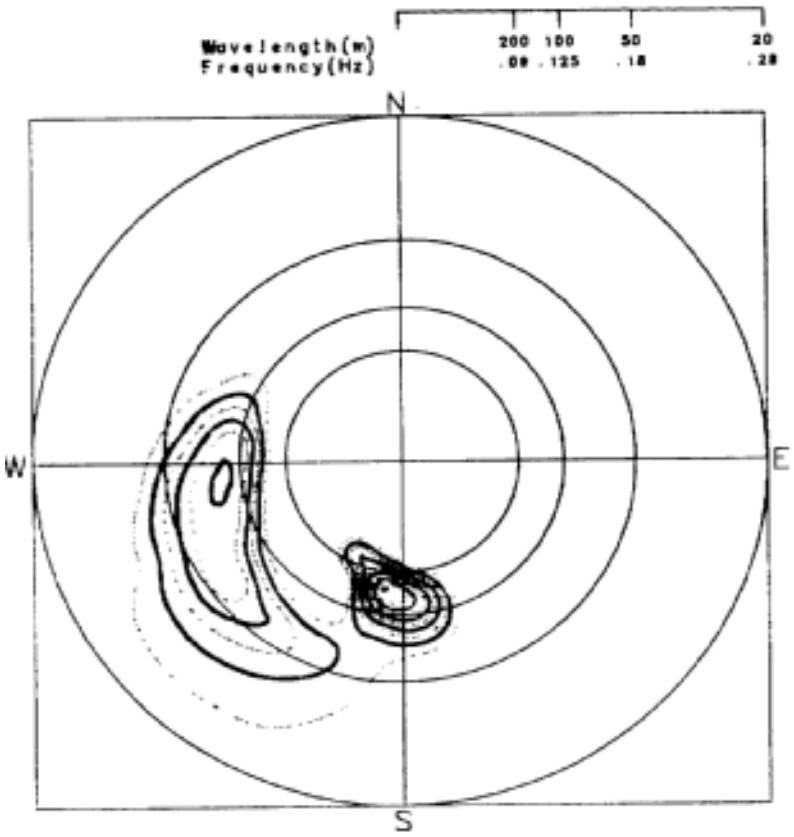

ODGP HINDCAST

Grid point : 3741.

8703.2518. GMT

Sig. Wave Ht. = 1.9 m

Peak Period = 6.3 s

Peak going towards 188. T

Contour spacing 0.043 m**2/Hz

Peak Energy 0.623 m**2/Hz

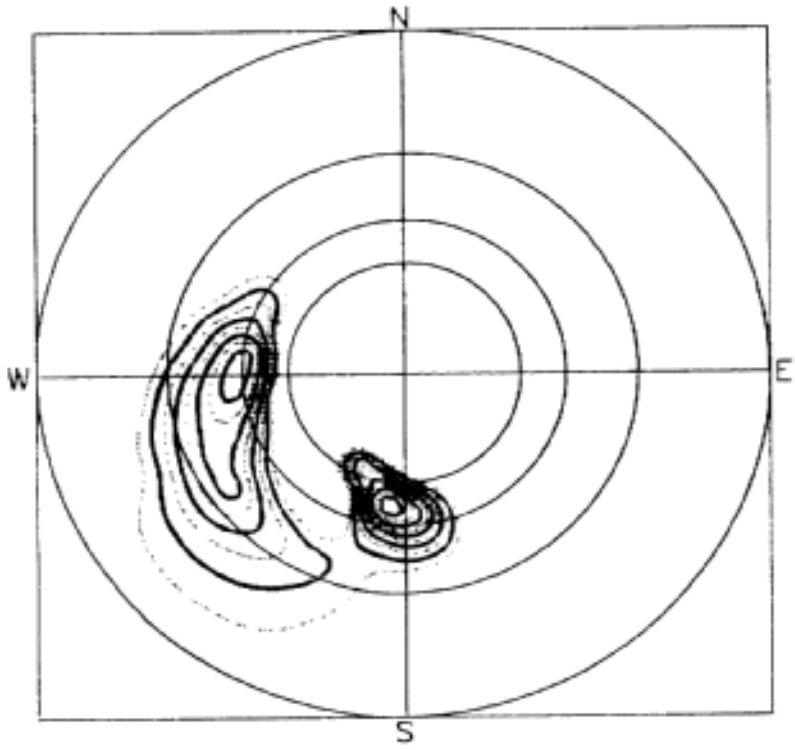

ODGP HINDCAST

Grid point : 3741.

8703.2520. GMT

Sig Wave Ht. = 1.9 m

Peak Period = 8.6 s

Peak going towards 188. T

Contour spacing 0.040 m**2/Hz

Peak Energy 0.582 m**2/Hz

Figure 6.14 (cont'd)

During the next time set, 1544z, the ice package, 25–1C, again shows two peaks; the larger peak with a period of ~6.5 seconds, is moving towards the north–northeast, and the smaller peak at ~9 seconds is moving towards the south. A comparison of this motion to the ODGP wave spectra shows that the smaller peak in the ice package motion has the same frequency and direction as the large peak in the ODGP spectra. The large peak in the ice package motion does not correspond to the ODGP spectra, although the position of the motion indicates that wave reflections may be occurring.

At 1604z, the ice package motion showed one peak at ~7 seconds towards the north–north–east, approximately 180° from the ODGP spectra. At 1624z, the peak shifted frequency to ~6.5 seconds, and a small one at ~9 seconds developed to the south–south–west. This smaller peak corresponds well to the swell component of the ODGP spectra.

At 1653z, the analysis of 25–1C produced two peaks; a larger peak at ~6.5 seconds moving towards the north–east, and the smaller peak at ~8.5 seconds moving towards the south–west, 180°, from the larger peak. The direction of the smaller peak coincides with the direction of the smaller peak in the ODGP spectra, and the larger peak corresponds to the position one would expect reflections to occur. At 1713z, the analysis of 25–1C indicates 3 peaks; the two larger peaks at ~9 and ~6 seconds move towards the north–east, and the smaller peak at ~9 seconds moves towards the west–south–west. Again, the smaller peak is moving in the expected direction and the larger peak occurs where one would expect reflections. However, one does not expect the larger peak to be caused by reflections.

At 1733z, the analysis shows two peaks in the ice motion, the larger peak at ~6.5 seconds moving towards the north–east, and the smaller peak at ~9 seconds moving towards the west–south–west. Again , the direction of the smaller peak coincides with the direction of the smaller peak in the ODGP spectra, and the larger peak occurs where one would expect reflections.

At 1753z, the ice package spectra starts to rotate anticlockwise. The larger peak at ~6.5 seconds moves towards the north–north–east, and the smaller peak at ~9 second moves towards the south–west. At 1826z, the larger peak moves towards the north–west, and the smaller peak moves towards the south–east. At 1846z, the larger peak moves slightly but the motion remains towards the north–west. The smaller peak towards the south–east becomes much smaller. At 1912z, the smaller peak disappears, and the larger peak becomes two peaks at and ~6.5 and ~9 seconds towards the west–north–west. Throughout the rotation of the spectrum. the position of the peaks do not correspond to the ODGP spectrum peaks. The reasons of the spectra rotation are unknown. However, there appears to be a correlation to the rotation of the ice

floe, as shown in Figure 6.15 , indicating the possibility of a preferred axis for energy dissipation in the ice floe. Alternatively, a weather system and/or current regime forcing the rotation of the floe will affect the motion of the ice floe as well.

Between 1932 and 2046z, the analysis indicates one energy peak moving towards the west–south–west, with a period of ~6.5 seconds, which corresponds to the higher frequency peak in the ODGP spectra. However, the peak period determined in the non–directional spectra indicates a period of 9.1 seconds. This discrepancy in frequency may be due to the larger angular spread in the lower frequencies. In each plot, the contour intervals was placed at one sixth of the peak energy. Any energies below the minimum level (i.e. less than one sixth of peak energy) are not shown on the plot.

In Figure 6.16 to 6.18 , the directional energy spectra for deployments 25–2B, 25–3B and 25–4B are shown along with the directional spectra of deployment 25–1C during the same time period, Figure 6.16 shows that ”wave” energy is travelling towards the south–west during deployment 25–2B. The 25–1C deployment also shows an energy peak in this direction, but also shows another peak travelling towards the north–east. It is not known whether this second peak is due to wave reflections from the ice edge, to the floe characteristics or to swell energy travelling from the other side of the ice field (i.e. from the south–west).

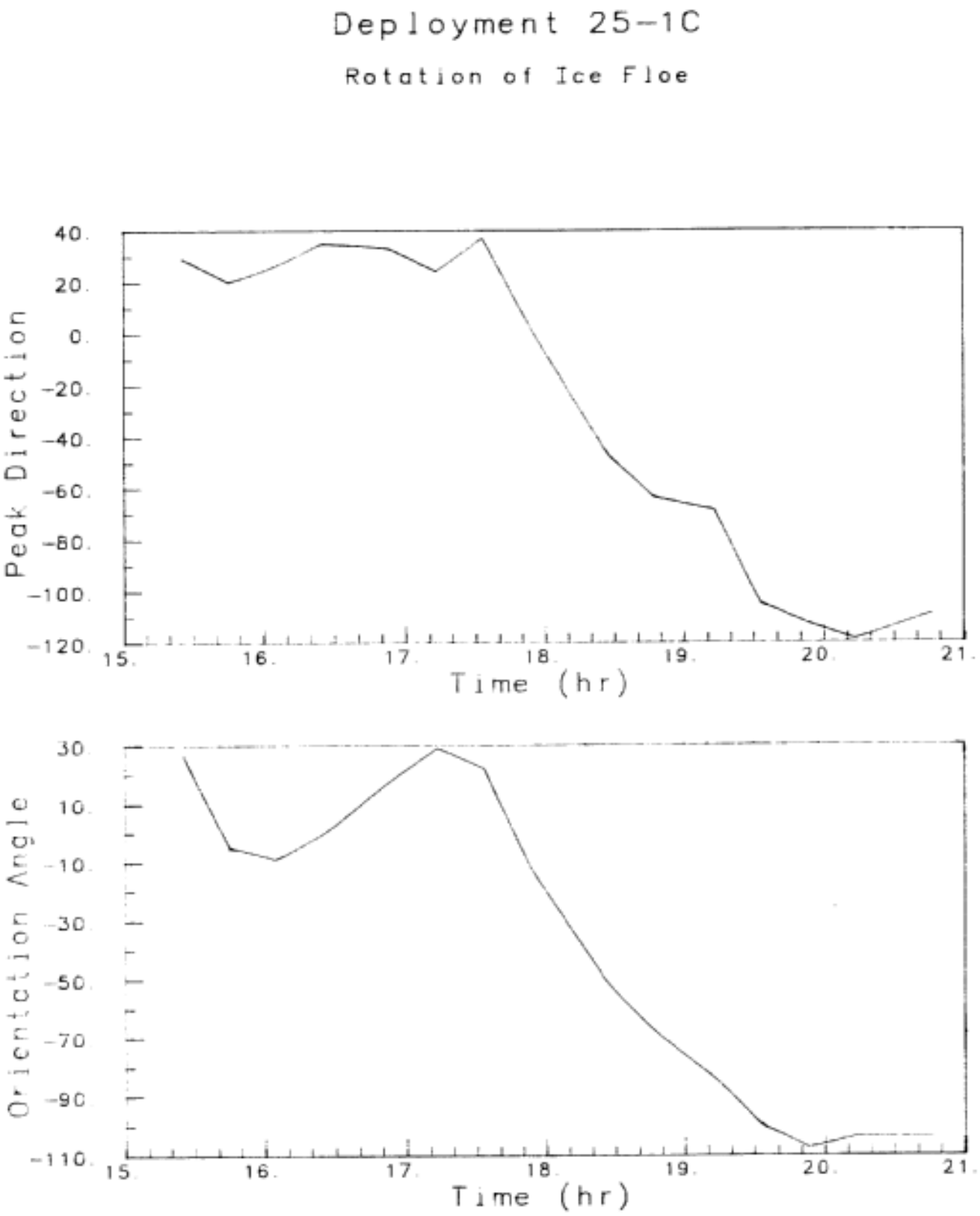

Figure 6.15 Time Series Plot of 25-1C Package Orientation Angle and the Direction of the Peak Energy.

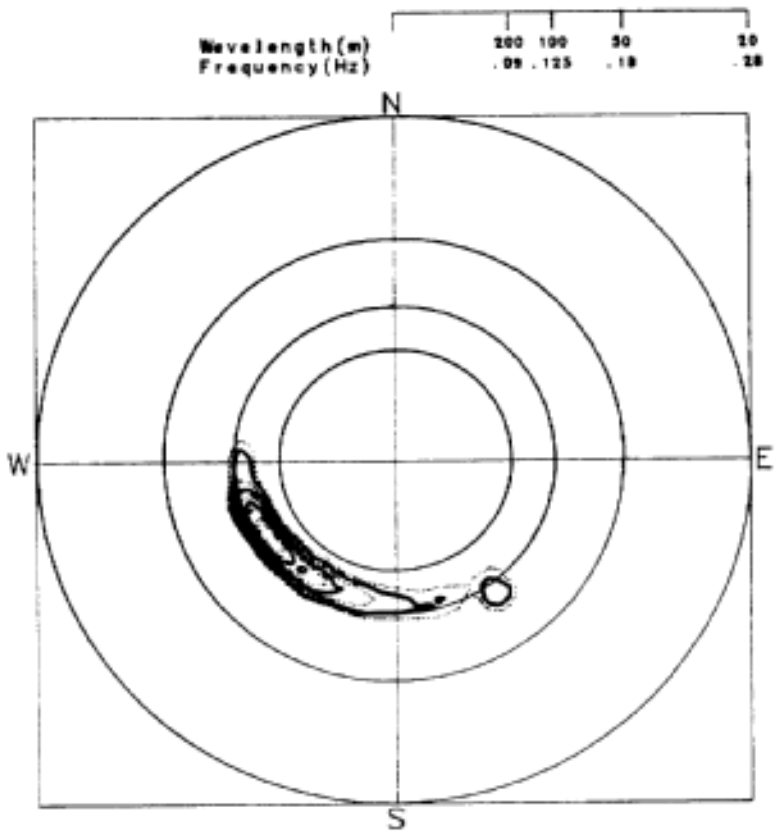

ICE MOTION PACKAGE

25-2B

25-03-87 17:16:29 GMT

Sig. Wave Ht. = 1.0 m
Peak Period = 8.7 s
Peak going towards 239. T
Contour spacing 0.111 m**2/Hz
Peak Energy 1.595 m**2/H

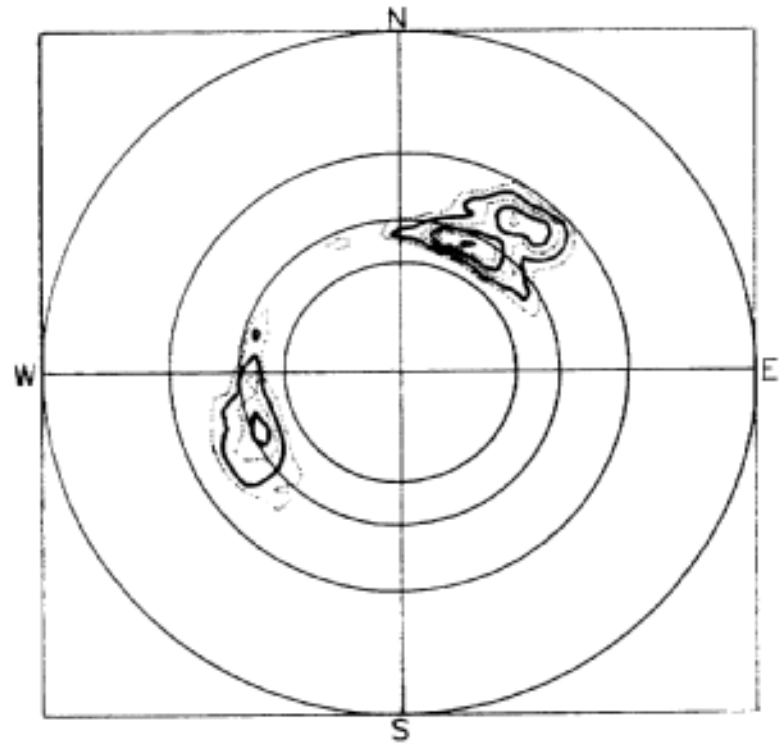

ICE MOTION PACKAGE

25-1C

25-03-87 17:13:12 GMT

Sig. Wave Ht. = 1.6 m
Peak Period = 8.7 s
Peak going towards 24. T
Contour spacing 0.198 m**2/Hz
Peak Energy 2.856 m**2/H

Figure 6.16

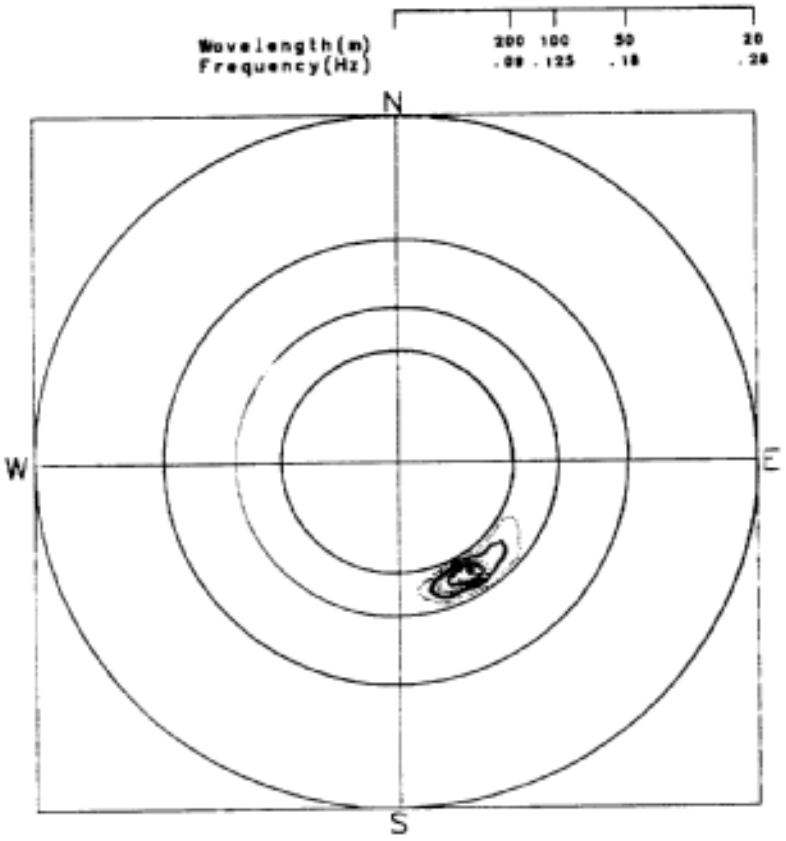

ICE MOTION PACKAGE

25-3B

25-03-87 19:05:15 GMT

Sig. Wave Ht. = 0.6 m
Peak Period = 9.5 s
Peak going towards 147. T
Contour spacing 0.091 m**2/Hz
Peak Energy 1.304 m**2/Hz

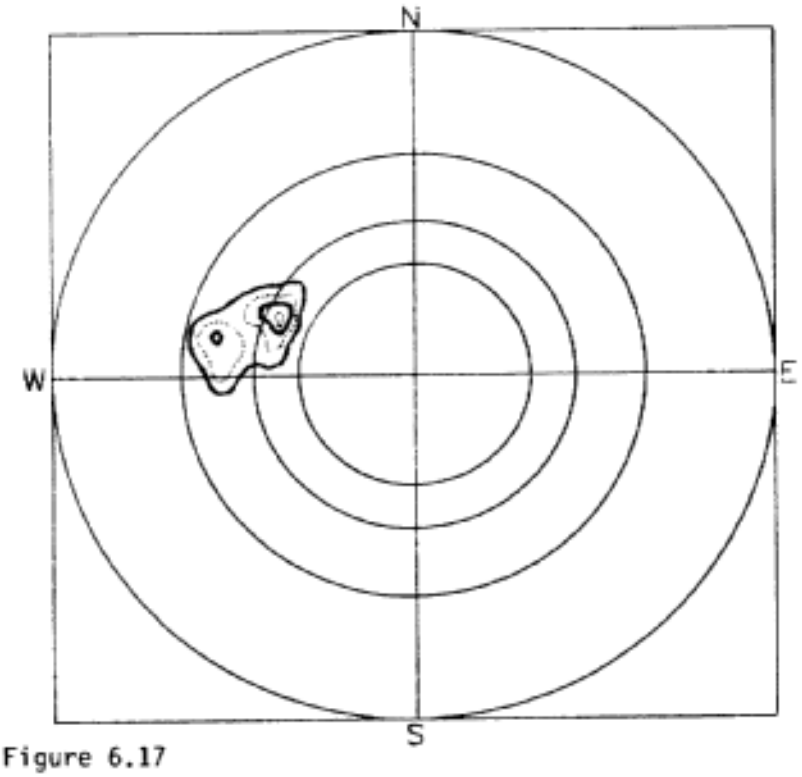

ICE MOTION PACKAGE

25-1C

25-03-87 19:12:40 GMT

Sig. Wave Ht. = 1.7 m
Peak Period = 8.7 s
Peak going towards 291. T
Contour spacing 0.495 m**2/Hz
Peak Energy 7.133 m**2/Hz

Figure 6.17

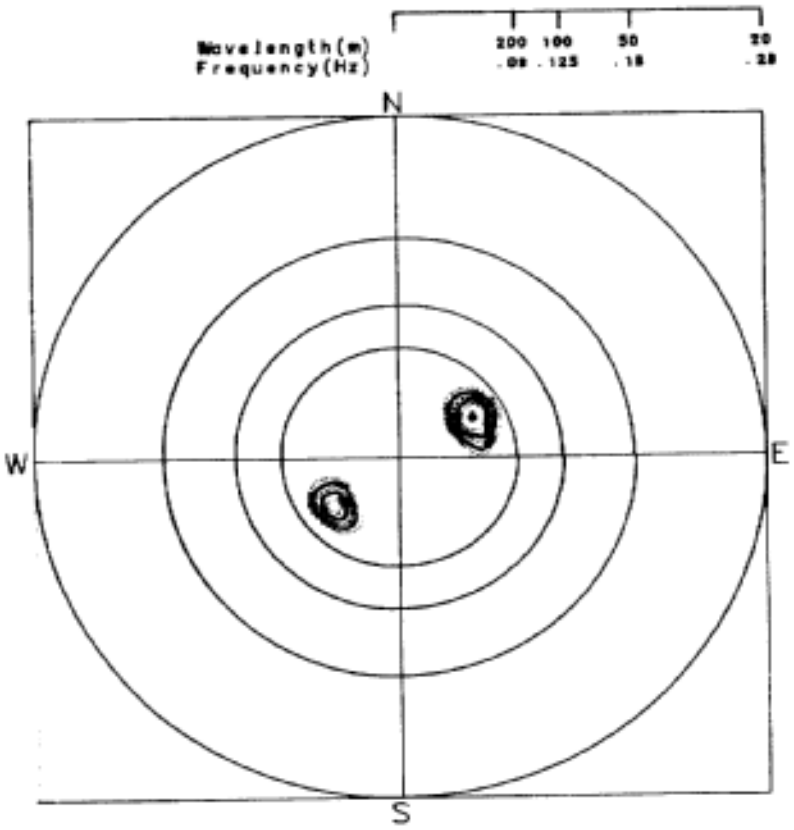

ICE MOTION PACKAGE

25–4B

25-03-87 20:11:39 GMT

Sig. Wave Ht. = 0.3 m
Peak Period = 18.2 s
Peak going towards 236. T
Contour spacing 0.009 m**2/Hz
Peak Energy 0.123 m**2/H

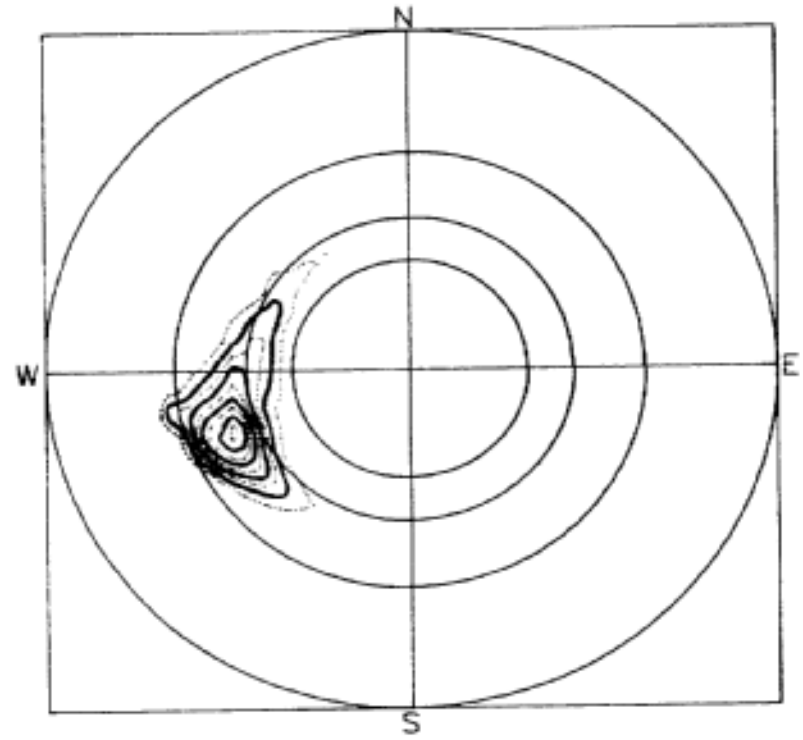

ICE MOTION PACKAGE

25–1C

25-03-87 20:12:42 GMT

Sig. Wave Ht. = 1.5 m
Peak Period = 7.4 s
Peak going towards 241. T
Contour spacing 0.172 m**2/Hz
Peak Energy 2.483 m**2/H

Figure 6.18

The directional wave spectra for deployment 25–3B is shown in Figure 6.17 , along with the spectra obtained during the same period of the 25–1C deployment. The motion of the ice floe during the 25–3B deployment is moving towards the south–east with a period of 9.5 seconds, while the motion of the 25–1C ice floe is moving towards west–northwest with a period of ~8.5 seconds. The reason for the differences in direction is unknown. Perhaps, the same phenomenon seen in the rotation of 25–1C may have affected the 25–3B deployment as well. However, there is no evidence supporting this hypothesis, and perhaps wave refraction in the ice was the cause.

The directional wave spectra for deployment 25–4B is shown in Figure 6.18 along with the spectra obtained from deployment 25–1C. The 25–4B spectra indicates two peaks with an 18.2 second period; one towards the north–east, and one towards the south–west. The 25–1C spectra also indicates a peak towards the south–west. The motion towards the south–west agrees with the ODGP spectra. The change in ”wave” frequency indicates a strong attenuation of the higher frequencies, and perhaps a frequency shift in energy as the waves pass through the ice field.

On March 26, three deployments were made along the ice edge. The directional energy spectra for deployments 26–2C and 26–3B are shown in Figure 6.19 . The results from deployment 26–1B were not included due to problems with the ice package. During the same time period, the directional energy spectra for the ODGP grid point 3741 is provided in Figure 6.20 . A comparison of the two ice package deployments show major differences in the package motions. The 26–2C deployment indicates motion towards the south–west, which agrees with the ODGP spectra, and motion towards the east. The 26–3B deployment indicates motion towards the north. Both packages indicate low frequency motion. The ODGP spectrum indicates two peaks; one peak at ~12 seconds to the south–southwest, and the other at ~10 seconds, towards the west. The motion in deployment 26–2C indicates a reflection of the ODGP spectral peak towards the west, and a refraction of the wave energy towards the south–west. The motion in deployment 26–3B can not be explained. The peak energy seems too high when compared with the ODGP prediction.

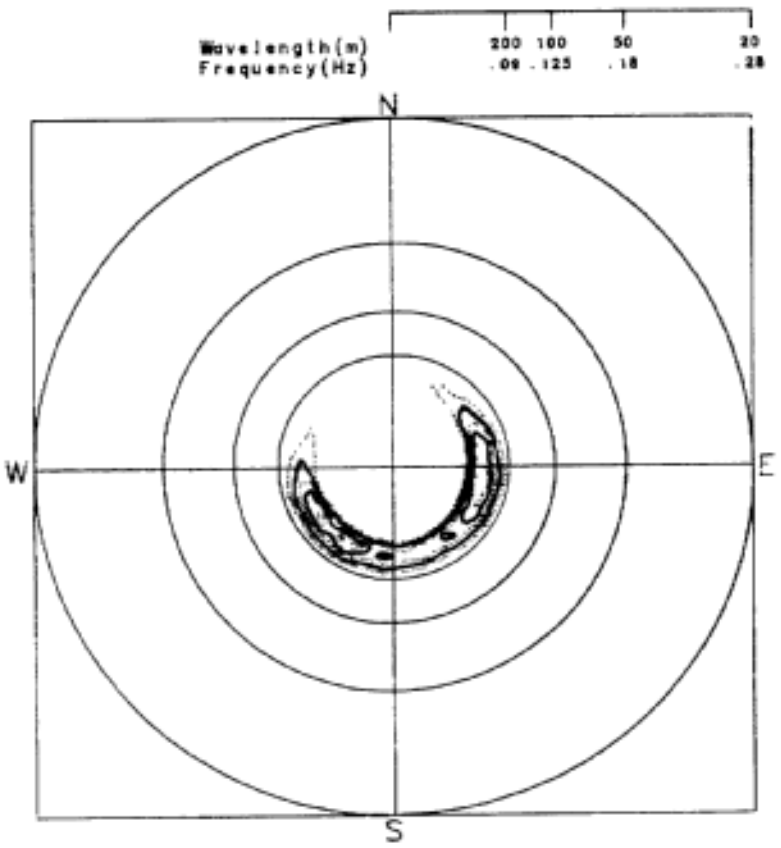

ICE MOTION PACKAGE

26-2C

26-03-87 13:59:32 GMT

Sig. Wave Ht. = 2.7 m
Peak Period = 14.3 s
Peak going towards 208. T
Contour spacing 0.653 m**2/Hz
Peak Energy 9.398 m**2/Hz

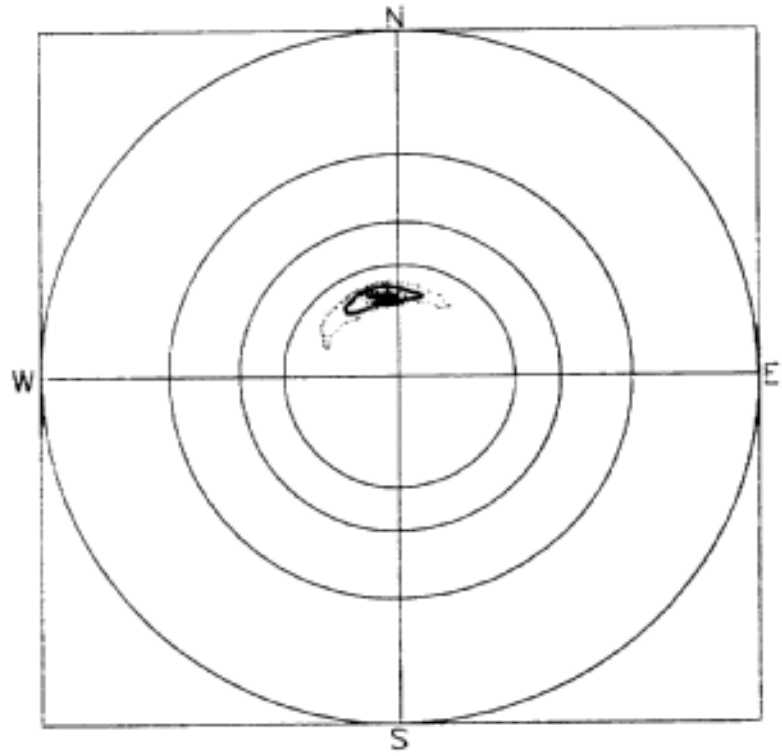

ICE MOTION PACKAGE

26-3B

26-03-87 16:23:28 GMT

Sig. Wave Ht. = 2.2 m
Peak Period = 15.4 s
Peak going towards 342. T
Contour spacing 0.972 m**2/Hz
Peak Energy 14.003 m**2/Hz

Figure 6.19

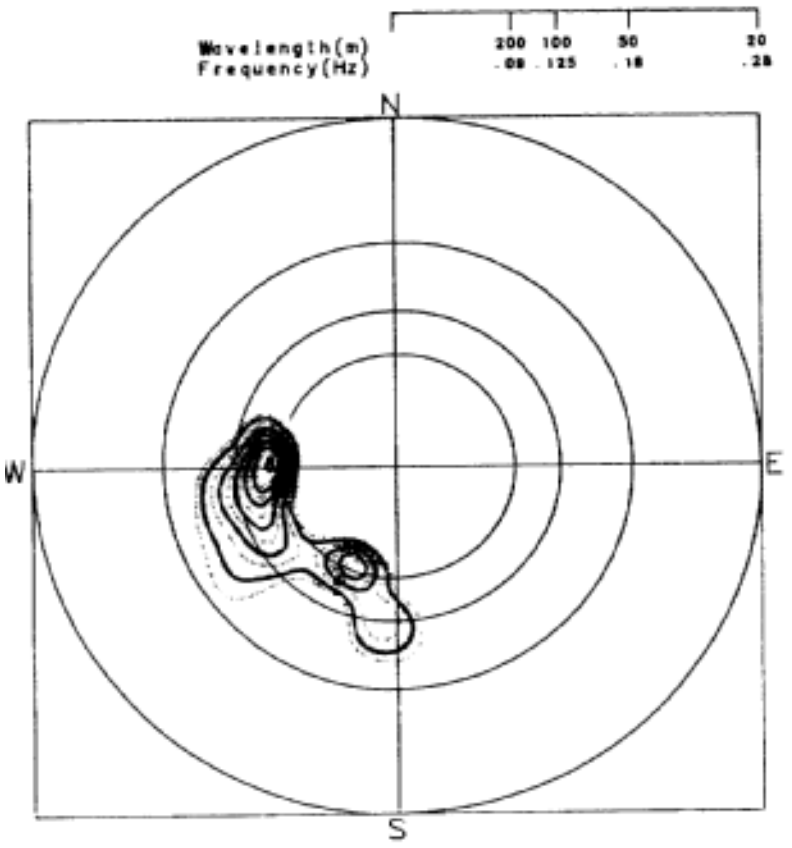

ODGP HINDCAST

Grid point : 3741.

8703.2614. GMT

Sig. Wave Ht. = 2.1 m

Peak Period = 9.7 s

Peak going towards 278. T

Contour spacing 0.073 m**2/Hz

Peak Energy 1.052 m**2/Hz

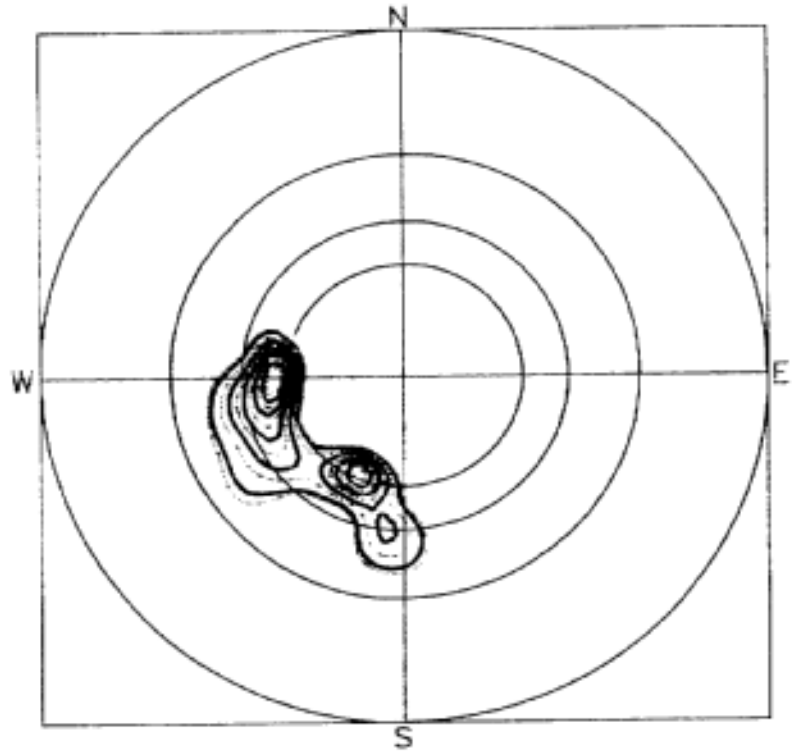

ODGP HINDCAST

Grid point : 3741.

8703.2616. GMT

Sig. Wave Ht. = 2.1 m

Peak Period = 9.7 s

Peak going towards 263. T

Contour spacing 0.066 m**2/Hz

Peak Energy 0.952 m**2/Hz

Figure 6.20

6.3 WAVE PENETRATION AND ATTENUATION IN MIZ

The initial analysis of the ice motion packages involved plotting time series of the ice package motion, as well as 1– and 2– dimensional spectral plots. These plots clearly show that waves can penetrate the MIZ and propagate through the ice. However, it is uncertain as to how the ice interacts with the propagating waves. In previous studies, Wadhams et al. (1986), Wadhams (1978), attenuation of the waves in the ice pack was observed and appeared to be dependent on the wavelength.

From Wadhams (1986), the wave energy at a distance x in the ice zone can be approximated as:

$E(x) = E_o \exp(x\lambda)$

where E_o is the wave energy outside the MIZ, and λ is the attenuation coefficient. The attenuation coefficient, or rate of attenuation, is dependent on the frequency/wavelength of the incoming wave.

In this study, several ice packages were deployed in three separate experiments. In the first experiment carried out on March 22, an ice motion package was deployed just inside the MIZ, and a waverider buoy was deployed 500 metres outside the MIZ. In the second experiment carried out on March 25, the ice motion packages were deployed at various distance in the ice pack. In the third experiment carried out on March 26, ice packages were deployed on the ice edge while radar images were taken of the area.

The results from the March 22 experiment indicate that the 1–dimensional spectral plots from the ice motion package and the waverider buoy are very similar (Figure 6.4). The waverider results indicate a significant wave height of 2.3 metres and a 9.2 second peak period, while the ice package a 1.9 metre significant wave height and a 9,1 second peak period. These results indicate that either the wave was attenuated by the ice. No 2– dimensional plots of the waverider measurements were available, so directional wave plots could not be used for a comparison.

The results from the March 25 experiment provide information on the attenuation of waves in the ice. At the start of the experiment, an ice package was deployed on an ice floe at the edge of the MIZ and left there for the duration of the experiment (deployment 25–1C). Then, a second ice package was deployed at distances of approximately 1, 2, and 4 km into the ice pack (deployments 25–2B, 25–3B, 25–4B). In Figure 6.8 , the 1– dimensional spectra from the 4 ice package deployments were plotted on the same plot. The plot illustrates that the wave energy is attenuated by the ice, with the energy in the low frequencies being relatively unaffected.

Although the ice package measurements were collected during different time periods, the measurements can still be used to verify the above

equation since the sea state did not change drastically during the course of the experiment. The rate of attenuation (or the attenuation coefficient λ) is calculated by plotting the ratio of the wave energies ($E(x)/E_o$) as a function of the distance into the ice on a logarithmic–linear plot. The initial energy Ei of the waves propagating into the ice is unknown. However, the measurements from deployment 25–1C can be used to approximate the wave energy of waves entering the MIZ, as shown by the March 22 experiment. The slope of the plot is the attenuation coefficient. An example calculation of the attenuation coefficient (at frequency = 0.1 Hz) is shown in Figure 6.21 . A comparison of the attenuation coefficient at 0.10 Hz was compared to the value obtained by Wadhams et al (1986), and were found to be the same.

The attenuation coefficient was calculated for several other frequencies. The results of these calculations are shown in Figure 6.22 . The plot shows how the attenuation of the wave energy tends to decrease as the frequency decreases, and the period increases, Furthermore, a logarithmic relationship appears to exist between the attenuation rate and the wave frequency.

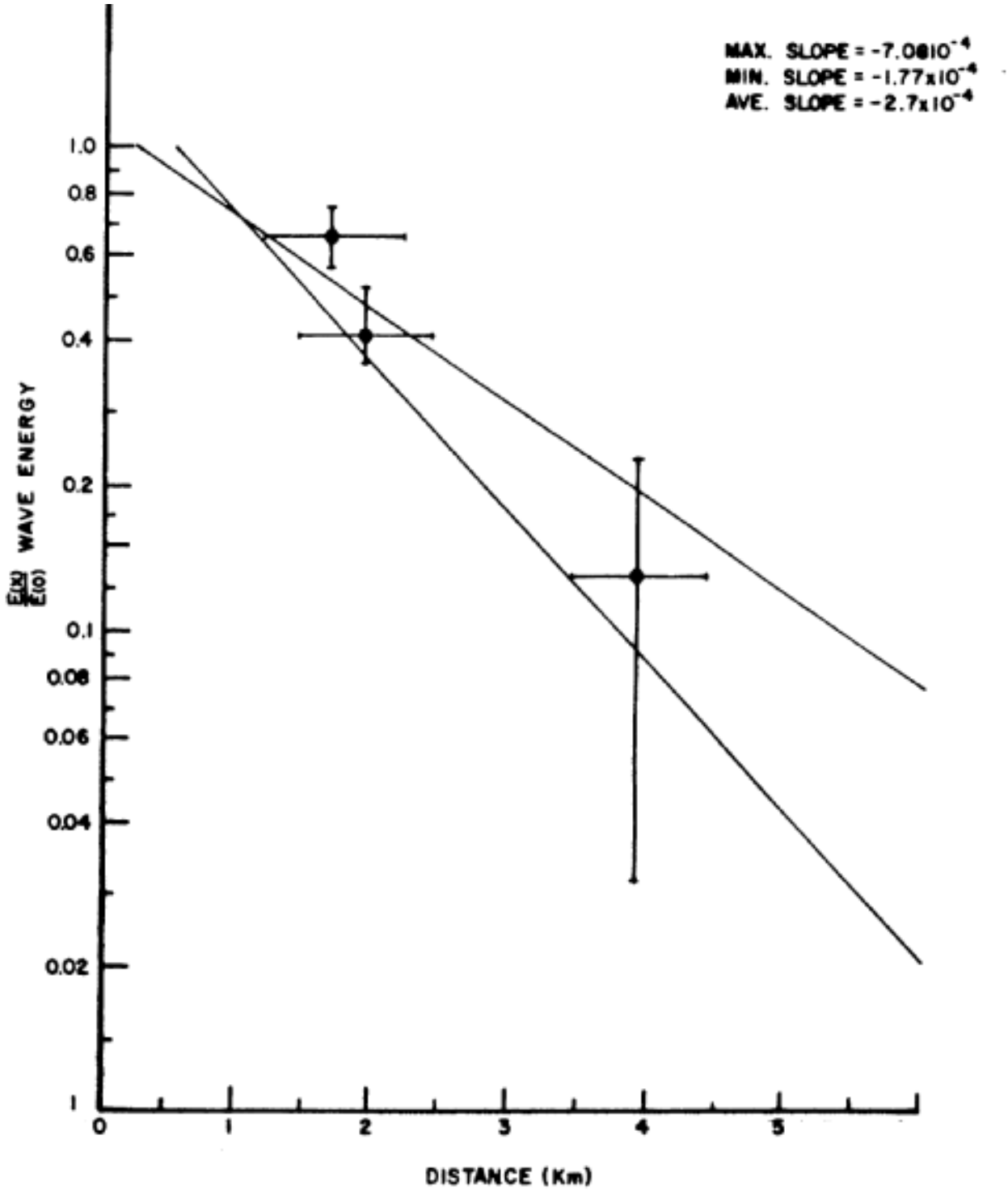

FIGURE 6.21

ATTENUATION OF WAVE ENERGY VERSUS DISTANCE FROM ICE EDGE

FREQUENCY f=0.10 Hz

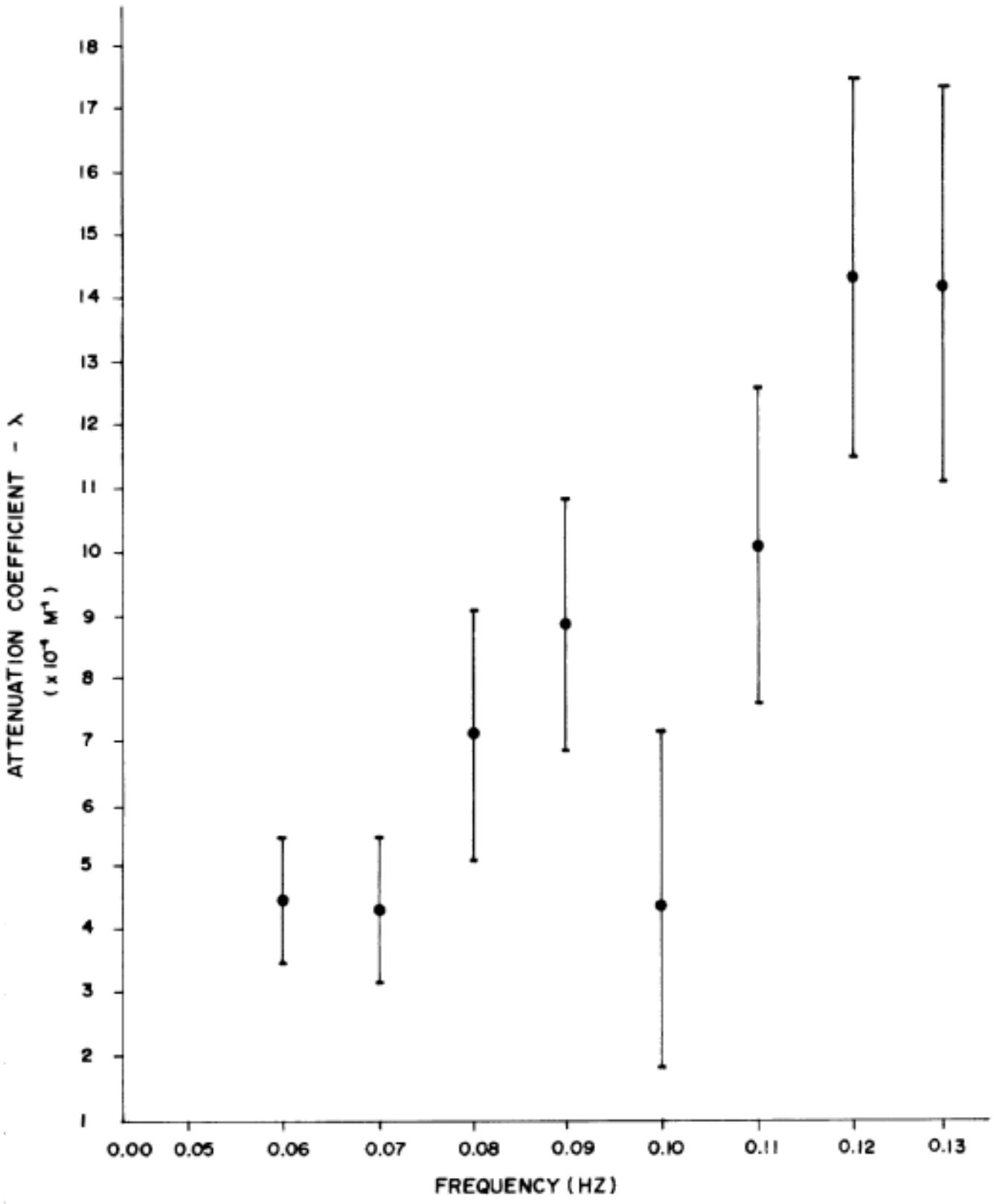

FIGURE 6.22 ATTENUATION COEFFICIENT vs. WAVE FREQUENCY

6.4 DISCUSSION

As seen in Figures 6.11 to 6.20 , the directional energy spectra inside the ice zone can be obtained for the ice motion packages. When calculating the directional spectra, the ice motion package was treated as pitch–roll waverider buoy, and that the motion of the ice floe would closely follow the wave motion. However, the results from this analysis do not always reflect the expected wave conditions in the ice field. In many directional spectral plots, the ice floe motion occurs in a direction where one would expect reflections to be seen. Wave reflection from an ice floe will generally occur when the ice floe has sufficient dimensions such as thickness and diameter, and when the frequency of the incident waves produce wavelengths shorter than the floe dimensions. With these factors in mind, one would expect to see some reflections. However, one must use caution in this interpretation. In many situations, the only motion seen in the plots is where one would expect reflections. In these situations, the size of the floe would not inhibit the transmission of wave energy in the wave direction, and one would expect to see motion in the wave direction.

Another assumption made in this analysis was that the ice floe was free to move, and that it was stationery. From the supplied data, it was observed that ice floe drifted during a deployment, and that the ice floe tended to rotate with time. These movements are small relative to the twenty minute period used in the spectral analysis. However, no attempt was made to observe the interaction of the ice floe with other floes. During the deployment, the ice floe may have been subjected to ice slamming, and may have been wedged between adjacent floes for short periods of time. These factors could greatly affect the analysis results.

Another assumption made during the analysis was that the ice motion package can be used in the same manner as a waverider. Although the heave component has been tested, no attempt has been made to test the directional results of the ice motion package in conditions measured by a directional waverider buoy. More tests are needed to determine whether the ice motion package can accurately provide directional spectral information, and whether the ice floe will alter the directional motion measured by the ice package. The dimension of the ice floe is potentially a very important factor in the motion seen by the ice package. Ideally, the ice motion package should be placed in the center of a ice floe with a uniform thickness, and circular in shape. From the oblique photographs of the ice floes used in the deployments, the ice package was not always placed near the center, and the dimensions of some floes were very irregular. These factors could greatly affect the motion measured by the ice package.

Another factor influencing the analysis results is the method used to convert the co– and quadrature spectra values to directional plots. As shown earlier in Figure 6.10 , each method produces different results. At this time, no method is perfect, but some methods provide better results than others. In this study, the maximum likelihood method was chosen even though problems were known to exist with the method.

In this study, the ice motion directional spectral plots appear to bring up more questions than answers. In one experiment, it was shown that the non–directional wave spectra from the ice package compares well with that measured from a waverider buoy. However, the directional spectra plots appear to be inconsistent with plots given by the ODGP model. These inconsistencies are not fully understood, and more work must be done to describe the ice floe motions. In future studies, it is suggested that a directional waverider buy be placed near an ice motion package. Comparisons between the two spectra will provide information about the effects of an ice floe on the motion seen by the ice motion package. In this study, no such measurements were taken, so the wave spectra from the ODGP model

formed the basis of the directional spectral comparisons Although the ODGP model produces accurate results, it cannot provide the same level of information given by a directional waverider buoy.

The main purpose of this study was to study the wave–ice interaction observed in the marginal ice zone. In this study, we have identified several problems which need to be studies further. These problems should be dealt with to get the most useful information available during the next LIMEX study in 1989.

7.0 SUMMARY AND CONCLUSIONS

The LIMEX ’87 Project showed that ocean waves play an important part in generating the type of ice which makes up the marginal ice zone. This conclusion is supported by ice observations and the wave induced ice motions collected from the ’CSS Baffin’. The waves break any large ice floes entering the marginal ice zone into small floes and ice cakes. The mean floe size measured along the ice edge was 3.3 m with standard deviation 2.7 m. Ice deformation within the cover acts to absorb the incident wave energy. There are two classes of deformations operating, (1) relative movements of adjacent floes; and (2) failure of ice material. The ice fails by two different modes. Ice crushing caused by the impact of adjacent floes, and splitting resulting from bending moments on the floes.

Waves penetrating the ice cover cause the ice floes to jostled around and strike each other. Sea ice is a relatively weak material and some ice breaks at the contact area during each impact. Ice crushing makes up the larger proportion of the breaking actions. As a result, it produces large volume of finely ground brash.

Several factors are operating and dictate how effectively the marginal ice zone absorbs the incident ocean wave energy. The list below considers five of these factors.

1. Ice Strength: The relatively weak ice of the marginal ice zone fails rapidly producing larger volumes of ground brash. The ’in situ’ pressuremeter trials showed the floe ice having a crushing strength of 0.5 MPa. A low strength compared with the 2 to 3 MPa for pressuremeter measurements on sea ice in the Arctic. The crushed ice lubricates subsequent relative motion between adjacent floes. In addition, the crushed ice between the floes cushions subsequent impacts and slows the ice failure rate.

Therefore, an ice cover losses its ability to absorb wave energy as the failure proceeds. Hence, the failure zone radiates away from the ice edge; and the waves penetrate progressively deeper into the ice cover.

2. Ice Jamming: When a coastline pins a boundary of the cover the lateral stress on the ice forces the individual floes to edge–to–edge contact. The compacting of the floes increased the number of edge–to–edge impacts. The horizontal load extrudes crushed ice from the interstitial gaps. Hence an ice cover held in compression maintains its ability to absorb wave energy. Although more crushed ice generates near the ice edge, the failure zone radiates away from the edge slowly.

3. Temperature: Temperature is an important variable in ice behaviour to influences strength, freezing and melting. The

surrounding air and water temperatures will dictate if heat transfers to or from the ice cover. When the heat transfers from the ground brash, it will begin to refreeze. Relative motion between adjacent floes and within the brash will inhibit the ground ice from cementing into solid floes. Once a block of ice achieves enough strength to resist relative motion, it will continue to freeze and become a floe or ice cake within the ice cover. During LIMEX ’87, the temperature seldom dropped below 0 degree C. and there was no opportunity to observe the refreezing processes. If the impinging ocean wave field abates during a freezing period, the whole zone will refreeze into large floes. Such floes are composed of particular ice and readily break into their constituent smaller floes when exposed to another incident wave field.

4. Floe Movements: The relative motion between the adjacent floes, the jostling and the rotations absorb a portion of the propagating ocean wave energy. This type of action packs the ice floes tightly together breaking any arches which may have formed within the cover.

5. Viscous Flow: The crushed ice matrix filling the interstitial gaps between the floes is pumped and squeezed by the jostling floes. Some ice gets pushed up to form the small ridges characteristic of pack ice floes. More gets pushed down and lies beneath the solid ice, Jordan’s (1988) recent research on ice failure mechanism speculates that the viscous flow of crushed ice produced at the failure interface consumes a significant portion of the energy required in ice breaking. The crushed ice generated by wave action is a similar material. The ground brash is saturated with water to the water line. In addition, the capillary action holds some water to the ice particles pushed above freeboard. The viscous flow of the ground ice material will also dissipate a portion of the ocean wave energy.

This group of independent factors act to dissipate the incoming ocean wave energy. All the factors discussed involve ice mechanics; the stress level, the relative motion and the failure of the ice cover. All these factors are important in predicting how pack ice conditions will influence operations on offshore structures during winter conditions. The LIMEX ’87 observations indicate the floes of the marginal ice zone is continually fractured and crushed. This action produces an ice cover which contains a significant portion of ground brash ice filling in between the solid floes.

Storm conditions which produce the large driving forces to impart large ice loads will also break the ice cover into small floes. An ice cover of small floes will be expected to flow past a floating or fixed structure, where the ice cover acts mechanically to absorb the incoming wave energy. Hence, the ice cover dissipates wave energy propagating into the ice pack.

The present study has shown that the ice motion package can provide an estimation of the wve spectra inside the MIZ. However, care must be taken when using the 6 spectra (C_{11}, C_{22}, C_{33}, C_{23}, Q_{12}, Q_{13}) to estimate the 2–D wave spectra E (F,ϕ).

It must be emphasized that the standard measurement of wave elevation and slopes normally utilizes a wave buoy whose motion response characteristics are known over the range of ocean wave frequencies. In LIMEX ’87, motion measurements were made on ice floes within the pack ice. The motion characteristics of the instrumented ice floes are not known, and hence, in general, it is not possible to state how the measured heave, pitch and roll relate to the corresponding wave elevation and slopes, Furthermore, the dispersion relationship linking wave frequency to wavelength is modified by the presence of pack ice.

It is likely that for the predominantly long wavelength waves which penetrate the pack ice, moderately sized (< 10m dia.) ice floes follow the wave surface reasonably closely. Thus, the measured floe motions may be cautiously treated as being equivalent to the desired wave measurements.

Also, for uniform ice, the wave dispersion relationship is known. The derivation of this relationship requires knowledge of the boundary condition at the ice/water interface, a condition which may readily be specified assuming a uniform ice cover is known material properties. However, in partial ice cover, this boundary condition varies locally from open water to ice covered conditions. It is not known how this affects the wave dispersion relationship or indeed if this relationship can even be determined except in some area–averaged sense.

Solution of these problems of unknown floe motion characteristics and wave dispersion relationship would require considerable additional effort, well beyond the present scope of work. Since the heave measurements are least affected, nondirectional wave spectra obtained from ice floe motions are probably valid without correction. These yielded information on the attenuation of the waves by the ice cover which agreed with Wadhams et al, (2986). The validity of any directional wave spectra obtained using ice floe motion measurements may have to be checked by comparing the directional spreading seen inside and outside of the pack ice on occasions where open water spectra are available. Unfortunately this information was not available from LIMEX ’87 experiment and it is hoped to be overcome in LIMEX 189 project.

7.1 FUTURE WORK

The validation of models for the breaking of ice by waves and the dissipation of wave energy in the ice cover and modelling of waves in ice should be one of the main objectives for LIMEX ’89.

1. The collection of ice motion records for longer periods will provide a better picture of how the ocean wave energy dissipates as a function of time. Motion records should be collected simultaneously by a group of sensor packages. The measurement pattern should give ice motions a series of positions into the ice cover relative to the ice edge. The motion experiments will be planned to observe the wave attenuation. The experiments should investigate wave dissipation's dependence on ice failure rate, heat transfer with the air and water, and the wind and ocean driving forces.

The study requires a multi–variate approach to design the experiment and analyze the collected data. The experimenters have little control on the range the independent variables will take. The objective must be to collect as much data as possible over as varied a set of conditions as possible, For example, it may be desirable to collect a motion data set at night to take advantage of lower nighttime air temperatures, Variance methods will be used during data analysis. The statistical techniques will be able to distinguish the contributions of the different factors like ice properties, ice failure, and driving forces.

A new version of the ice motion package is being designed. The new design addresses some of the operational difficulties experienced during LIMEX '87. The new unit will employ solid state mass storage and will have a lower power requirement. The package may be tracked with an ARGOS transmitter. Hence it will be practical to deploy the package for longer periods of data collection. With the package marked by a beacon, the supporting ship can move away and conduct other tasks. It would return later to recover the instruments and transfer the collected data. The package can be fitted to collect for up to 100 hours. The memory modules would be expensive for long term data collections.

2. The analysis will involve the calculation of energy consumed by ice movements and ice failure. These calculations will require a complete data set on ice thickness, ice properties, and ice failure modes. The energy consumed by the failure will be balanced against the energy dissipated by the ocean waves. Air and water temperature will be required. The temperature distribution describes the head flow and determines if the new ice is freezing or if the ice is melting.

3. Some small scale experiments are needed to observe the active failure mode at the floe perimeters. Results from these tests will be valuable in understanding the way the ice behaves when the ocean wave field forces the ice floes into motion. Small scale results are not likely to provide reliable estimates of energy consumption or rate of production of crushed ice.

4. The average energy dissipation rates are better tracked from larger scale measurements. Some of the required information can be

interpreted from imagery of the ice cover at the different ice motion stations. A detailed description of the ice conditions could be recorded with a helicopter aerial video imagery programme.

It should be possible to use ice imagery to determine ice crushing and ice breaking rates. SAR imagery could provide the data to estimate similar parameters on a much larger scale. The shipboard and aerial imagery should aim to collect the change of ice conditions with time. A camera station on the ship could make a time series of ice observations, when the ship remains at one location for an extended period. The deploying and recovering of the motion packages will provide an opportunity to repeat coverage for a number of fixed stations within the ice field. It will be important to collect coverage which will show the progressive failure of the solid ice floes. A time series of floes spacings collected for a group of ice floes could given an alternate method to make ice failure measurements. Such measurement would be valuable to ground truth ice deterioration interpreted from the ice imagery.

5. The development of new interpretation methods of efficiently and accurately extract ice failure estimates from ice imagery should be a priority. The image analyzer at Bedford Institute of Oceanography will provide an important facility to tackle this component of the research.

6. Further extensive research work is required to adequately model wave–ice interaction which includes wave generation in the ice margin, wave propagation into the MIZ, wave reflection, attenuation and refraction in the ice field, etc. In order to attain this goal, an extensive field program must be designed to collect directional wave data in the open water as close as practically possible from the ice edge and inside the ice edge in the open water pools in the MIZ. These measurements will complement the ice–motion package measurements described in item (1) above.

8.0 REFERENCES

Cardone, V.J. (1969). Specification of the wind distribution in the marine boundary layer for wave forecasting. Geophysical Science Laboratory, New York University. Report TR–69–1. Available from NTIS AD#702–490, New York, N.Y.

Cardone, V.J., W.J. Pierson, and E.G. Ward, (1976). Hindcasting the directional spectrum of hurricane generated waves. Journal of Petroleum Technology 28: 385–394.

Cardone, V. (1980). The Bering Sea Storm Specification Study. Proprietary Report to Exxon Production Resources.

Longuet–Higgins, M.S., D.E. Cartwright and N.D. Smith, (1963). Observations of the directional spectrum of sea waves using the motions of a floating buoy. Ocean Wave Spectra, Prentice–Hall, 111–136.

Lygre, Asle and Harald E. Krogstad, (1986). Maximum entropy estimation of the directional distribution in ocean wave spectra, Journal of Physical Oceanography, 16, 2052–2060.

MacLaren Plansearch Limited (1985). Evaluation the Spectral Ocean Wave Model (SOWM) for Supporting Real–Time Wave Forecasting in the Canadian East Coast Offshore. Report submitted to the Atmospheric Environment Service, January 1985.

Masson, D. and P. LeBlond (1986), Wave growth in scattered sea ice. Proceedings Intel. Workshop on Wave Hindcasting and Forecasting. Sept. 23–26, Halifax, N. S.

Oltman–Shay, Joan, and R.T. Guzo, (1984). A data adaptive ocean wave directional–spectrum estimator for pitch and roll type measurements. Journal of Physical Oceanography, 14, 1800–1810.

Pierson, W.J., L.J. Tick, and L. Baer, (1966). Computer based procedures for preparing global wave forecasts and wind field analyses capable of using wave data obtained by a space craft. Sixth Naval Hydrodynamics Symposium, ACR–136, Office of Naval Research, Department of the Navy, Washington, D.C., 499–532.

Reece, A.M., and V.J. Cardone, (1982). Test of wave hindcast model results against measurements during four different meteorological systems. Fourteenth Annual Offshore Technology Conference, Houston, TX, May 1982. OTC #4323.

Robin, C.D. (1963). Ocean waves in pack ice. The Polar Record, Vol. 11, No. 72. Jan. 63.

Squire, V.A. and S.C. Moore (1980). Direct measurement of the attenuation of ocean waves by pack ice. Nature, 283, 365–368.

Taylor, J. (1987). Calculation of Directional Wave Spectrum, Paper presented at Oceans ’87, Halifax, N. S., Sept. 28–Oct, 1, 1987.

Wadhams, P. (1975). Airborne laser profiling of swell in an open ice field. J. Geophys., 80, 4520–4528.

Wadhams, P. (1978). Wave decay in the marginal ice zone measured from a submarine. Deep Sea Research, 25, 23–40.

Wadhams, P. A mechanism for the formation of ice edge bands, J. Geophys. Res. 88(C5): 2813–2818, 1983.

Wadhams P., V. Squire, J.A. Ewing and R.W. Pascal (1986). The effect of the Marginal Ice Zone on the directional wave spectrum of the Ocean. J. of Physical Oceanography, Vol. 16, pp. 358–376.